Modeling of the viscoelastic honeycomb panel equipped with piezoelectric patches in view of vibroacoustic active control design

Corine Florens

THÈSE

présentée par

Corine FLORENS

pour l'obtention du

GRADE DE DOCTEUR

Spécialité : **Mécanique**
Laboratoire d'accueil : **ECP/MSSMat - ONERA/DADS**

Modeling of the viscoelastic honeycomb panel equipped with piezoelectric patches in view of vibroacoustic active control design

soutenue le 22 janvier 2010 devant un jury composé de

Président :	M. Denis Aubry, professeur des universités (Ecole Centrale Paris, MSSMat)
Rapporteurs :	M. Arnaud Deraemaeker, chargé de recherche FNRS, HDR (Université Libre de Bruxelles, BATir) M. Laurent Gornet, maitre de conférences HDR (Ecole Centrale Nantes, GeM)
Examinateurs :	M. Benoit Petitjean, expert (EADS Innovation Works)
Directeur de thèse :	M. Etienne Balmes, PAST HDR (Arts et Metiers Paristech, PIMM)
Invités :	M. Franck Clero, ingénieur de recherche (ONERA, DSNA)

n° 2010 ECAP 0001

Remerciements

Je souhaite exprimer toute ma gratitude à tous ceux et toutes celles qui m'ont aidée et soutenue durant ces années passées à préparer ma thèse.

Je tiens tout d'abord à adresser mes plus vifs remerciements à M. Etienne Balmès pour avoir dirigé cette thèse. Sa disponibilité, son soutien sans faille, ses qualités humaines et scientifiques ont permis l'aboutissement de mes travaux de recherche. Ce fût un réel plaisir de travailler ensemble. Je remercie également M. Franck Cléro pour avoir co-encadré ma thèse au sein de l'ONERA, et pour nos nombreuses discussions concernant le contrôle actif.

J'exprime aussi toute ma reconnaissance envers les membres du jury qui m'ont fait l'honneur de participer à l'examen de ce travail: MM. Arnaud Deraemaeker et Laurent Gornet, pour le temps précieux qu'ils ont consacré à relire mon manuscrit et à faire un rapport précis de ce travail. Qu'ils trouvent ici toute ma gratitude. M. Denis Aubry, qui a accepté de présider le jury durant la soutenance. M. Benoît Petitjean, pour avoir accepté de participer en tant qu'examinateur à la soutenance de ma thèse, M. Franck Cléro, en tant que membre invité.

J'adresse un remerciement tout particulier aux personnes qui m'ont apporté leur savoir ou leur savoir-faire, et sans qui ce travail ne serait pas ce qu'il est. MM. Laurent Coste de l'ONERA Châtillon, Mathieu Corus du laboratoire MSSMat de l'Ecole Centrale Paris, Kent Lindgren et Danilo Prelevic du laboratoire MWL de l'université KTH de Stockholm pour les aspects techniques et expérimentaux.

Je remercie chaleureusement M. Denis Aubry pour m'avoir accueillie au sein du laboratoire MSSMat et de l'équipe enseignante Tronc Commun de Mécanique à l'École Centrale Paris. Merci à tous les membres du laboratoire MSSMat pour les différents échanges que nous avons pu avoir ainsi qu'à l'équipe enseignante Tronc Commun de Mécanique pour les moments passés avec eux, en particulier Jean-Sebastien Schotte et Eric Savin.

Je remercie également le professeur Anders Nilsson, du laboratoire MWL de l'université KTH de Stockholm qui a suivi mes travaux dans le cadre de l'échange universitaire *European Doctorate in Sound and Vibration Studies* subventionné par le programme Marie Curie. Merci à tous les étudiants européens avec qui j'ai partagé six mois inoubliables à Stockholm: Daniel, Maria-José, Francesca, Hans, Fabrice, Paolo...

Pour les bons moments que nous avons passés ensemble, merci à toute l'équipe onérienne anciennement DDSS CAV. Que soient remerciés ici à nouveau Franck Cléro et Laurent Coste, mais aussi Isabelle Legrain, Florence Roudolff, Frédéric Mortain et Dominique Le Bihan. Je remercie tout particulièrement Pierrick Jean, avec qui je partageais le bureau, et Arnaud Lepage pour avoir contribué à ce que ces années à l'ONERA aient été aussi agréables qu'enrichissantes.

Je remercie enfin, du fond du coeur, ma famille. Merci, à mes parents qui m'ont toujours soutenue tout en me laissant libre dans le choix de mon parcours personnel, à mon frère Olivier qui a toujours été un exemple pour moi. Merci à Julien qui n'a pas hésité à quitter notre Provence natale pour venir partager ces quelques années parisiennes avec moi, son soutien et son affection m'ont été précieux.

Contents

*Modeling of a viscoelastic honeycomb panel equipped with piezoelectric patches in view of
vibroacoustic active control design*

List of Figures

Modeling of a viscoelastic honeycomb panel equipped with piezoelectric patches in view of vibroacoustic active control design

*Modeling of a viscoelastic honeycomb panel equipped with piezoelectric patches in view of
vibroacoustic active control design*

List of Tables

Nomenclature

Scalars

a, b	length of honeycomb cell sides (x-direction and inclined)
θ	angle of cell
t, t'	thicknesses of simple, double honeycomb cell wall
h	layer thickness
E	Young modulus
G	shear modulus
ν	Poisson's ratio
ρ	density
$G_{xz}^{\star}(G_{1z}^{\star}), G_{yz}^{\star}(G_{2z}^{\star})$	effective transverse shear moduli of the equivalent core
E_f	face sheet Young modulus
u_1, u_2, w	displacements on the mid-plane of a laminate in the material principal basis $(\mathbf{x_1}, \mathbf{x_2}, \mathbf{x_3})$
u_x, u_y, w	displacements on the mid-plane of a laminate in any structural basis $(\mathbf{x}, \mathbf{y}, \mathbf{z})$
U_1, U_2, U_3	displacements of any point on the cross section in the material principal basis $(\mathbf{x_1}, \mathbf{x_2}, \mathbf{x_3})$
x_1, x_2, x_3	spatial coordinates in the material principal basis $(\mathbf{x_1}, \mathbf{x_2}, \mathbf{x_3})$
x, y, z	spatial coordinates in any structural basis $(\mathbf{x}, \mathbf{y}, \mathbf{z})$
β_1, β_2	slopes around $\mathbf{x_2}$ and $\mathbf{x_1}$ respectively
γ_1, γ_2	transverse shear strains at the mid-plane of the plate
θ_1, θ_2	rotations around $\mathbf{x_1}$ and $\mathbf{x_2}$ respectively
$\varepsilon_{ij}, \gamma_{ij}$	normal and shear strains
σ_{ij}, τ_{ij}	normal and shear stresses
c_{ij}, q_{ij}	3D and reduced stiffness coefficients
ϕ_k	electric DOF
Q_k	total charge on an electrode
f	frequency
ζ	damping ratio

Operators

$\frac{\partial f}{\partial x}$	spatial derivative of f with respect to x
$f_{,x}$	short notation for the spatial derivative of f with respect to x

Modeling of a viscoelastic honeycomb panel equipped with piezoelectric patches in view of vibroacoustic active control design

Vectors

$\{\cdot\}$	any vector
$\{\cdot\}^T$	any vector transposed
$\{\mathbf{u}\}$	displacement field vector on the mid-plane of a laminate
$\{\mathbf{U}\}$	displacement field vector of any point of a laminate
$\{\boldsymbol{\varepsilon}\}, \{\mathbf{S}\}$	strain vector, elasticty and IEEE Standard notations
$\{\boldsymbol{\varepsilon}^{\mathbf{m}}\}, \{\boldsymbol{\kappa}\}, \{\boldsymbol{\gamma}\}$	membrane, curvature or bending, shear strains
$\{\boldsymbol{\sigma}\}, \{\mathbf{T}\}$	stress vector, elasticty and IEEE Standard notations
$\{\mathbf{N}\}, \{\mathbf{M}\}, \{\mathbf{Q}\}$	membrane forces, bending moments and shear forces
$\{\boldsymbol{\phi}\}$	normal modeshapes
$\{\mathbf{D}\}$	electric displacement
$\{\mathbf{E}\}$	electric field

Matrices

$[\cdot]$	any matrix
$[\cdot]^T$	any matrix transposed
$[\mathbf{A}], [\mathbf{B}], [\mathbf{D}]$	extensional stiffness, extension/bending coupling, bending stiffness matrices
$[\mathbf{F}], [\mathbf{H}]$	shear and corrected shear matrices
$[\mathbf{R}_\sigma]$	rotation matrix relating the stress in any structural basis and in the material principal basis
$[\mathbf{R}_\varepsilon]$	rotation matrix relating the strain in any structural basis and in the material principal basis
$[\boldsymbol{\Lambda}]$	constitutive law
$[\mathcal{N}]$	shape functions
$[\mathcal{B}]$	shape functions derivatives
$[\mathbf{K}]$	stiffness matrix
$[\mathbf{M}]$	mass matrix
$[\mathbf{s}^{\mathbf{E}}]$	compliance under constant electric field matrix
$[\mathbf{d}]$	piezoelectric constants matrix
$[\boldsymbol{\varepsilon}^{\mathbf{T}}]$	dielectric constants under constant stress matrix
$[\mathbf{c}^{\mathbf{E}}]$	stiffness under constant electric field matrix
$[\boldsymbol{\varepsilon}^{\mathbf{S}}]$	permittivity under constant strain matrix

Subscripts

$\cdot_f$	quantity relative to the sandwich face sheets
$\cdot_g$	quantity relative to the glue
$\cdot_h$	quantity relative to the pure honeycomb core
$\cdot_k$	quantity relative to a layer k

Modeling of a viscoelastic honeycomb panel equipped with piezoelectric patches in view of vibroacoustic active control design

Superscripts

$\cdot^{\star}$ effective properties of equivalent core

$\cdot^{k}$ quantity relative to a layer k

Acronyms

AN20	20 milimeter-thick Aluminum/Nomex honeycomb specimen
ASAC	Active Structural Acoustic Control
CLPT	Classical Laminate Plate Theory
CN20	20 milimeter-thick Carbon/Nomex honeycomb specimen
DOF	Degree(s) Of Freedom
FE	Finite Element
FEM	Finite Element Model
FOST	First-Order Shear Theory
FRF	Frequency Response Function
HEXA8	8-node 24-DOF brick
HOST	Higher Order Shear Theories
L	longitudinal direction (Length)
MAC	Modal Assurance Criterion
MITC4	4-node 20-DOF shell
QP20W	Midé QuickPack patch with two piezoelectric electrodes
RVE	Representative Volume Element
SVS	Shell-Volume-Shell
W	transverse direction (Width)
2D	Two-Dimensional
3D	Three-Dimensional

Chapter 1

Introduction

Reducing noise transmission inside cabins is an important concern for the aircraft industry, mainly to improve the comfort of passengers and reduce stress on the crew. Noise in the cabin has different sources [6] classified in

- exterior sources, whose field is transmitted through the fuselage skin, thermal insulation and trim panel multi-layered structure,

- interior sources, which are mainly related to air conditioning,

- structure borne sound, transmitted through structural parts before being radiated by the different panels inside the cabin.

Most of the exterior noise is filtered by the fuselage skin and interior furnishing, it nevertheless crosses different structural parts in its propagation and produces noise inside the cabin. In this propagation, trim panels represent the last barrier before cabin cavity. They cover the entire walls of the cabin, with the exception of its floor, and the overhead compartments. They significantly participate in the global acoustical behavior of the cabin. Figure 1.1 (left) represents a roof trim panel of a cabin representative of generic NH90 helicopter, this mock-up (named VASCo) has been developed at ONERA DMAE department in Toulouse. The middle figure shows how the trim panel is positioned in the VASCo helicopter cabin and the right figure shows how the panel is equipped for active control test.

Figure 1.1: *Trim panel (left), VASCo cabin with trim panel (middle) and test set up for vibroacoustic control (right)*

Modeling of a viscoelastic honeycomb panel equipped with piezoelectric patches in view of vibroacoustic active control design

Two main techniques exist aimed at reducing the sound radiated by the vibrating trim panels inside the cabin. Passive techniques optimize the panel geometric and material characteristics to minimize the transmission of vibration. Active techniques block, or at least limit, vibrations by generating suitable lots or antagonist vibrations.

Passive techniques use vibration isolation, to limit the transmission to the panel of vibrations coming from the main body frame through attachment points, and damping enhancement, were absorbing materials, typically viscoelastic, are added in the panel setup. When properly designed, passive treatments are efficient and have the advantage of not requiring external energy. Efficiency does however typically come with a significant mass increase and an efficiency that grows with frequency.

Figure 1.2 represents the transmission loss of the VASCo trim panel where the poor passive performance at low frequencies is clearly visible. The motivation for active vibration solutions is thus focused on improving performance in the low to medium frequency range.
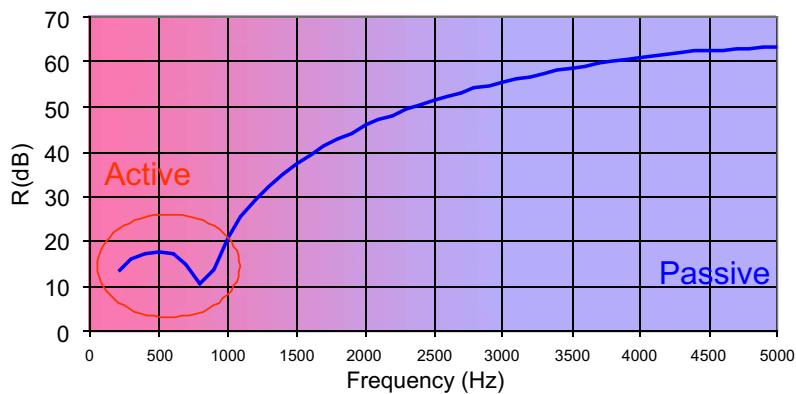
Figure 1.2: *Transmission Loss of the optimed trim panel (VASCo)*

Usually trim panels are made of sandwich composite. Sandwich plates are multilayered structures constituted by high-strength and stiff layers, named face sheets or skins, bonded to one or more low-density and soft layers, named core. Sandwich panels combine light weight and high stiffness. Therefore, since the World War II, the number of their applications has steadily increased. Nowadays, sandwich structures are widely used not only in aerospace industry but also in shipbuilding, construction and sports. Various material combinations can be used [7]. The face sheets are usually made of metal or fibrous composites (aluminum, carbon or glass reinforced plastic composite laminate). For the core, one distinguishes solid low-density material, such as viscoelastic material film or solid foam, and expanded high density material in cellular form, such as honeycomb core. For aerospace applications, both metallic and non-metallic (nomex, fiberglass, kraft paper [5]) honeycombs are used. Bonding between the honeycomb and the face sheets is typically achieved with an adhesive as represented on Figure 1.3.
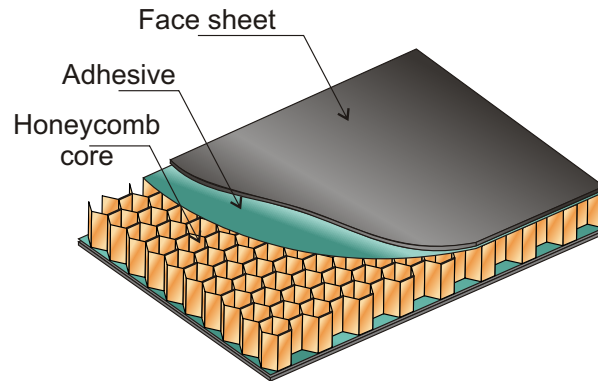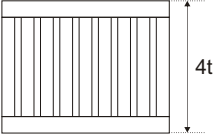
Figure 1.3: *Honeycomb core sandwich composite*

Honeycomb core sandwich structures behave like I-beams. Face sheets carry most of the bending and in-plane loads, whereas the core contributes to the bending stiffness, out-of-plane shear and compressive strength. Their mechanical efficiency is much better than a solid plate or beam with equivalent weight, as shown in Table 1.1.

Table 1.1: *Honeycomb sandwich efficiency [5]*

	Solid Material	Core Thickness h	Core Thickness 3.h
Relative Stiffness	1	7	37
Flexural Strength	1	3.5	9.2
Relative Weight	1	1.03	1.06

A honeycomb sandwich trim panel has a high strength to mass ratio, but its acoustic and dynamic properties need to be improved [8], through passive viscoelastic treatments in the high frequencies and active control in the low frequency. The first objective of the proposed work is thus to propose numerical models that could then be used to optimize passive and active panel characteristics. The second objective is to validate these models through experiments.

In fact, the damping behavior of viscoelastic based honeycomb core trim panels, possibly optimized with viscoelastic layers, contributes passively to alleviate high frequency noise and vibration. Thus, the biggest difficulty is to remove low and medium frequency noise, which is the object of the present work.

To properly design an active control system for trim panels, simulations are necessary for actuator placement and sizing and general performance evaluations. In the case of honeycomb cores, a detailed model of the cell geometry is rapidly inaccessible. A detailed, yet still simplified, representation of the cell using 3D plate elements for all walls will be considered in chapter 3. For this cell representation, a sample test beam $900 \times 45 \times 21$mm leads to a model with about 100000 DOFs. This is acceptable for sample validations, but is clearly not acceptable for full panel predictions. For the considered honeycomb, a 2 meters long and 1 meter wide helicopter trim panel would require 4.10^6 DOFs.

The first difficulty addressed in this work is thus to build an effective model representing the honeycomb core that allows element sizes not directly related to honeycomb cell sizes. Chapter 2 thus recalls fundamentals of classical laminate theory and provides a literature review of models used to represent honeycomb based sandwich panels. Classically, honeycomb panels are represented using an orthotropic volume for the honeycomb and shell elements for skins. Methodologies to integrate this model into finite elements (single layer, zig-zag and multi-element representations) and to estimate effective material parameters for the orthotropic core are detailed showing the variety of existing approaches and the lack of general agreement on exact details.

The first contribution of the thesis is the introduction, in chapter 3, of a numerical homogeneization procedure to estimate effective core parameters. The principle of this methodology is to correlate the frequencies of periodic modes in a detailed 3D and an effective model to estimate material properties of the effective model that minimize mismatch. The novel application of this approach to honeycomb panels gives a very general approach that can be used to build equivalent models using extremely detailed cell models. The analysis of the equivalence for a wide range of wavelength/frequencies gives useful insight on the validity of models.

Illustrations are given for a specific range of honeycombs with a detailed 3D plate model and a shell, orthotropic volume, shell model (SVS) effective model. The SVS model is preferred here because it can easily be implemented in most FEM software and leads to significant model size reduction (a factor 10 in this particular case). The results obtained are close to those of earlier methods, so the real interest is in the new ability to assess the simplified model and to address issues such as the effect of glue or local bending of cell wall.

Numerical homogeneization relies on the knowledge of detailed cell geometries and material properties. Since these are typically not known with very high accuracy, tests on sandwich samples are necessary. Helicopter or aircraft trim panels are commonly made with non-metallic honeycomb core sandwich, which have the advantage of a lower density. In particular, Nomex paper based honeycomb are the focus of the present work. Nomex paper, basis of honeycomb Nomex core, is a non woven sheet made of short

aramid fibers (Nomex). It is calendered before being impregnated with phenolic resin which is typically viscoelastic. The glue used to bond the Nomex honeycomb to the skins is probably also viscoelastic.

Chapter 4 details the use of modal tests on sample sandwich beams to estimate the material parameters of a viscoelastic core. Viscoelastic materials have a significant frequency and temperature dependence that is correctly identified by the tests. Tests on beams with aluminum and carbon skins are shown and demonstrate the ability to have very predictive models.

The final contribution of the thesis is, in chapter 5, the introduction, validation and use of a FEM model of honeycomb panels equipped with piezoelectric actuators. Such models are needed for active control predictions in order to avoid costly trial and error phases on actuator placement and sizing.

The formulation of a piezoelectric shell element, based on the work of Piefort [9], is first introduced. Its integration in a numerical simulation process is then discussed for actuator and sensor configurations. To validate the model a series of modal tests are presented and test/analysis correlation demonstrates very good model validity.

The considered honeycomb sandwiches are shown to exhibit a strong skin bending, which corresponds to the static deformation associated with the patches. This static contribution is particularly important for honeycomb panels and fundamentally limits the achievable performance. The experimental presence of localized sound sources was a significant factor motivating the need for this work. The conclusion on the importance of static correction effects clearly explains the origin of these effects and opens perspectives on the ability to redesign actuators to obtain better performance. The chapter concludes by discussing applications of the proposed model in further design work, thus preparing ground for a full control design [10].

Chapter 2

Honeycomb core sandwich composite survey

Contents

2.1   Introduction

The first step towards the objective proposing predictive models of active honeycomb panels is to model panels. This chapter thus provides a partial review of the literature existing on the topic.

Section 2.2 presents the Classical Laminated Plate Theory, which will be used to model panel skins and will also serve as reference for piezoelectric patch model introduced in Section 5.2.

Section 2.3.1 then classifies approaches to model the dynamic properties of sandwich structures in four main strategies. The classification is done in terms of increasing complexity, from the global approximation model in which one equivalent single layer in modeled, to the detailed 3D finite element model.

Within these approaches, it is classical to consider the honeycomb as an orthotropic material. Since 1958 [11], many methods for honeycomb elastic material properties estimation were introduced [12] and none of the approaches seems to have the total agreement. Section 2.3 provides a literature review on this subject and a numerical homogeneization procedure will be introduced in the next chapter.

2.2   Laminated plate theory

Three-dimensional finite element models developed in this work use laminated plate elements to model honeycomb cell wall, multi-ply composite for face sheets or for piezoelectric patches bonded on the faces. The different kinematic assumptions for plates are first presented in Section 2.2.1. Section 2.2.2 then summarizes the plate formulation for isotropic and orthotropic elastic materials. Section 2.2.3 finally addresses multi-layer laminates.

In this section the compact notation $f_{,x}$ is used for the partial derivative of the function f with respect to the variable x, $\frac{\partial f}{\partial x}$. As x_1, x_2 and x_3 are used for coordinates in space, $\frac{\partial f}{\partial x_1}$ becomes $f_{,1}$, similarly $f_{,2} = \frac{\partial f}{\partial x_2}$ and $f_{,3} = \frac{\partial f}{\partial x_3}$.

2.2.1   Plate kinematics

The choice of the increasingly elaborate kinematic assumptions can be used to classify the many existing plate theories.

Figure 2.1 represents Kirchhoff-Love's, Reissner-Mindlin's and Reddy's kinematic assumptions for the cross section. These assumptions are directly linked to the shear deformation modeling.
Classical laminate plate theory (CLPT) based on Kirchhoff-Love kinematic assumptions [13] doesn't take shearing across the thickness into account, whereas first-order shear theory (FOST) with Reissner-Mindlin assumptions [14] and higher order shear theories (HOST)

developed by Reddy [15], and next by Touratier [16] represent with more or less precision the shear phenomenon.

The first and simplest Kirchhoff-Love theory is accurate enough for thin plates. A cross section normal to the mid-plane remains straight and orthogonal to the mid-plane after bending. For thick and soft plates, the shear cannot be neglected, it is taken into account by enriching the displacement formulation across the thickness. Many improvements exist from linear approximation to higher order theories.
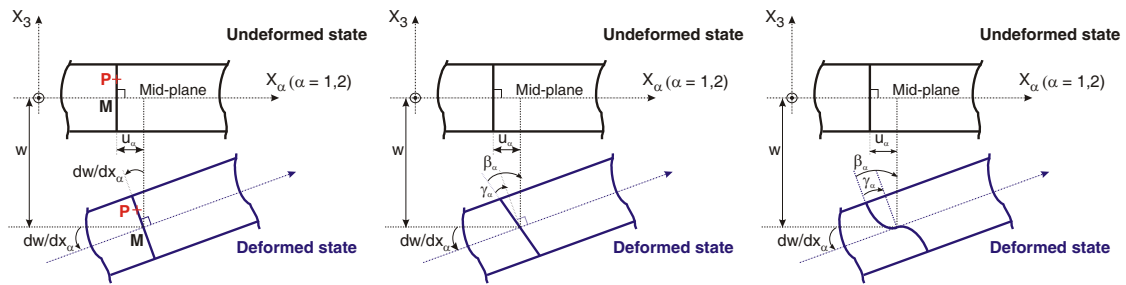
Figure 2.1: *Kirchhoff-Love's, Reissner-Mindlin's, and Reddy's theories*

The general expression of kinematics has been expressed by Touratier et al. [17]

$$\{\mathbf{U}\} = \left\{ \begin{array}{l} U_1 = u_1(x_1, x_2) - x_3.w_{,1}(x_1, x_2) + f(x_3).\gamma_1(x_1, x_2) \\ U_2 = u_2(x_1, x_2) - x_3.w_{,2}(x_1, x_2) + f(x_3).\gamma_2(x_1, x_2) \\ U_3 = w(x_1, x_2) \end{array} \right\}, \quad (2.1)$$

where, as specified on Figure 2.1,

- $\mathbf{x_3}$ is normal to the plate,

- u_1, u_2, w are the displacements of a point M on the mid-plane, along axes $\mathbf{x_1}$, $\mathbf{x_2}$, $\mathbf{x_3}$,

- U_1, U_2, U_3 the displacements of a point P on the M-cross section, along $\mathbf{x_1}$, $\mathbf{x_2}$, $\mathbf{x_3}$,

- γ_1, γ_2 are the transverse shear strains at the mid-plane of the plate,

$$\gamma_\alpha = \beta_\alpha + w_{,\alpha} \quad (\alpha = 1, 2) \quad (2.2)$$

- β_1, β_2 are the slopes around $\mathbf{x_2}$ and $\mathbf{x_1}$ respectively,

- and f can be seen as a *shear function* and takes the forms given in Table 2.1,

Modeling of a viscoelastic honeycomb panel equipped with piezoelectric patches in view of vibroacoustic active control design

Table 2.1: *Shear function f*

Kirchhoff-Love [13]	$f(x_3) = 0$
Reissner-Mindlin [14]	$f(x_3) = x_3$
Reddy [15]	$f(x_3) = x_3(1 - \frac{4x_3^2}{3h^2})$
Touratier [16]	$f(x_3) = \frac{h}{\pi} sin\frac{\pi x_3}{h}$

First-order shear deformation theory with Reissner-Mindlin's assumptions is widely implemented for thick plates. The transverse shear strains or stresses are assumed to be constant within the thickness, therefore to account for the non-uniformity of the through-thickness shear distribution, correction factors are introduced in the transverse shear constitutive relations (2.26).

Two notations can be found in literature for the rotation of the cross section after deformation. It is important to clarify this point. One suggests to do this in the context of Reissner-Mindlin's assumptions. The displacement field at a point P on the M-cross section depends on the displacement field at the point M on the mid-plane and on the rotation of the segment MP

$$\mathbf{U}(P) = \mathbf{u}(M) + \mathbf{\Omega} \wedge \mathbf{MP} \tag{2.3}$$

Classically, the rotation vector $\mathbf{\Omega}$ is written $\mathbf{\Omega} = \theta_1\mathbf{x_1} + \theta_2\mathbf{x_2}$. One introduces a field $\mathbf{\Psi}$ related to the rotation, classically written $\mathbf{\Psi} = \beta_1\mathbf{x_1} + \beta_2\mathbf{x_2}$ such that

$$\mathbf{\Omega} = \mathbf{x_3} \wedge \mathbf{\Psi} \tag{2.4}$$

so that the displacement field at the point P becomes

$$\mathbf{U}(P) = \mathbf{u}(M) + \mathbf{\Omega} \wedge \mathbf{MP} = \mathbf{u}(M) + x_3\mathbf{\Psi} \tag{2.5}$$

and the relations between the rotation θ_i and the slope β_i are

$$\begin{aligned} \beta_1 &= \theta_2 \\ \beta_2 &= -\theta_1 \end{aligned} \tag{2.6}$$

2.2.2   2D elastic material law

Both isotropic and orthotropic materials are considered in this work. In these cases, the general form of the 3D elastic material law is

$$
\begin{Bmatrix} \sigma_{11} \\ \sigma_{22} \\ \sigma_{33} \\ \tau_{23} \\ \tau_{13} \\ \tau_{12} \end{Bmatrix} = \begin{bmatrix} c_{11} & c_{12} & c_{13} & 0 & 0 & 0 \\ & c_{22} & c_{23} & 0 & 0 & 0 \\ & & c_{33} & 0 & 0 & 0 \\ & & & c_{44} & 0 & 0 \\ & (s) & & & c_{55} & 0 \\ & & & & & c_{66} \end{bmatrix} \begin{Bmatrix} \varepsilon_{11} \\ \varepsilon_{22} \\ \varepsilon_{33} \\ \gamma_{23} \\ \gamma_{13} \\ \gamma_{12} \end{Bmatrix}.
\tag{2.7}
$$

For orthotropic material, the law depends on 3 Poisson ratios, 3 Young moduli and 3 shear moduli and is given by (3.14) and for isotropic linear elastic material the law is written as follow,

$$
\begin{Bmatrix} \sigma_{11} \\ \sigma_{22} \\ \sigma_{33} \\ \tau_{23} \\ \tau_{13} \\ \tau_{12} \end{Bmatrix} = \frac{E(1-\nu)}{(1+\nu)(1-2\nu)} \begin{bmatrix} 1 & \frac{\nu}{1-\nu} & \frac{\nu}{1-\nu} & 0 & 0 & 0 \\ \frac{\nu}{1-\nu} & 1 & \frac{\nu}{1-\nu} & 0 & 0 & 0 \\ \frac{\nu}{1-\nu} & \frac{\nu}{1-\nu} & 1 & 0 & 0 & 0 \\ 0 & 0 & 0 & \frac{1-2\nu}{2(1-\nu)} & 0 & 0 \\ 0 & 0 & 0 & 0 & \frac{1-2\nu}{2(1-\nu)} & 0 \\ 0 & 0 & 0 & 0 & 0 & \frac{1-2\nu}{2(1-\nu)} \end{bmatrix} \begin{Bmatrix} \varepsilon_{11} \\ \varepsilon_{22} \\ \varepsilon_{33} \\ \gamma_{23} \\ \gamma_{13} \\ \gamma_{12} \end{Bmatrix}
\tag{2.8}
$$

Plate formulation consists in assuming one dimension, the thickness along x_3, negligible compared with the surface dimensions. Thus, vertical stress $\sigma_{33} = 0$ on the bottom and upper faces, and assumed to be neglected throughout the thickness,

$$
\sigma_{33} = 0 \Rightarrow \varepsilon_{33} = -\frac{1}{c_{33}} \left(c_{13}\varepsilon_{11} + c_{23}\varepsilon_{22} \right),
\tag{2.9}
$$

and for isotropic material,

$$
\sigma_{33} = 0 \Rightarrow \varepsilon_{33} = -\frac{\nu}{1-\nu} \left(\varepsilon_{11} + \varepsilon_{22} \right).
\tag{2.10}
$$

By eliminating σ_{33}, the plate constitutive law simplifies, with engineering notations,

$$
\begin{Bmatrix} \sigma_{11} \\ \sigma_{22} \\ \tau_{12} \\ \tau_{23} \\ \tau_{13} \end{Bmatrix} = \begin{bmatrix} q_{11} & q_{12} & 0 & 0 & 0 \\ q_{12} & q_{22} & 0 & 0 & 0 \\ 0 & 0 & q_{66} & 0 & 0 \\ 0 & 0 & 0 & q_{44} & 0 \\ 0 & 0 & 0 & 0 & q_{55} \end{bmatrix} \begin{Bmatrix} \varepsilon_{11} \\ \varepsilon_{22} \\ \gamma_{12} \\ \gamma_{23} \\ \gamma_{13} \end{Bmatrix}.
\tag{2.11}
$$

The reduced stiffness coefficients q_{ij} ($i,j = 1,2,4,5,6$) are related to the 3D stiffness coefficients c_{ij} by

$$
q_{ij} = \begin{cases} c_{ij} - \dfrac{c_{i3}c_{j3}}{c_{33}} & \text{if } i,j = 1,2, \\ c_{ij} & \text{if } i,j = 4,5,6. \end{cases}
\tag{2.12}
$$

Hence, the reduced elastic law for an isotropic plate becomes,

$$
\left\{ \begin{array}{c} \sigma_{11} \\ \sigma_{22} \\ \tau_{12} \end{array} \right\} = \frac{E}{(1-\nu^2)} \begin{bmatrix} 1 & \nu & 0 \\ \nu & 1 & 0 \\ 0 & 0 & \frac{1-\nu}{2} \end{bmatrix} \left\{ \begin{array}{c} \varepsilon_{11} \\ \varepsilon_{22} \\ \gamma_{12} \end{array} \right\},
\tag{2.13}
$$

and

$$
\left\{ \begin{array}{c} \tau_{23} \\ \tau_{13} \end{array} \right\} = \frac{E}{2(1+\nu)} \begin{bmatrix} 1 & 0 \\ 0 & 1 \end{bmatrix} \left\{ \begin{array}{c} \gamma_{23} \\ \gamma_{13} \end{array} \right\}.
\tag{2.14}
$$

Under Reissner-Mindlin's kinematic assumptions, given by (2.1) and (2.2) with shear function $f(x_3) = x_3$, the linearized strain tensor is

$$
[\boldsymbol{\varepsilon}] = \begin{bmatrix} u_{1,1} + x_3\beta_{1,1} & \frac{1}{2}(u_{1,2} + u_{2,1} + x_3(\beta_{1,2} + \beta_{2,1})) & \frac{1}{2}(\beta_1 + w_{,1}) \\ & u_{2,2} + x_3\beta_{2,2} & \frac{1}{2}(\beta_2 + w_{,2}) \\ (s) & & 0 \end{bmatrix}.
\tag{2.15}
$$

So, the strain vector is written,

$$
\{\boldsymbol{\varepsilon}\} = \left\{ \begin{array}{c} \varepsilon_{11}^m + x_3\kappa_{11} \\ \varepsilon_{22}^m + x_3\kappa_{22} \\ \gamma_{12}^m + x_3\kappa_{12} \\ \gamma_{23} \\ \gamma_{13} \end{array} \right\},
\tag{2.16}
$$

with $\{\boldsymbol{\varepsilon^m}\}$ the membrane, $\{\boldsymbol{\kappa}\}$ the curvature or bending, and $\{\boldsymbol{\gamma}\}$ the shear strains,

$$
\{\boldsymbol{\varepsilon^m}\} = \left\{ \begin{array}{c} u_{1,1} \\ u_{2,2} \\ u_{1,2} + u_{2,1} \end{array} \right\}, \quad \{\boldsymbol{\kappa}\} = \left\{ \begin{array}{c} \beta_{1,1} \\ \beta_{2,2} \\ \beta_{1,2} + \beta_{2,1} \end{array} \right\}, \quad \{\boldsymbol{\gamma}\} = \left\{ \begin{array}{c} \beta_2 + w_{,2} \\ \beta_1 + w_{,1} \end{array} \right\}.
\tag{2.17}
$$

Note that the engineering notation with $\gamma_{12} = u_{1,2} + u_{2,1}$ is used here, rather than the tensor notation with $\varepsilon_{12} = (u_{1,2} + u_{2,1})/2$. Similarly $\kappa_{12} = \beta_{1,2} + \beta_{2,1}$, whereas a factor $1/2$ would be needed for the tensor.

The stress resultants are obtained by integrating the stresses through the thickness of the plate,

$$
N_{\alpha\beta} = \int_{x_3(0)-h/2}^{x_3(0)+h/2} \sigma_{\alpha\beta}\, dx_3,
\tag{2.18}
$$

$$
M_{\alpha\beta} = \int_{x_3(0)-h/2}^{x_3(0)+h/2} x_3\, \sigma_{\alpha\beta}\, dx_3,
\tag{2.19}
$$

$$Q_{\alpha 3} = \int_{x_3(0)-h/2}^{x_3(0)+h/2} \tau_{\alpha 3}\, dx_3, \tag{2.20}$$

with $\alpha, \beta = 1, 2$, and $x_3(0)$ the position of the mid-plane from the reference-plane (or mesh-plane).
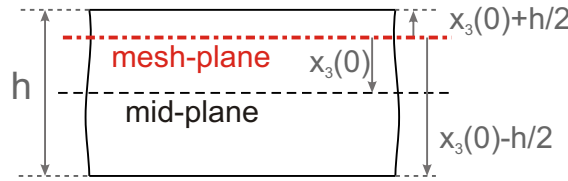
Figure 2.2: *Geometry of an unsymmetric plate*

The plate formulation links the stress resultants, membrane forces $\{\mathbf{N}\}$, bending moments $\{\mathbf{M}\}$ and shear forces $\{\mathbf{Q}\}$, to membrane $\{\boldsymbol{\varepsilon}^{\mathbf{m}}\}$, bending $\{\boldsymbol{\kappa}\}$ and shearing $\{\boldsymbol{\gamma}\}$ strains,

$$\left\{ \begin{array}{c} \mathbf{N} \\ \mathbf{M} \\ \mathbf{Q} \end{array} \right\} = \left[\begin{array}{ccc} \mathbf{A} & \mathbf{B} & \mathbf{0} \\ \mathbf{B} & \mathbf{D} & \mathbf{0} \\ \mathbf{0} & \mathbf{0} & \mathbf{F} \end{array} \right] \left\{ \begin{array}{c} \boldsymbol{\varepsilon}^{\mathbf{m}} \\ \boldsymbol{\kappa} \\ \boldsymbol{\gamma} \end{array} \right\}. \tag{2.21}$$

Therefore, the non-zero terms of the extensional stiffness matrix $[\mathbf{A}]$, extension/bending coupling matrix $[\mathbf{B}]$, and the bending stiffness matrix $[\mathbf{D}]$ are calculated as

$$A_{ij} = \int_{x_3(0)-h/2}^{x_3(0)+h/2} q_{ij}\, dx_3 \quad \text{if } i, j = 1, 2, \quad A_{33} = \int_{x_3(0)-h/2}^{x_3(0)+h/2} q_{66}\, dx_3, \tag{2.22}$$

$$B_{ij} = \int_{x_3(0)-h/2}^{x_3(0)+h/2} x_3\, q_{ij}\, dx_3 \quad \text{if } i, j = 1, 2, \quad B_{33} = \int_{x_3(0)-h/2}^{x_3(0)+h/2} x_3\, q_{66}\, dx_3, \tag{2.23}$$

$$D_{ij} = \int_{x_3(0)-h/2}^{x_3(0)+h/2} x_3^2\, q_{ij}\, dx_3 \quad \text{if } i, j = 1, 2, \quad D_{33} = \int_{x_3(0)-h/2}^{x_3(0)+h/2} x_3^2\, q_{66}\, dx_3, \tag{2.24}$$

$$F_{11} = \int_{x_3(0)-h/2}^{x_3(0)+h/2} q_{44}\, dx_3, \quad F_{22} = \int_{x_3(0)-h/2}^{x_3(0)+h/2} q_{55}\, dx_3. \tag{2.25}$$

An improvement of Mindlin's plate theory with tranverse shear consists in modifying the shear coefficients F_{ij} by

$$H_{ij} = k_{ij}F_{ij},\qquad(2.26)$$

where k_{ij} are correction factors. Reddy's 3rd order theory, see Table 2.1, brings to $k_{ij} = \frac{2}{3}$. Very commonly, enriched 3rd order theory is used, and k_{ij} are equal to $\frac{5}{6}$ and give good results. For more details on the assessment of the correction factor, see ref. [18].

For an isotropic symmetric plate $(x_3(0) = 0)$, the in-plane normal forces N_{11}, N_{22} and shear force N_{12}, function of the kinematics parameters, become

$$\left\{ \begin{array}{c} N_{11} \\ N_{22} \\ N_{12} \end{array} \right\} = \frac{Eh}{1-\nu^2} \left[\begin{array}{ccc} 1 & \nu & 0 \\ & 1 & 0 \\ (s) & & \frac{1-\nu}{2} \end{array} \right] \left\{ \begin{array}{c} u_{1,1} \\ u_{2,2} \\ u_{1,2}+u_{2,1} \end{array} \right\},\qquad(2.27)$$

the 2 bending moments M_{11}, M_{22} and twisting moment M_{12},

$$\left\{ \begin{array}{c} M_{11} \\ M_{22} \\ M_{12} \end{array} \right\} = \frac{Eh^3}{12(1-\nu^2)} \left[\begin{array}{ccc} 1 & \nu & 0 \\ & 1 & 0 \\ (s) & & \frac{1-\nu}{2} \end{array} \right] \left\{ \begin{array}{c} \beta_{1,1} \\ \beta_{2,2} \\ \beta_{1,2}+\beta_{2,1} \end{array} \right\},\qquad(2.28)$$

and the out-of-plane shearing forces Q_{23} and Q_{13},

$$\left\{ \begin{array}{c} Q_{23} \\ Q_{13} \end{array} \right\} = \frac{Eh}{2(1+\nu)} \left[\begin{array}{cc} 1 & 0 \\ 0 & 1 \end{array} \right] \left\{ \begin{array}{c} \beta_2+w_{,2} \\ \beta_1+w_{,1} \end{array} \right\}.\qquad(2.29)$$

Formulations (2.27) to (2.29) are needed for the parametric study on reduced models (Section 3.2.3).

One can notice that for a symmetric plate, the reference plane is the mid-plane of the plate $(x_3(0) = 0)$ and the extension/bending coupling matrix $[\mathbf{B}]$ is a zero matrix.

Using expressions (2.22) to (2.25) for constant q_{ij}, one has for a non-zero offset $(x_3(0) \neq 0)$

$$A_{ij} = h.q_{ij} \quad B_{ij} = x_3(0).h.q_{ij} \quad D_{ij} = (x_3(0)^2.h + \frac{h^3}{12}).q_{ij} \quad F_{ij} = h.q_{ij}\qquad(2.30)$$

with subscripts i, j in accordance with (2.22) to (2.25). The constitutive matrix clearly appears as a polynomial function of h, h^3, $x_3(0)^2h$ and $x_3(0)h$. If the ply thickness is kept constant, the constitutive law is a polynomial function of $1, x_3(0), x_3(0)^2$.

2.2.3   Global multi-layered laminate theory

In the composite field, multi-ply laminates are widespread. The principle of the global multi-layered laminate theory is to replace the sandwich structure by a single equivalent layer. The limits of this approximation are discussed in Section 2.3.1. To provide a good stiffness in all laminate directions, unidirectional fiber reinforced composite layers are stacked with specific orientation, such as $0°/45°/90°$.
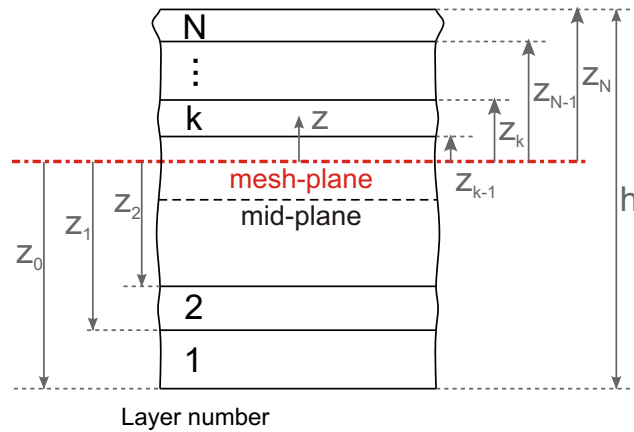
Figure 2.3: *Geometry of an N-layered laminate*

The constitutive matrix for an angled lamina can be expressed in terms of the constitutive matrix $[\mathbf{q}]_k$, in the principal directions $(\mathbf{x_1}, \mathbf{x_2}, \mathbf{x_3})$ of the layer k, with a rotation

$$\left[\mathbf{q'}\right]_k = \left[\mathbf{R_\sigma^k}\right]^{-1} [\mathbf{q}]_k \left[\mathbf{R_\varepsilon^k}\right].$$

(2.31)

In (2.31), $\left[\mathbf{R_\sigma^k}\right]$ and $\left[\mathbf{R_\varepsilon^k}\right]$ are the rotation matrices relating the stress $\{\mathbf{\sigma'}\}_k$ and strain $\{\mathbf{\varepsilon'}\}_k$ in any structural basis $(\mathbf{x}, \mathbf{y}, \mathbf{z})$ to $\{\mathbf{\sigma}\}_k$ and $\{\mathbf{\varepsilon}\}_k$ in the material principal basis $(\mathbf{x_1}, \mathbf{x_2}, \mathbf{x_3})$. The normal axis $\mathbf{z} = \mathbf{x_3}$ and the angle θ_k from $\mathbf{x}$ to $\mathbf{x_1}$, are shown on Figure 2.4.
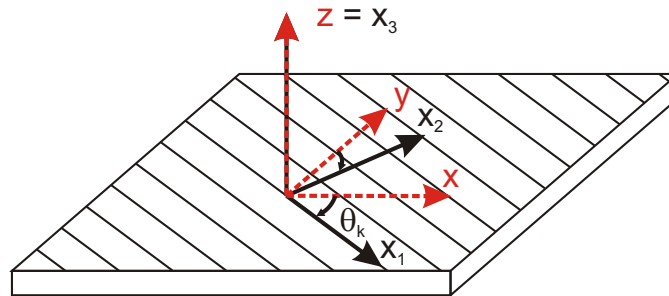
Figure 2.4: *Material and structural basis*

Modeling of a viscoelastic honeycomb panel equipped with piezoelectric patches in view of vibroacoustic active control design

For each constitutive layer of the laminate, the rotation matrices take the following forms,

$$
\left[\mathbf{R}_\sigma^k\right] = \begin{bmatrix}
\cos^2\theta_k & \sin^2\theta_k & 2\sin\theta_k\cos\theta_k & 0 & 0 \\
\sin^2\theta_k & \cos^2\theta_k & -2\sin\theta_k\cos\theta_k & 0 & 0 \\
-\sin\theta_k\cos\theta_k & \sin\theta_k\cos\theta_k & \cos^2\theta_k - \sin^2\theta_k & 0 & 0 \\
0 & 0 & 0 & \cos\theta_k & -\sin\theta_k \\
0 & 0 & 0 & \sin\theta_k & \cos\theta_k
\end{bmatrix}, \quad (2.32)
$$

and,

$$
\left[\mathbf{R}_\varepsilon^k\right] = \begin{bmatrix}
\cos^2\theta_k & \sin^2\theta_k & \sin\theta_k\cos\theta_k & 0 & 0 \\
\sin^2\theta_k & \cos^2\theta_k & -\sin\theta_k\cos\theta_k & 0 & 0 \\
-2\sin\theta_k\cos\theta_k & 2\sin\theta_k\cos\theta_k & \cos^2\theta_k - \sin^2\theta_k & 0 & 0 \\
0 & 0 & 0 & \cos\theta_k & -\sin\theta_k \\
0 & 0 & 0 & \sin\theta_k & \cos\theta_k
\end{bmatrix}, \quad (2.33)
$$

and in a compact form,

$$
\left[\mathbf{R}_\sigma^k\right] = \left[\begin{array}{c|c}
\left[\mathbf{R}_\sigma^k\right]_{(1,2,6)} & \mathbf{0} \\
\hline
\mathbf{0} & \left[\mathbf{R}_\sigma^k\right]_{(4,5)}
\end{array}\right], \quad
\left[\mathbf{R}_\varepsilon^k\right] = \left[\begin{array}{c|c}
\left[\mathbf{R}_\varepsilon^k\right]_{(1,2,6)} & \mathbf{0} \\
\hline
\mathbf{0} & \left[\mathbf{R}_\varepsilon^k\right]_{(4,5)}
\end{array}\right]. \quad (2.34)
$$

The plate formulation applies for each layer k, in the structural basis $(\mathbf{x}, \mathbf{y}, \mathbf{z})$,

$$
\left\{\begin{array}{c}
\mathbf{N} \\
\mathbf{M} \\
\mathbf{Q}
\end{array}\right\}_k = \begin{bmatrix}
\mathbf{A}_k' & \mathbf{B}_k' & \mathbf{0} \\
\mathbf{B}_k' & \mathbf{D}_k' & \mathbf{0} \\
\mathbf{0} & \mathbf{0} & \mathbf{H}_k'
\end{bmatrix} \left\{\begin{array}{c}
\boldsymbol{\varepsilon}^m \\
\boldsymbol{\kappa} \\
\boldsymbol{\gamma}
\end{array}\right\}. \quad (2.35)
$$

That is to say, with Reissner-Mindlin's plate assumptions,

$$
\left\{\begin{array}{c}
N_x \\
N_y \\
N_{xy}
\end{array}\right\}_k = \int_{z_{k-1}}^{z_k} dz \left[\mathbf{q}_\mathbf{p}'\right]_k \left\{\begin{array}{c}
u_{x,x} \\
u_{y,y} \\
u_{x,y} + u_{y,x}
\end{array}\right\}
$$

$$
+ \int_{z_{k-1}}^{z_k} z\, dz \left[\mathbf{q}_\mathbf{p}'\right]_k \left\{\begin{array}{c}
\beta_{x,x} \\
\beta_{y,y} \\
\beta_{x,y} + \beta_{y,x}
\end{array}\right\}, \quad (2.36)
$$

Modeling of a viscoelastic honeycomb panel equipped with piezoelectric patches in view of vibroacoustic active control design

$$
\left\{ \begin{array}{c} M_x \\ M_y \\ M_{xy} \end{array} \right\}_k = \int\limits_{z_{k-1}}^{z_k} z^2\, dz\, \left[\mathbf{q'_p} \right]_k \left\{ \begin{array}{c} \beta_{x,x} \\ \beta_{y,y} \\ \beta_{x,y} + \beta_{y,x} \end{array} \right\}
$$

$$
+ \int\limits_{z_{k-1}}^{z_k} z\, dz\, \left[\mathbf{q'_p} \right]_k \left\{ \begin{array}{c} u_{x,x} \\ u_{y,y} \\ u_{x,y} + u_{y,x} \end{array} \right\}, \tag{2.37}
$$

$$
\left\{ \begin{array}{c} Q_{yz} \\ Q_{xz} \end{array} \right\}_k = \frac{5}{6} \int\limits_{z_{k-1}}^{z_k} dz\, \left[\mathbf{q'_t} \right]_k \left\{ \begin{array}{c} \beta_y + w_{,y} \\ \beta_x + w_{,x} \end{array} \right\}, \tag{2.38}
$$

with z_k defined on Figure 2.3. And where one distinguishes the reduced in-plane elastic coefficients q_{ij} and q'_{ij} for $i,j = 1,2,6$ in matrices $\left[\mathbf{q^E_p} \right]_k$, $\left[\mathbf{q'^E_p} \right]_k$ and transverse shear elastic coefficients for $i,j = 4,5$ in matrices $\left[\mathbf{q^E_t} \right]_k$, $\left[\mathbf{q'^E_t} \right]_k$. For a symmetric laminate meshed on its mid-plane($z_0 = -\frac{h}{2}$), $\left[\mathbf{B^k} \right]$ and thus the second term of the sums (2.36) and (2.37), are equal to zero.

The application of the first-order plate theory to a multilayered laminate is now very classical, one can cite, for example, books by Jones [13] and Berthelot [18]. The global laminate stress resultants are the sum of every k-layer stress resultant in the structural basis $(\mathbf{x}, \mathbf{y}, \mathbf{z})$. The stiffness coefficients $(q'_{ij})_k$ are constant but can be different from one layer to another, and the displacements u, v, w and the slopes β_x and β_y are not functions of z. Thus the laminate stress-strain relation is

$$
\left\{ \begin{array}{c} \mathbf{N} \\ \mathbf{M} \\ \mathbf{Q} \end{array} \right\} = \left[\begin{array}{ccc} \mathbf{A} & \mathbf{B} & \mathbf{0} \\ \mathbf{B} & \mathbf{D} & \mathbf{0} \\ \mathbf{0} & \mathbf{0} & \mathbf{H} \end{array} \right] \left\{ \begin{array}{c} \boldsymbol{\varepsilon}^{\mathbf{m}} \\ \boldsymbol{\kappa} \\ \boldsymbol{\gamma} \end{array} \right\}. \tag{2.39}
$$

with

$$
[\mathbf{A}] = \sum_{k=1}^{N} \left[\mathbf{R^k_\sigma} \right]^{-1}_{(1,2,6)} [\mathbf{q_p}]_k \left[\mathbf{R^k_\varepsilon} \right]_{(1,2,6)} (z_k - z_{k-1}), \tag{2.40}
$$

$$
[\mathbf{B}] = \frac{1}{2} \sum_{k=1}^{N} \left[\mathbf{R^k_\sigma} \right]^{-1}_{(1,2,6)} [\mathbf{q_p}]_k \left[\mathbf{R^k_\varepsilon} \right]_{(1,2,6)} (z_k^2 - z_{k-1}^2), \tag{2.41}
$$

$$
[\mathbf{D}] = \frac{1}{3} \sum_{k=1}^{N} \left[\mathbf{R^k_\sigma} \right]^{-1}_{(1,2,6)} [\mathbf{q_p}]_k \left[\mathbf{R^k_\varepsilon} \right]_{(1,2,6)} (z_k^3 - z_{k-1}^3), \tag{2.42}
$$

$$
[\mathbf{H}] = \frac{5}{6} [\mathbf{F}] = \sum_{k=1}^{N} \frac{5}{6} \left[\mathbf{R^k_\sigma} \right]^{-1}_{(4,5)} [\mathbf{q_t}]_k \left[\mathbf{R^k_\varepsilon} \right]_{(4,5)} (z_k - z_{k-1}). \tag{2.43}
$$

A simple extension of the single ply dependence on offset (2.30), clearly shows that the constitutive law of a laminate is a polynomial function of $1, x_3(0), x_3(0)^2$.
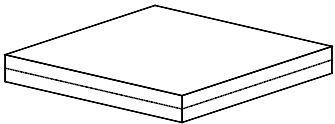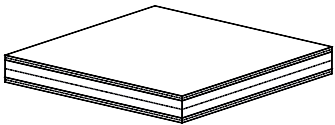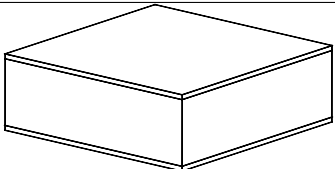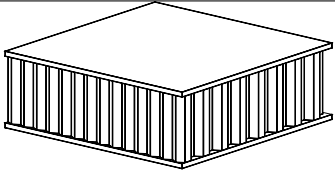
2.3   Review of existing modeling of honeycomb core sandwich composites

2.3.1   Sandwich composite modeling

To predict sandwich composite static or dynamic behavior, researchers have developed many models. An extensive review of computational models for sandwich panels and shells has been made by Noor and Burton [7]. Sandwich models are classified into three-dimensional detailed models, three-dimensional continuum models and two-dimensional plate and shell models.

Table 2.2 summarizes the different approaches for vibration of honeycomb core sandwiches, and gives a non-exhaustive list of corresponding references.

Table 2.2: *Models for vibration of honeycomb sandwich plates (or beams)*

		Models	References
2D		Global approximation model (equivalent single-layer model)	[19, 16, 20]
		Discrete-layer model (layerwise or zig-zag)	[1, 21]
3D		3D continuum model	[22, 23, 24, 25]
		3D detailed model	[22, 25, 26, 4]

The detailed 3D finite element model represents the actual geometry of the honeycomb core, as well as the adhesive and face sheet layers. Chamis, Aiello and Murthy [22] first carry out in 1986, with MSC/NASTRAN, a total 3D detailed FEM of metallic honeycomb core sandwich plate, with the intention of predicting honeycomb core properties. More

recently Al Bachi [4] developed a similar FEM with ANSYS software. The two detailed 3D FEM quoted have been implemented for static behavior preditions. In addition, Noor and Burton [26] suggest to use such models for predicting the free-vibration response of sandwich panels.

In the 2D global approximation model, also called equivalent single-layer model, the whole sandwich is replaced by a single equivalent layer with global through-the-thickness approximations for displacements, strains and/or stresses. It corresponds to variations of the theory presented in Section 2.2.3. Methods can be classified depending of their ability to describe, with more or less details, the shear phenomenon in soft layers of the sandwich, such as viscoelastic layer, and honeycomb core. These variations are often fairly strong so that the approach is difficult to generalize.

The largest class of extensions considers discrete-layer models, or layerwise or zig-zag models, where the sandwich is divided into several layers and each layer is modelled based on a chosen theory. In layerwise models, all layers are modeled on the basis of plate/shell theory using Kirchhoff-Love, Reissner-Mindlin or enriched kinematic assumptions.

3D continuum models are multilayer models that use plates or shells to model hard layers (skins) and volumes to model soft ones (cores or viscoelastic layers). Figure 2.5 shows a typical 3D layered FE model with shell elements for the face sheets and solid volume elements for the core. In the figure, separate nodes are introduced for the face-sheets and the core with rigid links between the two. It should be noted, and will be used in Section 5.5.1, that this has exactly the same kinematics as a model that would consider an offset for the face sheets, and thus a single layer of nodes. Two layers of nodes are used here to simplify the meshing and post-processing simulations. This approach, used in the present work, is found in the litterature to model honeycombs [22, 24] and has also been used to model thin viscoelastic layers by Plouin [23]. In the following, the designation Shell-Volume-Shell (SVS) FE model is used for this model.
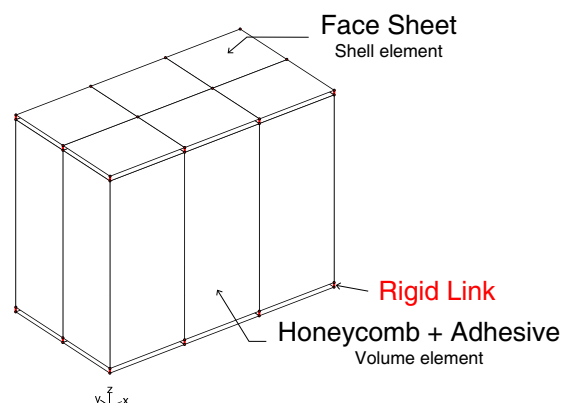
Figure 2.5: *3D continuum model definition*

Modeling of a viscoelastic honeycomb panel equipped with piezoelectric patches in view of vibroacoustic active control design

In the case of thin viscoelastic layers, Plouin and Balmès [23] have shown that the first-order shear theory is not adequate to accurately describe the high shear deformations inside the core, independently of the choice of shear correction factors. The critical aspect is there to allow the relative in-plane motion of the skins. Clearly the introduction of a volume layer enables this motion and the model is correct.

Ref. [23] also shows that shear locking for bending motion, typically expected for first order volume elements is actually not present even for very poor aspect ratios because the energy is essentially in shear and not bending. This is in good part due to the fact that the Young's modulus of the viscoelastic material of the core is usually 10^3 times lower than the skins material modulus, as observes Moreira [1]. For honeycombs, the core is much thicker so that volume elements no longer have poor aspect ratios and locking is not an issue.

In the case of honeycombs, the level of shear in the honeycomb is also very different from that in the skin, hence the need for a layered approach arises. Futhermore, the volume is assumed to be made of an orthotropic material to account for the differences of properties in various directions generated by the honeycomb manufacturing process. The estimation of the orthotropic properties will be discussed extensively in Section 2.3.2.

When looking at the kinematics of the SVS model, it is fairly obvious that the compression of the core plays a very minor role so that a single vertical DOF is really needed. Similarly, knowing the in-plane motion of one layer, one can use the out of plane shears to estimate the in-plane motion of the next layer using the condition that motion is continuous at interfaces. This is the basis of the zig-zag or layerwise theory [21]. Using the Moreira's notations [1] corresponding to figure 2.6, one thus assumes

$$
\{\mathbf{U}\}_k = \left\{ \begin{array}{l} U_k = u_0(x,y) + \frac{h_1}{2}\beta_1^x + \sum_{j=2}^{k-1} h_j \beta_j^x + \frac{h_k}{2}\beta_k^x + z_k \beta_k^x \\[2mm] V_k = v_0(x,y) + \frac{h_1}{2}\beta_1^y + \sum_{j=2}^{k-1} h_j \beta_j^y + \frac{h_k}{2}\beta_k^y + z_k \beta_k^y \\[2mm] W_k = w_0(x,y) \end{array} \right\}, \tag{2.44}
$$

where

- h_k is the thickness of the k-layer,

- u_0, v_0, w_0 are the displacements of the reference layer (k=1),

- U_k, V_k, W_k the displacements field of the k-layer,

- β_k^x, β_k^y are slopes of the normal about the **y** and **x** axes respectively.
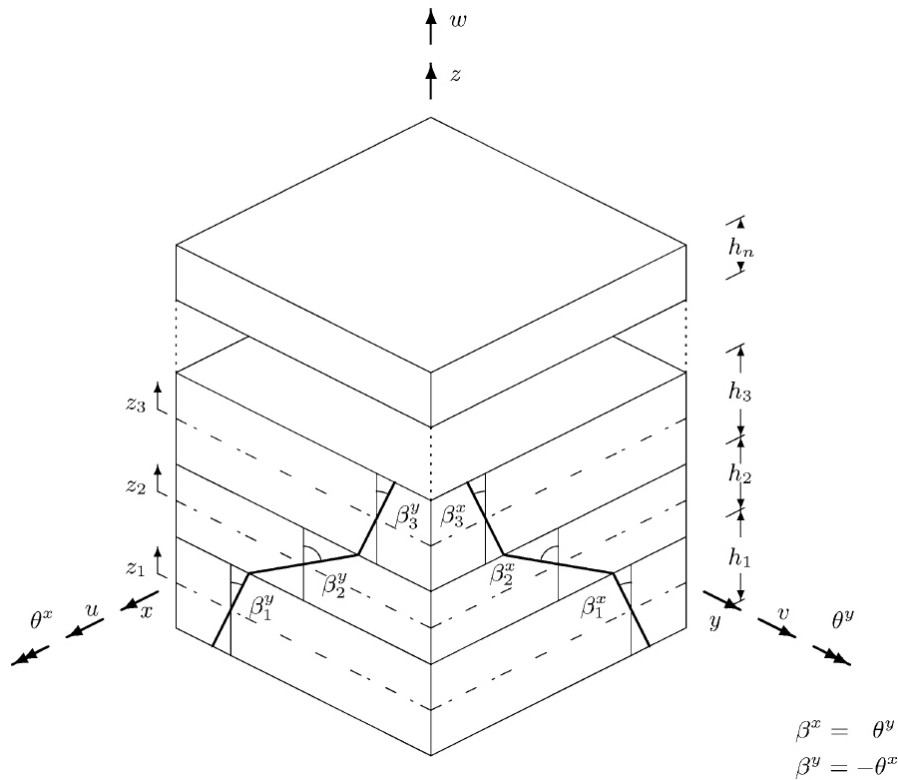
Figure 2.6: *Layerwise theory - Moreira's kinematic model [1]*

Various authors motivate the need for these developments by underlining the lower degrees of freedom (DOF) number (the classical 5 of a plate for the base layer plus shears 2 per other layer). A model alternating shell and volume, will use 5 per shell layer and 6 per volume layer. But the connections between shell and volume eliminate all the volume DOFs. As a result, the layerwise model really only has one less DOF for a 3 layers sandwich. It should however be clear that the difference in formulation is very small and essentially limited to the numerical integration strategy through the thickness.

The position taken by Balmès for the development of the viscoelastic vibration toolbox [27] and the underlying research is that the extra work of developing specific multilayer elements is enormous compared to the marginal gain in computational cost. In particular models using multiple layers of elements can use standard FEM solvers and pre/post-processing, while special zig-zag formulations need intensive developments and have thus only been developed within specialized applications.

2.3.2   Honeycomb core material properties estimation

For all models, the knowledge of material parameters is an important issue. The reliability of the response predictions of the computational models for sandwich plates is critically dependent on the accurate characterization of the properties of the face sheets, core and adhesive layers, what Noor and Burton have underlined in [7]. In the case of honeycomb core sandwich, modeling the core is itself a difficulty because of the high heterogeneity of the structure.

The honeycomb core is a periodic structure in two orthotropic directions. The direction of the ribbon, longitudinal, usually referred by L (length), here *x*-direction, and transverse direction, referred by W (width), here *y*-direction. The orthotropy is due to the manufacturing process. Indeed after being shaped, the ribbons are bonded, hence the *x*-direction cell walls are twice thicker than the *y*-direction walls. The cells are hexagonal shaped in this study, but different honeycomb shapes exist.

For reasons of numerical efficiency, classically the honeycomb core is replaced by a homogeneous equivalent core (volume layer of the SVS FE model). To assess its elastic properties, sandwich composite can be treated with a global one layer 2D model as Saito and al. do on an aluminum honeycomb panel [19], or with a multi-layered, 2D or 3D models. The attention has been focused on the 3D multi-layered approach, whereby the pure honeycomb core material is considered. The influence of skins and bonding on the estimation of the equivalent honeycomb core properties will be discussed in Section 3.4.
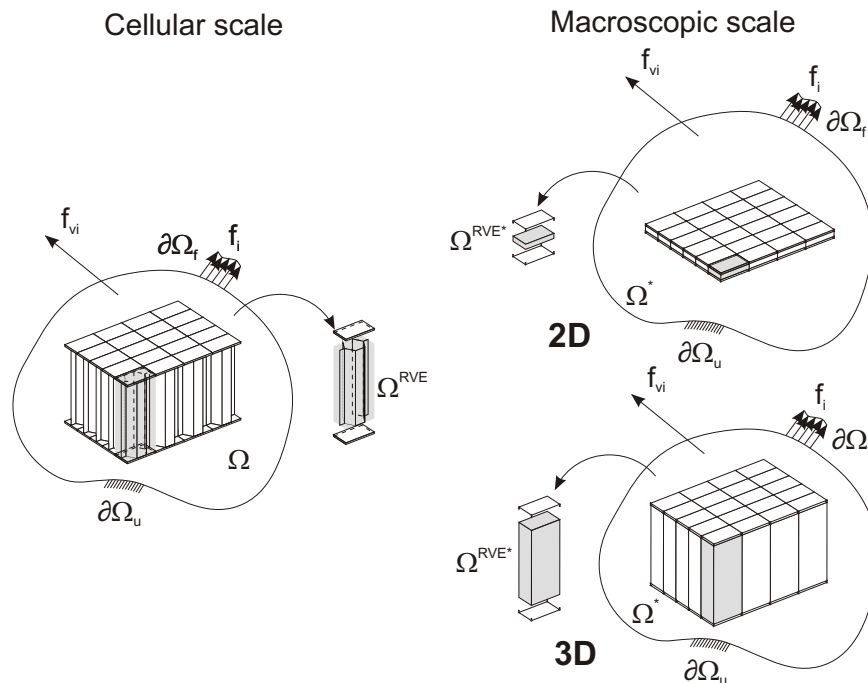
Figure 2.7: *Simplification process for actual cellular scale to equivalent macroscopic scale, according Hohe's diagram in [2]*
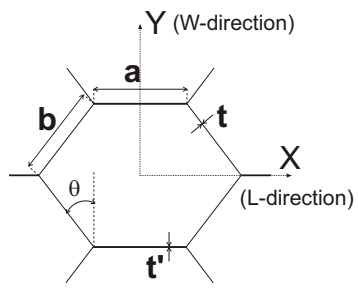
Honeycomb core equivalent orthotropic properties, will be called *effective properties* and referred with a superscript star (*), according to homogenization theory. Thus orthotropic material law (2.45) depends on 9 independent material parameters, the Young's moduli $E_x^\star$, $E_y^\star$, $E_z^\star$, Poisson's ratios $\nu_{yx}^\star$, $\nu_{zx}^\star$, $\nu_{zy}^\star$, and shear moduli $G_{xy}^\star$, $G_{xz}^\star$, $G_{yz}^\star$. For further details, see Berthelot's book [18].

$$
\left\{
\begin{array}{c}
\varepsilon_x \\
\varepsilon_y \\
\varepsilon_z \\
\gamma_{yz} \\
\gamma_{xz} \\
\gamma_{xy}
\end{array}
\right\}
=
\left[
\begin{array}{cccccc}
1/E_x^\star & -\nu_{yx}^\star/E_y^\star & -\nu_{zx}^\star/E_z^\star & 0 & 0 & 0 \\
-\nu_{xy}^\star/E_x^\star & 1/E_y^\star & -\nu_{zy}^\star/E_z^\star & 0 & 0 & 0 \\
-\nu_{xz}^\star/E_x^\star & -\nu_{yz}^\star/E_y^\star & 1/E_z^\star & 0 & 0 & 0 \\
0 & 0 & 0 & 1/G_{yz}^\star & 0 & 0 \\
0 & 0 & 0 & 0 & 1/G_{xz}^\star & 0 \\
0 & 0 & 0 & 0 & 0 & 1/G_{xy}^\star
\end{array}
\right]
\left\{
\begin{array}{c}
\sigma_x \\
\sigma_y \\
\sigma_z \\
\tau_{yz} \\
\tau_{xz} \\
\tau_{xy}
\end{array}
\right\}
\quad (2.45)
$$

The effective parameters are estimated as function of the cells geometric characteristics (a, b, t, t', θ) and the constitutive material parameters (E, G, ρ, ν).

Table 2.3: *Definition of honeycomb core geometric parameters and material properties*

Constitutive Material parameters		Geometric parameters	
E	Young's modulus	a	length of cell side (L or *x*-direction)
G	Shear modulus	b	length of sloping cell side
ρ	Density	θ	angle of cell
ν	Poisson's ratio	t & t'	thickness of simple & double cell wall

An extensive literature review on existing methods to determine the equivalent honeycomb core properties is presented by Noor in [7], and more recently by Schwingshackl in [12].

In 1958, Kelsey [11] first provided a set of equations for $G_{xz}^\star$ and $G_{yz}^\star$ based on energy methods applied on the honeycomb cell walls. Gibson and Ashby extended this analytical approach to derive all the nine orthotropic parameters, and their book [3] is nowadays the standard reference work in the field. However, the analytical solutions proposed do not take into account the double thickness walls in the direction of the ribbon (L), and do not agree well with experimental results, thus numerous researchers still continue working on improving the estimation of the honeycomb core effective parameters.

Literature searches bring out three main approaches to estimate core effective properties, which differ by the size of the representative element chosen to estimate the whole structure properties:

1. considerations on the deformations of a cell wall, [11, 3, 28, 29],

2. application of homogenization theory on a representative volume element (RVE = one representative cell) [30, 31, 32, 33, 2],

3. use of numerical tests on a beam or panel (more than one cell in x and y-directions) [22, 4, 26, 25] .

The first approach is the one presented by Kelsey [11], and enriched by Gibson and Ashby [3]. For the in-plane properties calculation, a hexagonal unit cell is forced to deform under loadings in **x** and **y** directions (see Figure 2.8). The standard beam theory is used, and the constitutive material of the cells is considered as linear, elastic and isotropic material.
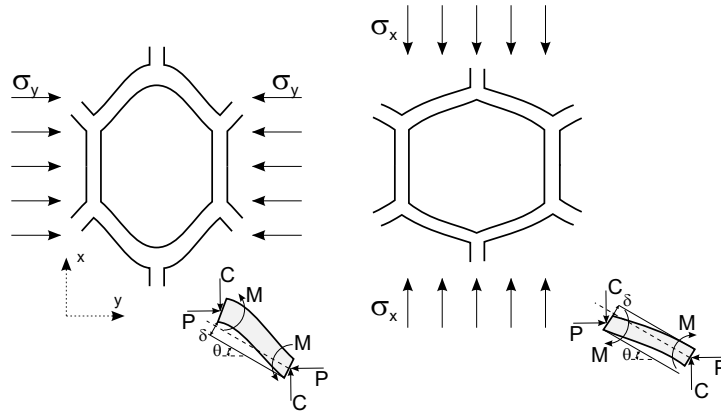
Figure 2.8: *Kelsey, Gibson and Ashby's model for analytic estimation [3]*

To estimate the Young's modulus $E_x^\star$, a stress σ_x parallel to **x** is applied to a cell. The wall deflection is calculated by standard beam theory, under pure bending stress assumption, and the strain ε_x is inferred. The Young's modulus parallel to **x** is given by $E_x^\star = \sigma_x/\varepsilon_x$. The same is done in y-direction to calculate $E_y^\star$.

Like the Young's moduli, the in-plane shear modulus $G_{xy}^\star$ is calculated by the ratio τ_{xy}/γ_{xy}.

The Poisson's ratio is deduced by the negative ratio of the strains normal to, and parallel to, the loading direction, $\nu_{xy}^\star = -\varepsilon_y/\varepsilon_x$ and $\nu_{yx}^\star = -\varepsilon_x/\varepsilon_y$. By reciprocity, $\varepsilon_x\nu_{yx}^\star = \varepsilon_y\nu_{xy}^\star$.

Such method cannot be applied for out-of-plane shear moduli. Due to the complexity of stress distribution in a sheared honeycomb, the exact analytical calculation of $G_{xz}^\star$ and $G_{yz}^\star$ is not possible. Theorems of minimum potential energy and minimum complementary energy allow estimating their lower and upper bounds.

The lower and upper bounds of $G^\star_{yz}$ are equal, but energy methods only give the range of $G^\star_{xz}$ as function of constitutive material shear modulus G and geometric parameters, see details in ref. [3, 26].

To refine the previous shear moduli estimation, Grediac [28] suggests to take into account the non uniformity of the stress fields in the cell walls. He considers a basic cell by FE method (see Figure 2.9). Then, Meraghni [29] adapts Grediac's approach to determine $E^\star_z$ and extends it for a non hexagonal core.
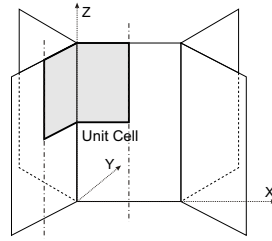
Figure 2.9: *Grediac and Meraghni's representative unit of honeycomb for numerical estimation*

The Young's modulus $E^\star_z$ is the constitutive material Young's modulus E scaled to the effective area which support the normal loading in z-direction.

The out-of-plane Poisson's ratios are equal to the constitutive material Poisson's ratio ν. By reciprocity, $\nu^\star_{xz} = \frac{E^\star_x}{E^\star_z}\nu$ and $\nu^\star_{yz} = \frac{E^\star_y}{E^\star_z}\nu$.

The Gibson and Ashby's formulas, adapted to take the thickness of the inclined cell wall $t' \neq t$ into account, are gathered in Table 2.4.

Table 2.4: *Gibson and Ashby's formulas of honeycomb core stiffness coefficients*

In-plane (**x,y**) parameters		Out-of-plane parameters	
$E^\star_x$	$E\left(\dfrac{t}{b}\right)^3 \dfrac{\frac{a}{b}+sin\theta}{cos^3\theta}$	$E^\star_z$	$\dfrac{E}{b}\dfrac{2t+\frac{a}{b}t'}{\left(\frac{a}{b}+sin\theta\right)cos\theta}$
$E^\star_y$	$E\left(\dfrac{t}{b}\right)^3 \dfrac{cos\theta}{(\frac{a}{b}+sin\theta)sin^2\theta}$	$G^\star_{yz}$	$G\dfrac{t}{b}\dfrac{cos\theta}{\frac{a}{b}+sin\theta}$
$G^\star_{xy}$	$\dfrac{E}{b^3}\dfrac{\frac{a}{b}+sin\theta}{\left(\frac{a}{b}\right)^2\left(\frac{1}{t'^3}+\frac{2a}{bt^3}\right)cos\theta}$	$G^\star_{xz}$	Up: $\dfrac{G}{b}\dfrac{\frac{a}{b}t'+2tsin^2\theta}{2cos\theta\left(\frac{a}{b}+sin\theta\right)}$
			Low: $\dfrac{G}{b}\dfrac{\left(\frac{a}{b}t'+tsin\theta\right)^2}{cos\theta\left(\frac{a}{b}+sin\theta\right)\left(2\frac{a}{b}t'+t\right)}$
$\nu^\star_{xy}$	$\dfrac{(\frac{a}{b}+sin\theta)sin\theta}{cos^2\theta}$	$\nu^\star_{zx}$	ν
$\nu^\star_{yx}$	$\dfrac{cos^2\theta}{(\frac{a}{b}+sin\theta)sin\theta}$	$\nu^\star_{zy}$	ν

The Density of the honeycomb core, $\rho^\star$, is calculated for a representative volume of honeycomb, see Figure 2.10. $\rho^\star$ depends on basic material density ρ and on geometric parameters,

$$\rho^\star = \frac{\rho(at' + 2bt)}{2bcos\theta\,(a + bsin\theta)}. \tag{2.46}$$

Representative volume
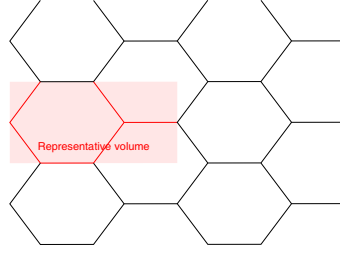
Figure 2.10: *Representative Volume*

The second approach uses homogenization theory on a representative volume element of the structure, typically one cell of the honeycomb. The principle of homogenization theory is to perform a change of scale by replacing a complex microstructure Ω (here cellular structure), by a homogenized *effective* medium $\Omega^\star$. The effective medium $\Omega^\star$ is assumed to be mechanically equivalent at the macroscopic level to the cellular structure Ω, see Figure 2.7.

Homogenization of periodic media applies to honeycomb core, assumed to be periodic in *x* and *y*-directions. The equivalent material properties of a periodic structure can be evaluated by homogenizing a basic cell Ω^{RVE} , also called representative volume element (RVE), see Figure 2.11 for examples of basic cells. In addition to the same external boundary conditions applied on Ω and $\Omega^\star$, Ω^{RVE} and $\Omega^{RVE\star}$ have the same periodic conditions on their displacement fields.

According to this theory, Shi [30] proposes to evaluate the out of plane shear modulus $G_{zx}^\star$ by calculating the average transverse shear stress from the cellular-RVE and the corresponding macro-RVE

$$\langle\tau_{zx}\rangle = \frac{1}{V}\int_{\Omega_h} \tau_{zx}dxdy \tag{2.47}$$

$$\langle\tau_{zx}\rangle = G_{zx}^\star\gamma_{zx} \tag{2.48}$$

with $\Omega = h * \Omega_h$, *h* the thickness of honeycomb core layer, and *V* the volume of the RVE.

The method using the strain energy based RVE-procedure is presented by Hohe and Becker [33] and applied by Gornet [31] with the finite element code Cast3M-CEA for an application to trimaran structures. The method uses Hill-Mandel's theorem, according to which the macroscopic energy of the RVE is equal to the mean of the each constitutive

element of the RVE energy.

$$\langle Tr(\boldsymbol{\sigma}\boldsymbol{\varepsilon})\rangle = \frac{1}{V}\int\limits_{\Omega^{RVE}} Tr(\boldsymbol{\sigma}\boldsymbol{\varepsilon})dV = \frac{1}{V}\int\limits_{\Omega^{RVE\star}} Tr(\boldsymbol{\sigma}^{\star}\boldsymbol{\varepsilon}^{\star})dV^{\star} = \langle Tr(\boldsymbol{\sigma}^{\star}\boldsymbol{\varepsilon}^{\star})\rangle \qquad (2.49)$$

Moreover, the macroscopic equivalence of the strain states ε_{ij} and $\varepsilon_{ij}^{\star}$ is assumed if the volume average of strain states is equal,

$$\langle \varepsilon_{ij}\rangle = \frac{1}{V}\int\limits_{\Omega^{RVE}} \varepsilon_{ij}dV = \frac{1}{\Omega}\int\limits_{\Omega^{RVE*}} \varepsilon_{ij}^{\star}dV^{\star} = \langle \varepsilon_{ij}^{\star}\rangle . \qquad (2.50)$$

The homogenization process consists in deforming Ω and $\Omega^{\star}$ by independent reference strain states which satisfy the equation (2.50). The total strain energy densities for both volume, $Tr(\boldsymbol{\sigma}\boldsymbol{\varepsilon})$ and $Tr(\boldsymbol{\sigma}^{\star}\boldsymbol{\varepsilon}^{\star})$, are computed. Then knowing the relation $\sigma_{ij}^{\star} = c_{ijkl}^{\star}\varepsilon_{kl}^{\star}$, between the strain and the stress components, the effective elasticity tensor $c_{ijkl}^{\star}$ is chosen to satisfy the equation (2.49) for every strain state. See application of this approach in ref. [33].

Shi's basic cell [30]   Gornet's meshing of RVE [31]
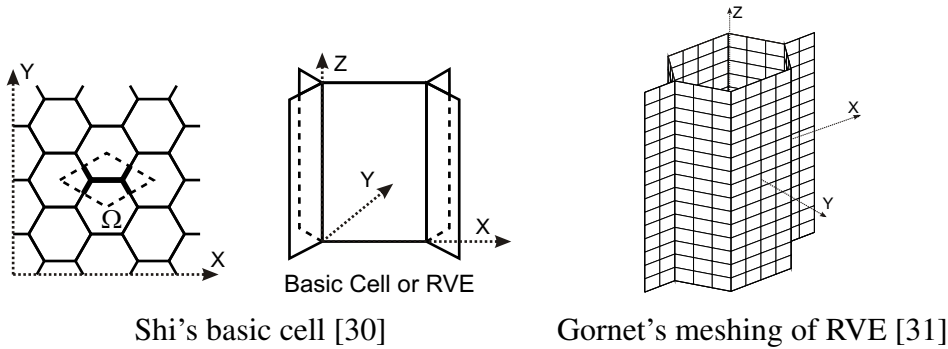
Figure 2.11: *Representative Volume Element for homogenization theory*

The third approach is based on numerical tests on a bigger specimen of honeycomb core sandwich. Despite the expensive computation time of a 3D detailed FE analysis, numerical simulations are performed, for different boundary and loading conditions, with aim of elastic core parameters estimation.

Chamis [22] first carries out a total 3D detailed FEM of honeycomb core sandwich. His approach consists in generating by MSC/NASTRAN four models with computational levels of sophistication in order to compare them in static conditions. The four models correspond to those listed in Table 2.2.

Considering a representative volume element (RVE) size of 3D detailed FEM of the honeycomb, the equivalent properties of the honeycomb core are determined by loading the model with imposed displacements in each direction at one face while fixing the opposite face, as shown on Figure 2.12 along *x*-direction. Chamis demonstrates that the

honeycomb core behaves like an equivalent homogeneous anisotropic solid. Such an approach has been implemented by Al Bachi [4] with ANSYS software on a 40-cells RVE and compared to the Gibson and Ashby's parameters formulation. Al Bachi concludes on a good agreement of the analytic and numerical methods.
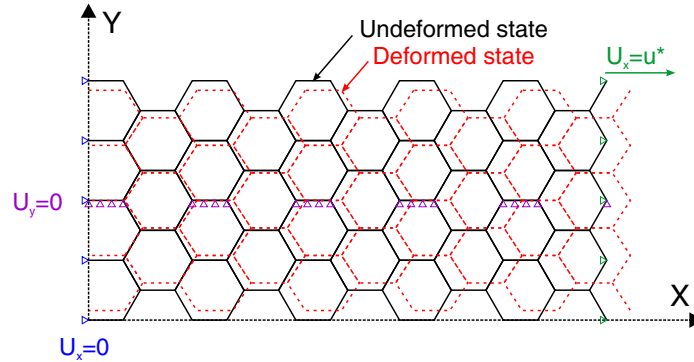
Figure 2.12: *Numerical simulation of a tensile stress along x-direction on the Representative Volume Element, according Al Bachi's diagram in [4]*

Similarly, 3D detailed model can be used to predict the equivalent honeycomb core properties in dynamic conditions.

Noor and Burton [26] present a method using a detailed 3D finite element model, built in ANSYS, as standard of comparison to assess the accuracy of the equivalent homogeneous core model, for the dynamic behavior prediction of the honeycomb core sandwich. They compare the free-vibration responses predicted by equivalent continuum models, with properties estimated through the first approach [11, 3], and detailed 3D FE models. Using the free-vibration frequencies as comparison criterion, they consider infinitely long panels in *x* or *y*-directions and rectangular panels. Their approach consists in considering the minimum vibration frequencies obtained with several number of cells models.

Schwingshackl and al. recall in [12] that the out of plane shear moduli of the core, $G^\star_{xz}$ and $G^\star_{yz}$, and the Young's modulus of the skins E_f, are the most influent parameters on the dynamics of the sandwich. This will be verified in Section 3.4.2. Thus, the comparison of the different approaches focuses on the transverse shear moduli of the honeycomb core, the quoted approaches are numerically compared in Table 3.4, for the test case of Aluminum-Nomex specimen (AN20 Table 3.2).

Chapter 3

A numerical evaluation of honeycomb core equivalent properties

Contents

3.1   Introduction

The literature review in Section 2.3 showed that the determination of equivalent parameters, particularly the transverse shear moduli, was a key difficulty in the modeling of honeycomb using equivalent shell/volume/shell models.

The many approaches implemented to estimate the equivalent (or effective) parameters use similar principles: a representative volume of honeycomb is submitted to loads and distortion is evaluated. Strategies to improve precision involve

- taking a bigger representative volume, a sample of several honeycomb cells instead of a unique representative cell,

- considering the non uniformity of the deformation in the cell wall,

- taking into account the boundary conditions fixed by the face sheets and adhesive layer, and

- varying the type of solicitation.

The objective of this chapter is to propose a general numerical methodology to evaluate effective parameters automatically, and in the process gain, a better understanding of the range of validity of the equivalence, for dynamic applications. The principle retained is to correlate the frequencies of waves propagating in the honeycomb at various wavelengths for a detailed 3D FE model and the equivalent SVS FE model. This can be seen as a numerical homogeneization procedure based on an automated model updating.

The first issue, addressed in section 3.2, is to generate a parametric description of the honeycomb.

Ideally, an accurate geometry of the honeycomb cell and constituent material properties are known and are used to generate a detailed 3D FE model. A key aspect is that the numerical nature of the proposed procedure makes it possible to account for any level of detail (geometries of the cells, properties of the adhesive, ...). For practical system level computations, the classical shell/volume/shell (SVS) representation of honeycomb panels is really used. Section 3.2.1 introduces a sample 3D FE model, that will be used throughout the chapter, and gives details about the SVS model implementation.

In a numerical homogeneization procedure, constitutive parameters will be varied to minimize an objective function, the rest of section 3.2 thus details methodologies used to handle model parameterization.

The principle of homogeneization procedures is to seek parameters that lead to identical responses in a detailed (3D FEM here) and an equivalent simplified model (SVS model here). In the many possibilities, it was chosen here to focus on the frequency of periodic modes, thus leading to the procedure outlined in Figure 3.1.

In a spatially periodic medium, propagating waves of a given wavelength only occur at certain frequencies and correspond to periodic modes. The parameters of detailed and simplified models can be adjusted so that these frequencies are equal for both models. For a unit kinetic energy, the strain energy is equal to the square of the wavelength/mode
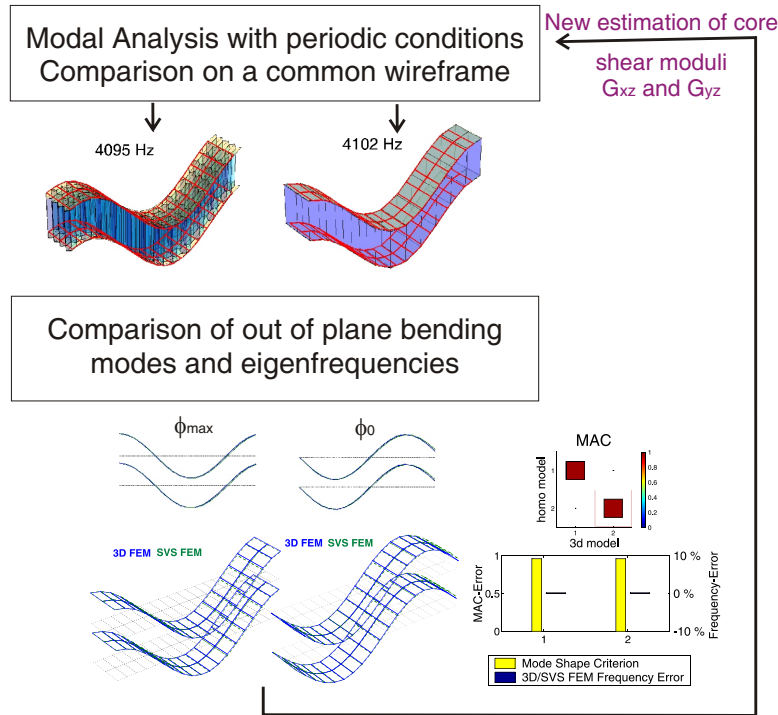
Figure 3.1: *Procedure of numerical identification by correlation of periodic modes*

frequency. Updating frequencies is thus strictly equivalent to equating strain energy levels, which is more classically given as equivalence in homogeneization procedures. The novelty of the approach is that multiple wavelengths are considered, so that the results are not found for a single representative volume but for a range.

Section 3.3 discusses computation and correlation issues associated with periodic modes. Meshes of a honeycomb beam can be used with simple periodic conditions. But the approach gives only a few periodic modes and becomes very expensive for refined 3D FEM. Fourier / Floquet theory allows rapid computations with using the representative volume element (or twice that volume as classically done to represent complex components).

The equivalence of detailed and simplified models depends on the ability of the simplified model to represent the appropriate behavior. Section 3.4 thus presents an analysis of constituent properties and their influence on panel vibrations. After detailing the properties of the chosen panel, the section analyzes the evolution of energy fractions as a function of wavelength and demonstrates that the only significant parameters for the core are the density, which can be evaluated from geometric considerations, and the transverse shear moduli $G_{xz}^\star, G_{yz}^\star$. Other effective parameters are estimated using formulas of Gibson and Ashby [3], recalled in Table 3.1 with $t' = 2t$, but have a very minor impact on periodic modes. Finally, the influence of glue and local bending in the cell walls is also discussed.

Periodic bending modes in the longitudinal and transverse directions are thus only dependent on known parameters and the unknown equivalent $G_{xz}^\star$ and $G_{yz}^\star$ respectively. As illustrated in section 3.5.1, one can estimate these parameters by a straightforward

optimization finding the modulus associated with matching periodic mode frequencies. The validation of the effective parameters is done for a panel in free-free conditions in Section 3.5.2.

The proposed procedure considers the whole sandwich including skins, section 3.5.3 verifies the range of wavelengths where the effective parameters are indeed independent of skin properties and thus intrinsic characteristics of the core.

In practice, neither geometry nor properties may be well known. In the present work, the properties of the Nomex paper and the exact nature of the glue used for bonding were not known. Furthermore, the variability in the glue filet geometry could not be evaluated. The process introduced in this chapter would thus eventually be used as a bijection between effective core properties and constituent parameters, with either being evaluated from correlation with experiments such as the modal tests that will be presented in Chapter 4. To illustrate this process, section 3.5.4 discusses a procedure to estimate glue properties.

3.2   Physical and equivalent models

This section discusses finite element models of the honeycomb and their parameterization. A 3D model is introduced to represent basic constituent properties. The classical shell/volume/shell (SVS) model is introduced for practical simulations. The estimation of effective parameters of this model is a key issue of this chapter.

3.2.1   3D models of honeycomb core sandwich

The first model, that will be referred to as the *3D FE model*, is built to represent the physical reality (geometry, thickness, material...) as closely as possible, with the intention of minimizing the modeling errors. This model will be used as reference to estimate honeycomb properties starting from material and geometric considerations.
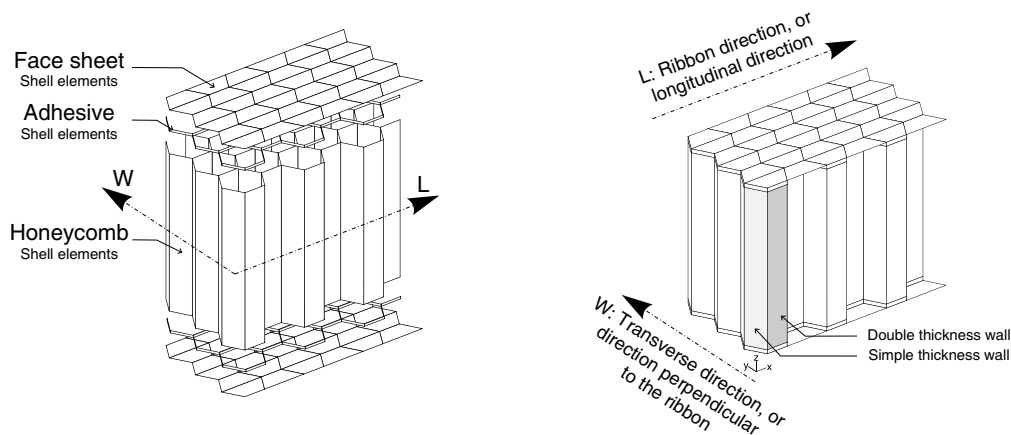
Figure 3.2: *Definition of the 3D finite element model*

The geometry of the glue is shown in Figure 3.3. Rather than introducing a detailed geometry, the model considered here privileges a functionally equivalent representation as a small massless plate extending from the skin neutral fiber to its surface. The explicit representation of glue elements thus allows a meshing of the honeycomb cell walls and face-sheets that is compatible and strictly respects the geometry. The free constitutive parameters E_g and the shell thickness t_g can be directly related to the functional values of shear and bending stiffness, this will be discussed in section 3.4.3.
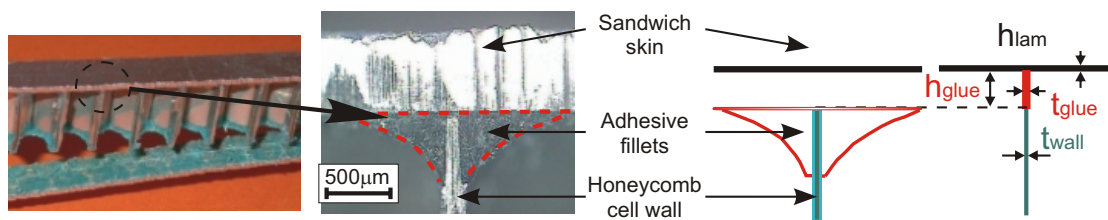
Figure 3.3: *Modeling of adhesive fillet*

The second model, shown in figure 3.4 and designated by SVS (shell/volume/shell) model, with the core composed of a volume element of orthotropic material is then classically considered since such a model is necessary to allow predictions of large panels. The estimation of the effective parameters of the orthotropic material from geometric and material data of the true honeycomb is a key objective of this chapter.
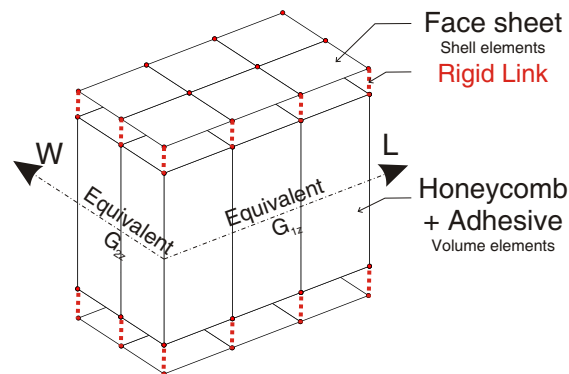
Figure 3.4: *Geometry of the Shell Volume Shell (SVS) model*

The sandwich face sheets are modeled by isotropic shell, for metallic skin such as aluminum, or multilayered laminate, for composite skin such as carbon fiber reinforced composites. Classical laminated plate theory detailed in Section 2.2, is used. As in most of the literature, Mindlin theory is assumed to be sufficient. In the following, all face properties are noted with the suffix f. For the simulations shown, the SDT [34] implementation of MITC4 composite plate/shell elements are used.

To simplify handling, the face sheets are normally meshed to be compatible with the underlying core models. In the case of detailed 3D models, one thus uses hexagonal shapes composed of two quadrangular elements, while in the SVS model regular rectangles are used.

The two FE models differ in the honeycomb core modeling. For the 3D detailed model, the core is formed of basis hexagonal cells which can be described by the geometric parameters shown in Figure 3.11. The double thickness walls, linked to the manufacturing process, where originally flat ribbons are assembled together to form the cells, is represented. The cell walls are considered as isotropic material. The nominal model considers one MITC4 element per cell wall although the validity of this assumption is discussed in section 3.4.4.

For the SVS model, an equivalent homogenized continuum replaced the honeycomb structure and the adhesive layer. The model is implemented with 8 nodes isoparametric HEXA8 elements composed with orthotropic material. HEXA8 element are linked to the MITC4 element of the face sheets by rigid link to simplify the proper handling of the distinction between surface (where the honeycomb connects to the skin) and neutral fiber (where the skin is meshed).

As detailed in Section 2.3, the SVS model has been the object of many studies. Table 3.1 lists parameters typically considered and which will be used as starting points for the estimation procedure of this chapter. As stated in Ref. [35], a value of $\nu^*_{xy} = 1$ gives a constitutive law that is not positive definite. This is clearly non-physical since a passive material cannot have deformation that produces energy, a value of 0.8 is thus used. The numerical values are calculated for the test case Aluminum/Nomex specimen (AN20), whose properties are given in Table 3.2.

Table 3.1: *Estimation of Honeycomb core properties [3] (with $t' = 2t$)*

In-plane (x,y) parameters			Out-of-plane parameters		
E^*_x	$E\left(\frac{t}{b}\right)^3 \frac{\frac{a}{b}+sin\theta}{cos^3\theta}$	0.148	E^*_z	$2E\frac{t}{b}\frac{\frac{a}{b}+1}{\left(\frac{a}{b}+sin\theta\right)cos\theta}$	256
E^*_y	$E\left(\frac{t}{b}\right)^3 \frac{cos\theta}{\left(\frac{a}{b}+sin\theta\right)sin^2\theta}$	0.148	G^*_{yz}	$G\frac{t}{b}\frac{cos\theta}{\frac{a}{b}+sin\theta}$	18.5
G^*_{xy}	$E\left(\frac{t}{b}\right)^3 \frac{\frac{a}{b}+sin\theta}{\left(2\frac{a}{b}\right)^2\left(\frac{1}{16}+\frac{a}{b}\right)cos\theta}$	0.0521	G^*_{xz}	Up: $G\frac{t}{b}\frac{\frac{a}{b}+sin^2\theta}{cos\theta\left(\frac{a}{b}+sin\theta\right)}$	30.8
				Low: $G\frac{t}{b}\frac{\left(2\frac{a}{b}+sin\theta\right)^2}{cos\theta\left(4\frac{a}{b}+1\right)\left(\frac{a}{b}+sin\theta\right)}$	30.8
ν^*_{xy}	$\frac{\left(\frac{a}{b}+sin\theta\right)sin\theta}{cos^2\theta}$	1*	ν^*_{zx}	ν	0.3
ν^*_{yx}	$\frac{cos^2\theta}{\left(\frac{a}{b}+sin\theta\right)sin\theta}$	1*	ν_{zy}	ν	0.3

Young's and shear moduli are given in MPa.
∗ theoretical value, 0.8 used to assure a positive definite constitutive law.

Modeling of a viscoelastic honeycomb panel equipped with piezoelectric patches in view of vibroacoustic active control design

3.2.2 Model parameterization and reduction

The approach that will be proposed to estimate effective parameters is an automated model update based on the match of periodic mode modal frequencies. This update requires computation of periodic modes for a large range of moduli. While, the cost of each evaluation is limited, the total time needed to evaluate multiple constitutive parameters can build up rapidly. This section outlines model reduction methodologies that have been used to speed up mode computations and were derived from Refs [36, 37, 38].

In the considered applications, one deals with variable constitutive parameters. The constitutive matrix $[\mathbf{\Lambda}]$, which represents the constitutive law underlying a FEM formulation can always be written as a linear combination of matrices

$$[\mathbf{\Lambda}(\alpha_\mathbf{i})] = \sum_i \alpha_i [\mathbf{\Lambda_i}], \qquad (3.1)$$

The definition of such matrices will be discussed in more detail in sections 3.2.3 and 3.2.4 for plates and orthotropic volumes. The assembled stiffness matrices of elements based on this constitutive law are always defined by an integration of the form

$$[\mathbf{K}(\mathbf{\Lambda}(\alpha_\mathbf{i}))] = \int_\Omega [\mathbf{\mathcal{B}}]^T [\mathbf{\Lambda}(\alpha_\mathbf{i})][\mathbf{\mathcal{B}}] d\Omega, \qquad (3.2)$$

with strain shape functions derivatives $[\mathbf{\mathcal{B}}]$ depending on the element type. It thus readily appears that the full finite element matrices follow the same linear combination as that of constitutive laws

$$[\mathbf{K}(\mathbf{\Lambda}(\alpha_\mathbf{i}))] = \sum_i \alpha_i [\mathbf{K}(\mathbf{\Lambda_i})]. \qquad (3.3)$$

If assembly time is an issue, one can assemble for each $[\mathbf{K}(\mathbf{\Lambda_i})]$, then recompute the model matrices by using the weighted sum. The main gain in computing time is however found using fixed basis reduction of parametric models [36, 37, 38]. This principle is to use a single Rayleigh Ritz basis $[\mathbf{T}]$ to approximate modes for a range of design points. The procedure outlined in Figure 3.5 assumes $\{\mathbf{q}\} = [\mathbf{T}]\{\mathbf{q_R}\}$ and solves for the reduced problem. It is important to note that the reduction is a linear combination. One can thus reduce matrices $[\mathbf{K}(\mathbf{\Lambda_i})]$ once and continue using the linear combination (3.3).
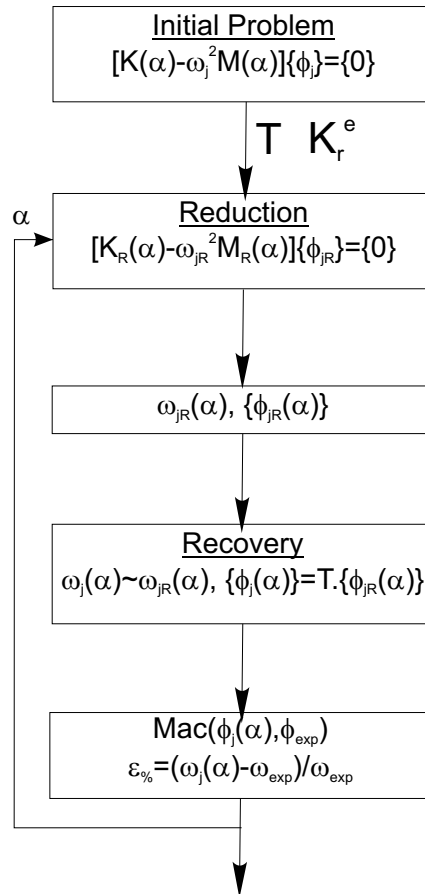
Figure 3.5: *Reduction and Correlation Process*

The multi-model reduction approach was used in this work. The underlying idea is that exact solutions are computed for a limited number of target points. In the present study extreme values of the α_i were used. The vector sets $\{\boldsymbol{\varphi}_{1:NM}(\alpha_i)\}$ found at the chosen design points are not necessarily independent, an orthonormalization step is thus performed to generate a basis $[\mathbf{T}]$. A detailed discussion of possible basis generation procedures can be found in [39]. Given the resulting Ritz basis, approximate solutions at other design points can then be computed within the subspace generated by the exact solutions.

3.2.3 Membrane and shear effects in plates

In this work, shell models are used to represent the skins and the glue. In both cases, it is useful to distinguish membrane and bending contributions as detailed below.

The classical plate formulation was given in Section 2.2.2. In particular, for isotropic symmetric plate, it was shown that the extension/bending coupling matrix $[\mathbf{B}]$ is a zero matrix. Hence the constitutive law is written

$$
\left\{ \begin{array}{c} \mathbf{N} \\ \mathbf{M} \\ \mathbf{Q} \end{array} \right\} = \left[\begin{array}{ccc} \mathbf{A} & \mathbf{B} & \mathbf{0} \\ \mathbf{B} & \mathbf{D} & \mathbf{0} \\ \mathbf{0} & \mathbf{0} & \mathbf{F} \end{array} \right] \left\{ \begin{array}{c} \boldsymbol{\varepsilon}^{\mathrm{m}} \\ \boldsymbol{\kappa} \\ \boldsymbol{\gamma} \end{array} \right\},
\tag{3.4}
$$

with

$$
[\mathbf{A}] = \frac{Eh}{1-\nu^2} \left[\begin{array}{ccc} 1 & \nu & 0 \\ & 1 & 0 \\ (s) & & \frac{1-\nu}{2} \end{array} \right] = Eh.[\mathbf{a}]
\tag{3.5}
$$

$$
[\mathbf{D}] = \frac{Eh^3}{12(1-\nu^2)} \left[\begin{array}{ccc} 1 & \nu & 0 \\ & 1 & 0 \\ (s) & & \frac{1-\nu}{2} \end{array} \right] = Eh^3.[\mathbf{d}]
\tag{3.6}
$$

$$
[\mathbf{F}] = \frac{Eh}{2(1+\nu)} \left[\begin{array}{cc} 1 & 0 \\ 0 & 1 \end{array} \right] = Eh.[\mathbf{f}]
\tag{3.7}
$$

These expressions clearly show that membrane and shear effects associated with $[\mathbf{A}]$ and $[\mathbf{F}]$ are proportional to Eh while bending effects associated with $[\mathbf{D}]$ are proportional to Eh^3.

Not all FEM codes allow a direct separation of constitutive law contributions in the building of the element. It is thus useful to realize that the decomposition can be achieved by combining multiple elements with realistic properties.

From two thicknesses, one can decompose membrane/shear and bending effects as

$$
[\mathbf{\Lambda}(\mathbf{E},\mathbf{h})] = Eh[\mathbf{\Lambda_1}] + Eh^3[\mathbf{\Lambda_2}]
\tag{3.8}
$$

where $[\mathbf{\Lambda_1}]$ and $[\mathbf{\Lambda_2}]$ are obtained with

$$
\left\{ \begin{array}{c} \mathbf{\Lambda_1} \\ \mathbf{\Lambda_2} \end{array} \right\} = \left[\begin{array}{cc} \frac{1.1^2}{E_0 h_0 (1.1^2 - 1)} & -\frac{1}{E_0 h_0 1.1 (1.1^2 - 1)} \\ -\frac{1}{E_0 h_0^3 (1.1^2 - 1)} & \frac{1}{E_0 h_0^3 1.1 (1.1^2 - 1)} \end{array} \right] \left\{ \begin{array}{c} \mathbf{\Lambda}(E_0, h_0) \\ \mathbf{\Lambda}(E_0, 1.1 h_0) \end{array} \right\}
\tag{3.9}
$$

It may also be interesting to represent the same overall properties as a combination of two plates that only differ in the membrane/shear and third plate that only differs from the first in its bending properties. One thus seeks to express the constitutive matrix as

$$[\mathbf{\Lambda}(\mathbf{E}, \mathbf{h})] = \frac{4Eh}{E_0 h_0}([\mathbf{\Lambda_{shell_2}}] - [\mathbf{\Lambda_{shell_1}}]) + \frac{4Eh^3}{E_0 h_0^3}([\mathbf{\Lambda_{shell_3}}] - [\mathbf{\Lambda_{shell_1}}]) \qquad (3.10)$$

Taking $shell_1$ ($E = E_0/4$, $h = h_0$, $\rho = \rho_0$), $shell_2$ ($E = E_0/\sqrt{2}$, $h = h_0/\sqrt{2}$, $\rho = 0$) and $shell_3$ ($E = E_0/(4\sqrt{2})$, $h = \sqrt{2}h_0$, $\rho = 0$) one has the following constitutive laws that verify the desired separation

$$[\mathbf{\Lambda_{shell_1}}] = \begin{bmatrix} \frac{E_0 h_0}{4}[\mathbf{a}] & 0 & 0 \\ 0 & \frac{E_0 h_0^3}{4}[\mathbf{d}] & 0 \\ 0 & 0 & \frac{E_0 h_0}{4}[\mathbf{f}] \end{bmatrix} \qquad (3.11)$$

$$[\mathbf{\Lambda_{shell_2}}] = \begin{bmatrix} \frac{2E_0 h_0}{4}[\mathbf{a}] & 0 & 0 \\ 0 & \frac{E_0 h_0^3}{4}[\mathbf{d}] & 0 \\ 0 & 0 & \frac{2E_0 h_0}{4}[\mathbf{f}] \end{bmatrix} \qquad (3.12)$$

$$[\mathbf{\Lambda_{shell_3}}] = \begin{bmatrix} \frac{E_0 h_0}{4}[\mathbf{a}] & 0 & 0 \\ 0 & \frac{2E_0 h_0^3}{4}[\mathbf{d}] & 0 \\ 0 & 0 & \frac{E_0 h_0}{4}[\mathbf{f}] \end{bmatrix} \qquad (3.13)$$

This expression does not however separate membrane and shear, but this was not deemed necessary in the present study. It is reminded that the same linear combination can be applied to the finite element matrices rather than the constitutive matrices. For the mass the decomposition, $\rho_{shell_1} = \rho_{shell}$ and $\rho_{shell_2} = \rho_{shell_3} = 0$ ensure that the sum of the mass is the same as the original mass. But if the implementation of element without mass was a problem, one can choose $\rho_{shell_1} = \frac{1}{3}\rho_{shell}$; $\rho_{shell_2} = \frac{\sqrt{2}}{3}\rho_{shell}$ and $\rho_{shell_3} = \frac{1}{3\sqrt{2}}\rho_{shell}$.

3.2.4 Parametric representation of orthotropic volume laws

For orthotropic materials, the constitutive law is given by

$$
\begin{Bmatrix} \sigma_x \\ \sigma_y \\ \sigma_z \\ \tau_{yz} \\ \tau_{xz} \\ \tau_{xy} \end{Bmatrix} =
\begin{bmatrix}
\frac{1-\nu_{yz}\nu_{zy}}{E_yE_z\Delta} & \frac{\nu_{yx}+\nu_{zx}\nu_{yz}}{E_yE_z\Delta} & \frac{\nu_{zx}+\nu_{yx}\nu_{zy}}{E_yE_z\Delta} & 0 & 0 & 0 \\
\frac{\nu_{yx}+\nu_{zx}\nu_{yz}}{E_yE_z\Delta} & \frac{1-\nu_{xz}\nu_{zx}}{E_xE_z\Delta} & \frac{\nu_{yz}+\nu_{yx}\nu_{xz}}{E_xE_y\Delta} & 0 & 0 & 0 \\
\frac{\nu_{zx}+\nu_{yx}\nu_{zy}}{E_yE_z\Delta} & \frac{\nu_{yz}+\nu_{yx}\nu_{xz}}{E_xE_y\Delta} & \frac{1-\nu_{xy}\nu_{yx}}{E_xE_y\Delta} & 0 & 0 & 0 \\
0 & 0 & 0 & G_{yz} & 0 & 0 \\
0 & 0 & 0 & 0 & G_{xz} & 0 \\
0 & 0 & 0 & 0 & 0 & G_{xy}
\end{bmatrix}
\begin{Bmatrix} \varepsilon_x \\ \varepsilon_y \\ \varepsilon_z \\ \gamma_{yz} \\ \gamma_{xz} \\ \gamma_{xy} \end{Bmatrix} \quad (3.14)
$$

with $\Delta = \frac{1-\nu_{xy}\nu_{yx}-\nu_{yz}\nu_{zy}-\nu_{zx}\nu_{xz}-2\nu_{yx}\nu_{zy}\nu_{xz}}{E_xE_yE_z}$.

For honeycomb applications, the key parameters are the out-of-plane shear moduli G_{xz} and G_{yz}. One thus seeks a decomposition that separates the contribution of these parameters from all the others

$$
[\mathbf{\Lambda}(G_{yz}, G_{xz})] = [\mathbf{\Lambda_0}] + G_{yz}\left[\mathbf{\Lambda_{G_{yz}}}\right] + G_{xz}[\mathbf{\Lambda_{G_{xz}}}] \quad (3.15)
$$

To avoid numerical problems in the implementation of elements, it is again found desirable to use realistic materials. One thus replicates the element 3 times with

$$
[\mathbf{\Lambda_{core1}}] = \begin{bmatrix} \left[\frac{\mathbf{C_1}}{3}\right] & [\mathbf{0}] \\ [\mathbf{0}] & \begin{matrix} \frac{G^0_{yz}}{4} & 0 & 0 \\ 0 & \frac{G^0_{xz}}{4} & 0 \\ 0 & 0 & \frac{G_{xy}}{3} \end{matrix} \end{bmatrix} \quad
[\mathbf{\Lambda_{core2}}] = \begin{bmatrix} \left[\frac{\mathbf{C_1}}{3}\right] & [\mathbf{0}] \\ [\mathbf{0}] & \begin{matrix} \frac{2\,G^0_{yz}}{4} & 0 & 0 \\ 0 & \frac{G^0_{xz}}{4} & 0 \\ 0 & 0 & \frac{G_{xy}}{3} \end{matrix} \end{bmatrix} \quad
[\mathbf{\Lambda_{core3}}] = \begin{bmatrix} \left[\frac{\mathbf{C_1}}{3}\right] & [\mathbf{0}] \\ [\mathbf{0}] & \begin{matrix} \frac{G^0_{yz}}{4} & 0 & 0 \\ 0 & \frac{2\,G^0_{xz}}{4} & 0 \\ 0 & 0 & \frac{G_{xy}}{3} \end{matrix} \end{bmatrix} \quad (3.16)
$$

so that $[\mathbf{\Lambda_{core0}}] = [\mathbf{\Lambda_{core1}}] + [\mathbf{\Lambda_{core2}}] + [\mathbf{\Lambda_{core3}}]$ corresponds to the core with the maximum stiffness. Hence, $[\mathbf{\Lambda_{core}}] = 3[\mathbf{\Lambda_{core_1}}] + \alpha_1([\mathbf{\Lambda_{core_2}}] - [\mathbf{\Lambda_{core_1}}]) + \alpha_2([\mathbf{\Lambda_{core_3}}] - [\mathbf{\Lambda_{core_1}}])$.
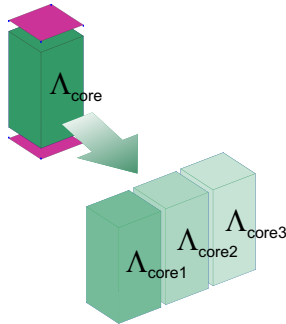
$$
[\mathbf{\Lambda_{core}}] = \begin{bmatrix} [\mathbf{C_1}] & [\mathbf{0}] \\ [\mathbf{0}] & \begin{matrix} \frac{(3+\alpha_1).G^0_{yz}}{4} & 0 & 0 \\ 0 & \frac{(3+\alpha_2).G^0_{xz}}{4} & 0 \\ 0 & 0 & G_{xy} \end{matrix} \end{bmatrix} \quad (3.17)
$$

Figure 3.6: *Decomposition of the core.*

By identification, one deduces $G_{yz} = (3 + \alpha_1) \frac{G_{yz}^0}{4}$ and $G_{xz} = (3 + \alpha_2) \frac{G_{xz}^0}{4}$ and the intermediate weighting coefficients are expressed by $\alpha_1 = 4 \frac{G_{yz}}{G_{yz}^0} - 3$ and $\alpha_2 = 4 \frac{G_{xz}}{G_{xz}^0} - 3$. It then appears that

$$
\begin{aligned}
[\mathbf{\Lambda}(G_{yz}, G_{xz})] &= (9\,[\mathbf{\Lambda_{core1}}] - 3\,[\mathbf{\Lambda_{core2}}] - 3\,[\mathbf{\Lambda_{core3}}]) \\
&\quad + G_{yz}\,\frac{4\,([\mathbf{\Lambda_{core2}}] - [\mathbf{\Lambda_{core1}}])}{G_{yz}^0} \\
&\quad + G_{xz}\,\frac{4\,([\mathbf{\Lambda_{core3}}] - [\mathbf{\Lambda_{core1}}])}{G_{xz}^0}
\end{aligned}
\tag{3.18}
$$

which gives the desired dependence (3.15).

It is then reminded that the same linear combination can be applied to the finite element stiffness matrices $[\mathbf{K_{core_1}}]$, $[\mathbf{K_{core_2}}]$ and $[\mathbf{K_{core_3}}]$ rather than the constitutive matrices. For the mass, the decomposition in $\rho_{core_1} = \rho_{core_2} = \rho_{core_3} = \rho_{core}/3$ is used although concentration of the mass on one element is possible.

3.3   Periodic wave computations

The method proposed to evaluate effective parameters of the core relies on multiple evaluations of periodic modes. A first approach was implemented using classical periodicity conditions. This is first introduced and allows discussion of pairing issues. Eventually, the cost of this approach was found to be too significant and computations of periodic modes based in Fourier/Floquet theory is thus introduced next.

3.3.1   Direct approach with a multiple cells

A first approach to computing periodic shapes is to mesh a model that has the length of the considered period, L_x along x-direction and L_y along y-direction, and to apply periodicity conditions on that mesh. The periodicity conditions on the normal modeshapes $\{\phi\}$ are

$$
\begin{aligned}
forall\, y : \{\phi(0,y)\} = \{\phi(L_x, y)\}, \\
forall\, x : \{\phi(x,0)\} = \{\phi(x, L_y)\}.
\end{aligned}
\tag{3.19}
$$

Periodic solutions always come in pairs at identical frequencies, corresponding the real and imaginary parts of the propagating wave. As illustrated in Figure 3.7, there is no reason for the modes computed in the 3D and SVS models to have a matching phase.

3D FEM   SVS FEM
4094.6 Hz 4179.0 Hz

3D FEM   SVS FEM
4094.9 Hz 4179.0 Hz
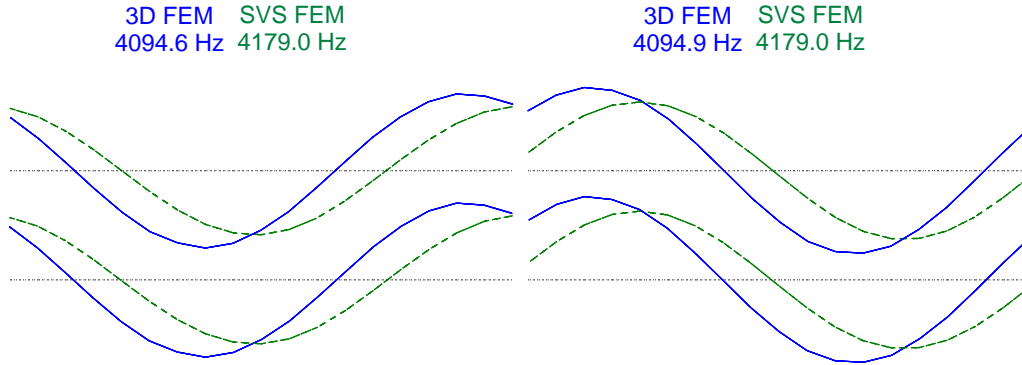
Figure 3.7: *Comparison of 3D FEM and SVS FEM periodic modes before preliminary updating*

Every orthogonal combination of the computed modes is however an acceptable modal basis. To ensure a good correlation, one thus combines pairs of eigenvectors to obtain, one vector with maximum amplitude at the left edge of the mesh and another to have zero amplitude. As illustrated in Figure 3.8, one thus seeks ψ such that

$$\begin{cases} \{\phi_{max}\} = cos(\psi).\{\phi_4\} + sin(\psi).\{\phi_5\} \\ \{\phi_0\} = -sin(\psi).\{\phi_4\} + cos(\psi).\{\phi_5\} \end{cases} \quad (3.20)$$

The procedure can be applied to both FE models. $\{\phi_0^{3D}\}$ and $\{\phi_0^{SVS}\}$, $\{\phi_{max}^{3D}\}$ and $\{\phi_{max}^{SVS}\}$ can thus be compared and the parameters updating performed.

zero value

ϕ_4 ϕ_0

maximum value

ϕ_5 ϕ_{max}
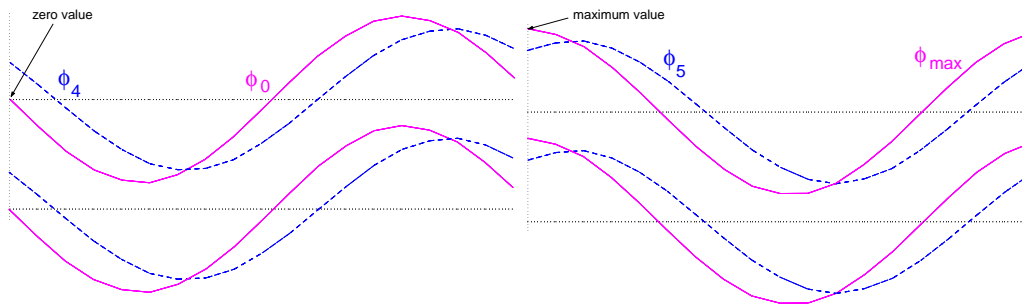
Figure 3.8: *Original eigenvectors compared to $\{\phi_0\}$ and $\{\phi_{max}\}$ eigenvectors*

To evaluate the validity of the effective parameters, it is important to check that they are independent of wavelength. Rather than computing the first mode of many meshes, it is tempting to use multiple modes of a longer volume. Indeed, the second periodic bending corresponds to the first periodic bending of a twice shorter beam. Figure 3.9 illustrates this correspondence of 100 mm and a 200 mm long beams.

Modeling of a viscoelastic honeycomb panel equipped with piezoelectric patches in view of vibroacoustic active control design
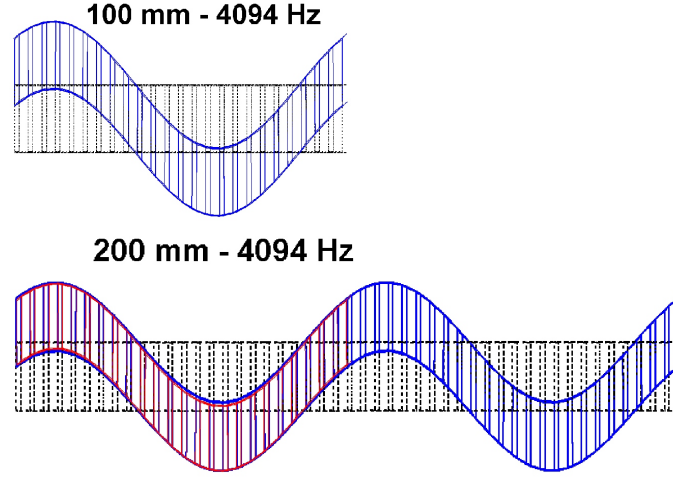
Figure 3.9: *Wavelength of periodic modes.*

Eventually, the computation of periodic modes for many wavelengths was found to be very costly. The next section will thus propose the use of Fourier/Floquet theory for the same objective.

3.3.2   Periodic modes by Fourier/Floquet theory

The objective of this section is to show how the periodic modes can be computed at a much lower cost using Fourier theory. The section summarizes equations detailed in [40] for the periodic structures and [41] for cyclic symmetry.

One considers a model whose properties are spatially periodic. For a physical response, known at regularly spaced positions $n\Delta x$, one can compute its Fourier transform

$$\{\mathbf{U}(\kappa)\} = \sum_{n=-\infty}^{+\infty} \{\mathbf{u}(n\Delta x)\} e^{-j\kappa n\Delta x} \tag{3.21}$$

$\{\mathbf{U}(\kappa)\}$ is a complex shape defined on the mesh of the repeated cell. One actually uses two cells to represent the real and imaginary parts of $\{\mathbf{U}\}$. The wave number κ varies in the $[0, \frac{2\pi}{\Delta x}]$ interval (or any interval of the same length, since $\{\mathbf{U}(\kappa)\}$ is periodic in the wavelength domain).

Given the Fourier transform $\{\mathbf{U}(\kappa)\}$, one can recover the physical motion by computing the inverse Fourier transform

$$\{\mathbf{u}(n\Delta x)\} = \frac{\Delta x}{2\pi} \int_0^{\frac{2\pi}{\delta x}} \{\mathbf{U}(\kappa)\} e^{j\kappa n\Delta x} d\kappa \tag{3.22}$$

For a mono-harmonic response (fixed wave number κ), the spatial transform is given by $\{\mathbf{u}(n\Delta x)\} = \mathrm{Re}\left(\{\mathbf{U}(\kappa)\} e^{jn(\kappa\Delta x)}\right)$. This property can be used to recover motion on

any cell based on known values on the first one. As the motion is continuous between geometric cells, one has $\{\mathbf{u_{left}}(n\Delta x)\} = \{\mathbf{u_{right}}((n-1)\Delta x)\}$. In a FEM model, displacements are known at a number of DOFs assembled in a vector $\{\mathbf{U}\}$. For a given cell, one defines observation matrices $[\mathbf{c_L}]$, $[\mathbf{c_R}]$ to extract corresponding displacements on the left and right edges. The continuity condition on all interface DOFs can thus be written in the form $[\mathbf{c_L}]\{\mathbf{U}(\kappa)\} = [\mathbf{c_R}]\{\mathbf{U}(\kappa)\}e^{-j(\kappa\Delta x)}$. Hence, in the real/imaginary format, one has the constraint equation on nodes of the cell edge

$$
\left[\begin{array}{cc} [\mathbf{c_L}] - \cos(\kappa\Delta x)[\mathbf{c_R}] & -\sin(\kappa\Delta x)[\mathbf{c_R}] \\ \sin(\kappa\Delta x)[\mathbf{c_R}] & [\mathbf{c_L}] - \cos(\kappa\Delta x)[\mathbf{c_R}] \end{array} \right]_{2N_r \times 2N} \left\{ \begin{array}{c} Re(\mathbf{U}) \\ Im(\mathbf{U}) \end{array} \right\} = 0 \qquad (3.23)
$$

Periodic modes are mono-harmonic solutions of wavelength π/κ. One thus seeks to solve for

$$
\left[\begin{array}{cc} \mathbf{K} - \omega_j^2\mathbf{M} & 0 \\ 0 & \mathbf{K} - \omega_j^2\mathbf{M} \end{array} \right] \left\{ \begin{array}{c} Re(\mathbf{U}) \\ Im(\mathbf{U}) \end{array} \right\} = 0 \qquad (3.24)
$$

with (3.23) verified.

Figure 3.10 illustrates the basic cell and restitution on multiple cells using (3.22) of modes computed to $1/\kappa$ equal to 3 and 17.
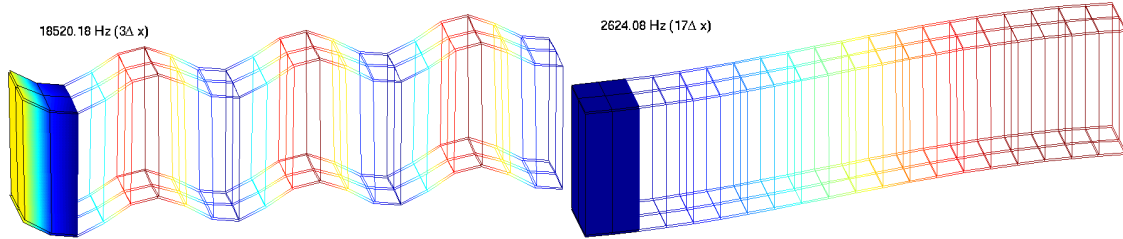
Figure 3.10: *Periodic modes of the SVS model*

One can usefully note that the wavelength $L = \pi/\kappa$ covers the full interval of positive lengths, that $\{\mathbf{u}(\frac{2\pi}{\Delta x} - \kappa)\} = \{\bar{\mathbf{U}}(\kappa)\}$, and thus that the half spectrum corresponds to a wavelength of Δx. Using the property of symmetry allows the use of computations for wavelengths larger than Δx only. For forced responses, one solves for $\{\mathbf{U}(\kappa)\}$ at multiple κ knowing the transform of the applied loads, then uses a numerical approximation of (3.22) to recover the physical response at any desired position.

The major advantage of using periodic modes is that only two cells need to be meshed for computations at any wavelength. Compared to the simple periodicity condition with multiple cells, it is thus much easier to compute modes for large wavelengths (low frequencies). This method was thus preferred when it became available in SDT [34]. The issue of matching modes discussed in section 3.3.1 remains and is treated similarly.

3.4   Panel constituent properties and their influence

In this section one seeks to analyze the energy contributions of various constituents of a honeycomb sandwich panel as a function of wavelength/frequency and glue properties. A specific study of the 3D FE model and the comparison with the SVS FE model alow to infer on the limits of the homogeneization.

To illustrate the procedure, a particular panel is chosen and its properties are given in Section 3.4.1. Section 3.4.2 then analyses energy contributions in the core, skins and glue layers. Section 3.4.3 further details the influence of glue. Finally local effects in the honeycomb cell walls are detailed in Section 3.4.4.

3.4.1   Test case properties

The honeycomb sandwich specimen chosen is an Aluminum/Nomex honeycomb, available at ONERA and designated by AN20, whose properties are given in Table 3.2 and Figure 3.11. It corresponds to the sample whose test is described in Chapter 4. One refers to AN20L for beams cut along longitudinal direction and to AN20W along transverse (or width) direction.

Table 3.2: *Definition of AN20 Aluminum-Nomex test beam parameters*

	Geometric parameters		Material parameters	
Face sheet	h_f	0.6 mm	ρ_f	$2.8 \ 10^3 kg/m^3$
(Aluminum)			E_f	72.5 GPa
Honeycomb core	h_h	20 mm	ρ_h	$1.38 \ 10^3 \ kg/m^3$
(Nomex)	t (t'=2.t)	$7.62 \ 10^{-2}$ mm ($1.524 \ 10^{-1}$ mm)	$E_{h_{ref}}$	3 GPa
	a, b, θ	2.75 mm, 2.75 mm, π/6 rad		
Glue	$h_g = h_f/2$	0.3 mm	ρ_g	$10^3 \ kg/m^3$
(Hypothesis: epoxy)	$t_{g_{ref}}$	0.1 mm	$E_{g_{ref}}$	2 GPa

The main advantage of this specimen is that face sheets properties are well known. The cells are made of Nomex paper which is composed of short aramid fiber and phenolic resin. The characteristics of this material are not well known. They can however be assumed to be invariant by rotation within the paper plane. It thus seems acceptable to consider the cell wall as a plate composed of isotropic material. This assumption is by no means demonstrated and shows the difficulty in building a honeycomb model from constituent properties.
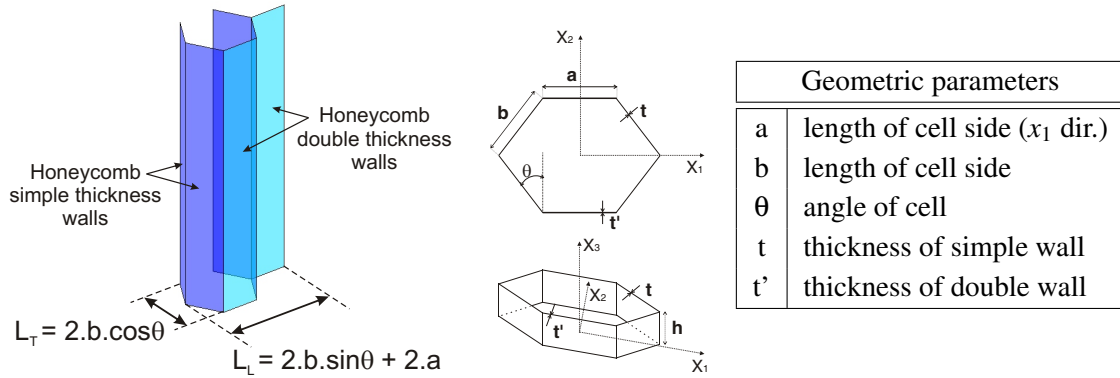
Figure 3.11: *Definition of honeycomb core geometric parameters*

The glue properties are completely unknown and a discussion will be done in Section 3.4.3. Densities are those found in literature for such materials and have not been verified. The influence of the core density will be discussed in Section 3.5.1.

3.4.2   Dominant constituents and wavelength

The objective of this section is the evaluation of energy contributions in honeycomb panels as a function of wavelength/frequency. For plates, one is interested in separating the membrane and bending contributions. For orthotropic representations of the core, one wants a separate evaluation of the energy associated with the *xz* and *yz* transverse shears, which dominate, and a verification that the remaining energy is negligible.

Periodic modes (propagating waves) are typically mass normalized when evaluated. In the present case, one wants to compare the contributions of constituents at multiple frequencies. One thus normalizes the strain energy, which is equivalent to compute the energy fraction in each constituent. Based on the parametric decompositions (3.8) for isotropic plates and (3.15) for orthotropic volumes one obtains stiffness matrices associated with specific terms in the constitutive law and computes energy fractions from

$$E(\boldsymbol{\phi}) = \sum_I \frac{1}{2} \alpha_i \{\boldsymbol{\phi}\}^T [\mathbf{K}(\boldsymbol{\Lambda_i})] \{\boldsymbol{\phi}\}, \tag{3.25}$$

with $\{\boldsymbol{\phi}\}$ the mode shape vector at the considered wavelength. One notes that the considered decompositions of the constitutive matrices are sums of positive definite matrices, so that the linear combination is really a sum of energies.

For the 3D FE model, face sheets, glue and honeycomb cells are modeled by isotropic plates. The strain energy relative to the face sheets and to the glue is separated into *A* terms, that refer to membrane/shear effects, and *D* to bending. As detailed in the discussion of the constitutive law parameterization done in Section 3.2.3, *A* terms depend linearly on product $E_f.h_f$ for the skins and $E_g.t_g$ for the glue and *D* terms on $E_f.h_f^3$ and

$E_g.t_g^3$. Concerning plate representations of the honeycomb core, the distinction between membrane/shear effects and bending does not seem relevant here, since it is not directly related to the effective parameters $G_{xz}^\star$ and $G_{yz}^\star$. The linear dependence to the cell wall Young modulus E_{nomex} will be the only one retained.

For the nominal panel (AN20), Figure 3.12 displays for the detailed 3D model the evolution of the periodic mode frequency as a function of wavelength and the associated energy contributions. The wavelength is scaled to the length of the unit cell L_{cell}, with $L_{cell} = L_L$ for beam along x-direction and $L_{cell} = L_T$ for beam along y-direction, defined on Figure 3.11. The plot clearly indicates very different regimes. Above 1000 cell lengths (at low frequencies), the energy is essentially due to membrane effects in the skin. This is underlying principle of honeycombs, the core only serves to separate the skins which carry all the load.

Between 3 and 100 cell lengths, the core contains a major part of the energy. Its properties are thus critical to properly represent motion with relatively short wavelengths. For isolated panels, such motion only occurs at higher frequencies. When integrated into frames, structural effects may lead to short wavelength behavior at low frequencies.
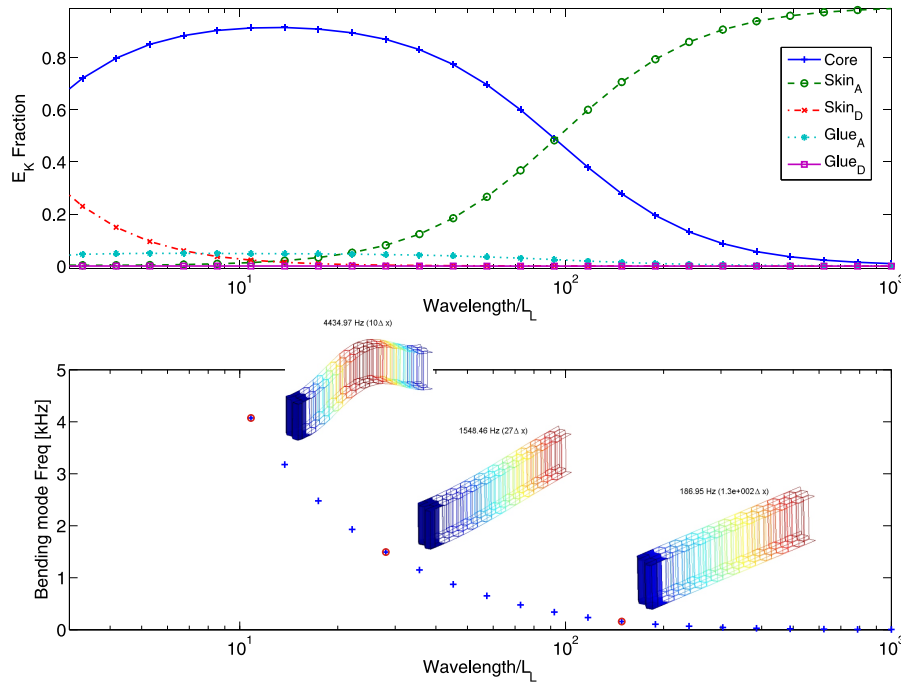
Figure 3.12: *Top: Energy contribution of constituents, detailed 3D model, bending along x-direction. Bottom: Frequency of first periodic mode along x-direction. Examples of mode shapes*

For very short wavelengths, very high frequencies, one starts seeing local modes of the skin and/or honeycomb (see Figure 3.21). Such modes are not really of interest to the present study which focuses on low frequency panel behavior.

One interest of the parametric study on the 3D detailed model is the ability to estimate quantitatively the influence of the bonding. Very few results on its influence have been found in literature. One can mainly mention Burton and Noor [42] who have studied the effect of the adhesive joint between the face sheet and the honeycomb core on the static response of sandwich panels. A 3D detailed FE model which represents in details the adhesive layer has been implemented with ANSYS code. The authors have shown that the ratio of the strain energy in the adhesive joint to the total strain energy could reach 11% for titanium alloy honeycomb sandwich with high-modulus composite for face sheets. For the considered specimen (AN20), the shear energy in the glue is above 8 % in the 10 to 50 cell lengths range (4kHz to 700Hz). This confirms the findings of Burton and Noor, and justifies the need for a specific study of the glue presented in the next section.

Figure 3.13 shows a similar plot for the SVS model with separation of strain energy in the skin, core transverse shear moduli $G_{xz}^\star$ and $G_{yz}^\star$ and other energy in the core. Similar regimes are found and one verifies the classical result that almost all the energy in the core is associated with the $G_{xz}^\star$ shear, for bending along x-direction.
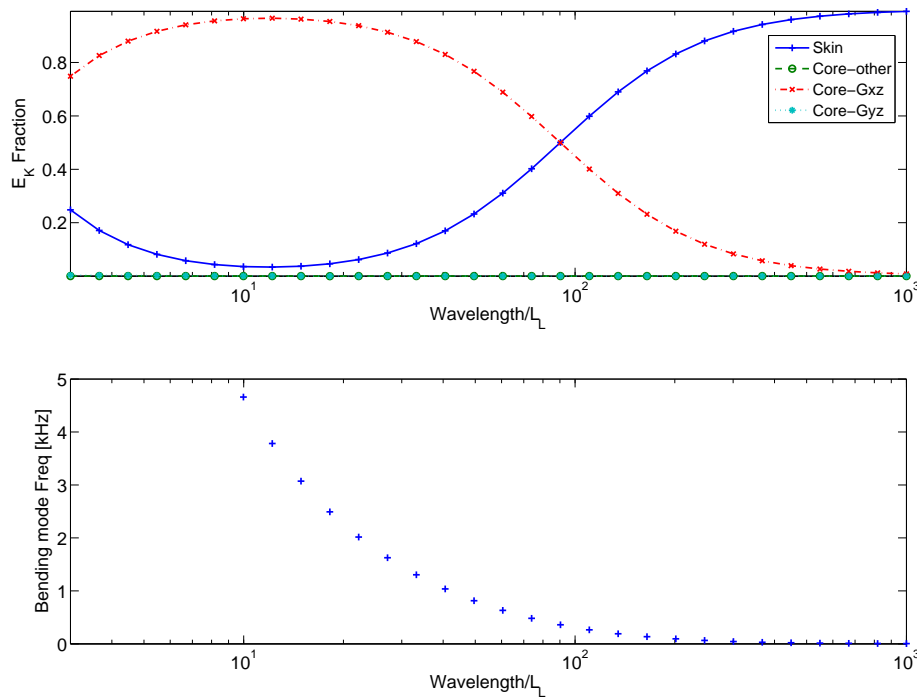
Figure 3.13: *Top: Energy contribution of constituents, SVS model, bending along x-direction. Bottom: Frequency of first periodic mode along x-direction*

The parametric study on the detailed 3D model highlights the influence of the adhesive layer on the dynamic behavior of the honeycomb sandwich beam, while the study on the SVS model illustrates the classical result on dynamics of sandwich composite, the main influent parameters are the face sheets Young modulus and the core shear moduli.

3.4.3   Influence of glue parameters

The detailed 3D model is used in this section, the skin and Nomex paper properties are assumed be known properly and one seeks to understand under which conditions the glue influences the dynamic properties significantly.

Figure 3.14 illustrates the evolution of energy fractions in the glue layer for varying glue moduli. By means of parametric study on the detailed 3D honeycomb, one readily concludes that the strain energy in the adhesive joint decreases with the increase of the glue modulus like found in ref [42]. Since 0.2 GPa is a very realistic value for epoxy it clearly appears that the glue can indeed have a major impact on the short and medium wavelength dynamics. One will now seek to evaluate the possible impact on the 900 mm long AN20L sandwich beam.
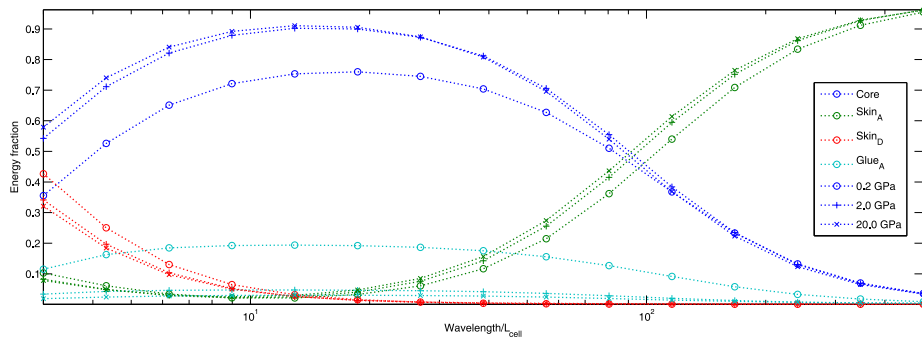
Figure 3.14: *Energy fraction of constituents. Detailed 3D model with 0.2 to 20 GPa glue modulus*

In practice, the exact geometry of the glue volume is not known and shows significant irregularities. The representation of the adhesive fillet is presented in Section 3.2.1, in particular Figure 3.3 compares the observed fillet with the model chosen. It was thus chosen here to use glue shear and bending stiffness as parameters characterizing the glue, that depend not only on E_g but also on the glue element thickness t_g. The reference deformations used to define these quantities are shown in Figure 3.15.

Figure 3.15: *Parameterization and stress on glue element*

Modeling of a viscoelastic honeycomb panel equipped with piezoelectric patches in view of vibroacoustic active control design

The considered model represents glue fillets as shell elements, parameters effectively entered in the FE code are thus E_g and t_g. For a clamped beam and a rigid top surface shown in Figure 3.15, one can compute a bending moment $M_b = K_{bend}\theta$ and a shear force $F_s = K_{shear}x$ and thus relate E_g and t_g to equivalent stiffness parameters

$$K_{bend} = \frac{E_g a t_g^3}{12 h_g},$$

(3.26)

$$K_{shear} = \frac{E_g a^3 t_g}{4 h_g^3}.$$

(3.27)

As the geometry of the real glue volume is not regular (see Figure 3.3), only plausible limits of stiffness can be given. K_{bend} and K_{shear} ranges are evaluated by surrounding the real glue volume by parallelepipedic element. A typical value of glue Young's modulus is E_g= 2 GPa. According to manufacturers data, epoxy adhesive Young's modulus E_g is within range

$$E_{g_{min}} = 20 MPa,$$
$$E_{g_{max}} = 5 GPa.$$

(3.28)

The glue thickness must be higher than the honeycomb cell wall thickness $t = 0.762\mu m$ (see Figure 3.11) for the AN20L test beam. Concerning $t_{g_{max}}$, it is chosen by observing glue joint by electron microscopy (see Figure 3.3). The thickness of the skin is 0.6 mm, it is assumed to be a reasonable value for the upper bound of glue volume thickness.

The height h_g of the glue volume is lower than laminate thickness, 0.6 mm and higher than 0.2 mm. With this approximate data, a realistic stiffness range of the glue is found (Figure 3.16),

$$K_{shear} \in \left[9.89.10^5,\ 7.21.10^7\right] N/m$$
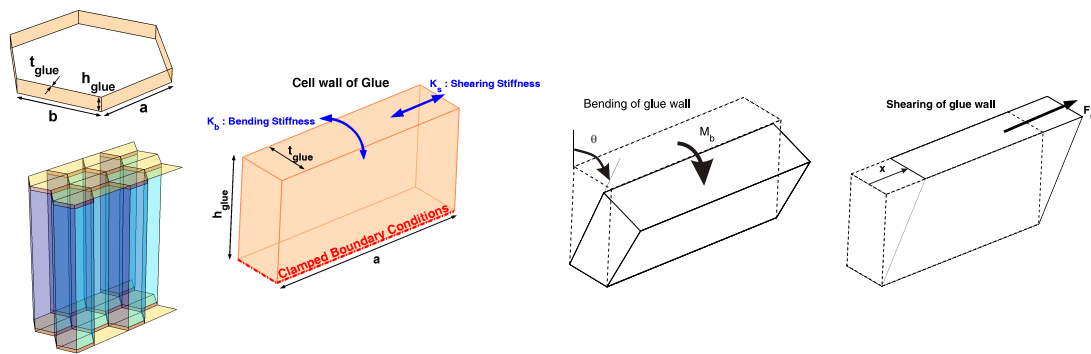$$K_{bend} \in \left[1.01.10^{-5}, 4.12.10^{-1}\right] N.m/rad.$$

(3.29)

The chosen meshing procedure represents glue as a shell with h_g equal to the skin half-thickness (0.3 mm), and a as the length of the honeycomb cell side. One thus has a direct relation between (K_{shear}, K_{bend}) and (t_g, E_g) based on equations (3.26) and (3.27). Assuming E_g= 2 GPa and $t_g = 0.1$mm, leads to K_{bend}/K_{shear} values in the middle of the acceptable area ($K_{shear} = 3.84.10^7$ N/m and $K_{bend} = 1.53.10^{-3}$ N.m/rad).

The reasonable areas for K_{bend}, K_{shear} and E_g, t_g are plotted on Figure 3.16, respectively in white and blue. The influence on the first mode frequency of the 900 mm AN20L beam is shown in the figure and in Table 3.3. The effect is clearly significant, specially for shear, and underlines the need for proper estimation of glue properties. One should also note that Figure 3.14 showed that the importance of glue increases with frequency.
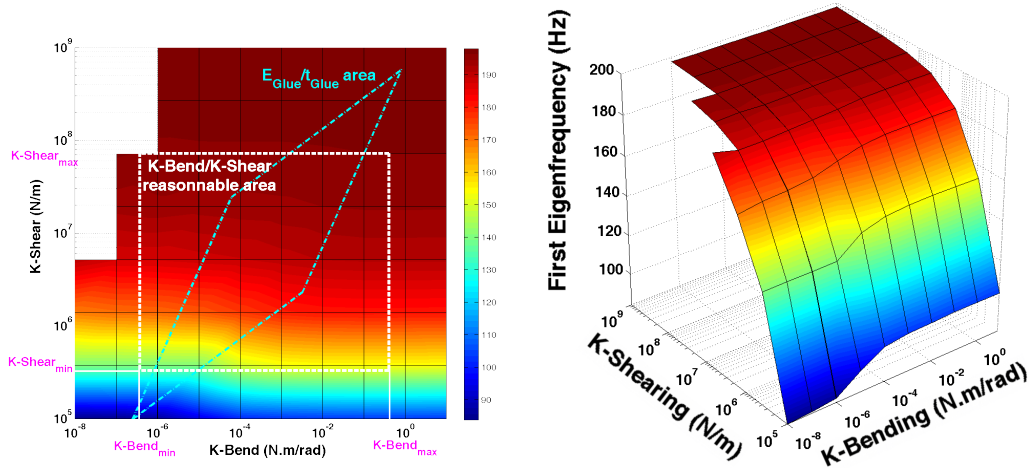
Figure 3.16: *Potential glue stiffness parameters K_{Bend} and K_{Shear} and their influence on the first mode frequency in free-free conditions*

Table 3.3: *Influence of K_{Bend} and K_{Shear} on the first eigenfrequency of AN20L 900mm beam in free-free conditions*

K_{Shear}	$K_{Bend}(N.m/rad)$									
(N/m)	10^{-8}	10^{-7}	10^{-6}	10^{-5}	10^{-4}	10^{-3}	10^{-2}	10^{-1}	1	10
10^5	83.87	84.47	85.9	94.35	101.4	102.9	103.5	103.7	103.7	103.4
$3.7\ 10^5$	140.2	140.2	140.4	140.5	149.8	153.1	154.0	154.1	154.1	153.8
$1.4\ 10^6$	169	170.7	171.4	173.1	176.6	179.7	180.9	181.1	181.1	180.9
$5.2\ 10^6$	190.5	187.6	187.6	188.4	189.0	190.1	191.0	191.3	191.3	191.3
$1.9\ 10^7$		193.5	194.1	193.5	193.9	194.1	194.5	194.7	194.7	194.7
$7.2\ 10^7$		196.5	195.9	196	196.0	196.0	196.1	196.2	196.3	196.3
$2.7\ 10^8$			197.1	197.1	197.1	197.1	197.1	197.2	197.3	197.3
$1\ 10^9$			198.0	197.8	197.7	197.7	197.7	197.8	198.0	198.0
	Frequency (Hz)									

3.4.4   Local effects of honeycomb cell wall

The next limitation of the equivalent SVS model is its inability to model local dynamics within the honeycomb volume. While such dynamics are not desirable, understanding their occurrence was deemed to be necessary to understand the frequency range of validity for the considered models.

The local effect of honeycomb cell has been simulated for the AN20 test case, with fixed skins and fixed edge cells. The meshing of the wall is refined to simulate the local

bending of cells. Figure 3.17 illustrates the various regimes that can be found for variable glue stiffness.
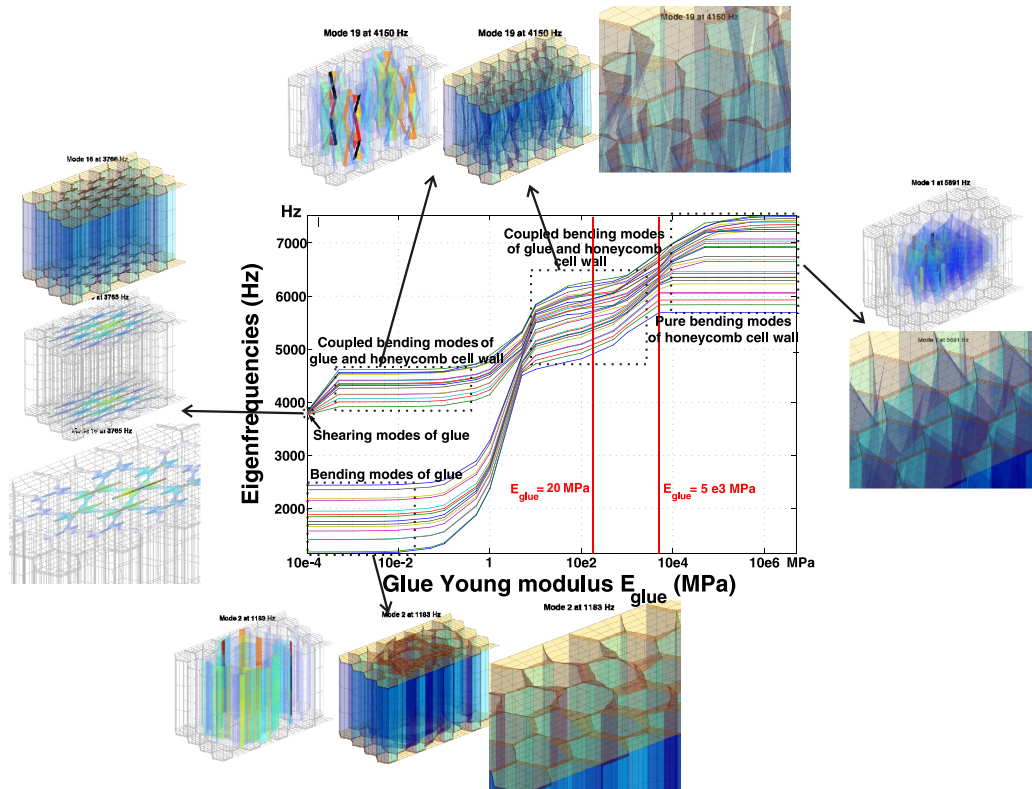
Figure 3.17: *Local modes as a function of E_g*

For very low, probably unrealistic, E_g, one has glue bending and shear modes. For higher modulus, bending modes of the honeycomb cell wall are coupled with glue deformation and occur above 4 kHz. For a stiff glue ($E_g = 2 GPa$), modes are nearly pure honeycomb cell wall bending and occur around 6kHz.

Those frequencies are above active control frequency band considered. However, that depends on basic material for honeycomb, here Nomex, on kind of glue and on honeycomb geometry and thickness. For each panel designed for active control one should verify that local mode frequencies are out of active control frequency band.

For the determination of effective parameters in the next section, low wavelength periodic modes will be shown to depend significantly on dynamic deformation in the core so that the equivalence between 3D and SVS model is not maintained in that frequency range.

3.5 Effective core parameters of an aluminum/nomex composite

As outlined in the introduction, the SVS model is needed for large scale simulations, but relies on the estimation of effective core shear moduli $G^\star_{xz}$ and $G^\star_{yz}$ which are not direct material parameters. This section thus discusses a numerical procedure to estimate $G^\star_{xz}$, respectively $G^\star_{yz}$. The estimation is based on an automated parameter updating, matching the frequencies of periodic modes of the 3D and SVS models at multiple wavelengths.

Section 3.5.1 illustrates the procedure for the AN20 Aluminum/Nomex specimen and highlights the importance of wavelength regimes that were described in Section 3.4.2. Section 3.5.2 validates the parameters obtained for computations on a full panel. Section 3.5.3 addresses the question, often mentioned in the literature, of whether or not effective parameters are dependent on skin properties. Finally, Section 3.5.4 discusses a procedure to separate honeycomb and glue properties that would use multiple tests.

3.5.1 Effective core parameters identified by inverse problem

As illustrated in Section 3.4.2, periodic modes propagating in the *x*-direction have almost their energy distributed between the skin and the shear energy associated with the $G^\star_{xz}$ term of the constitutive matrix. Assuming that the skin properties are well known, one can thus perform a single parameter update of $G^\star_{xz}$ in the SVS model to match the frequency of the corresponding mode in the detailed 3D model. This section illustrates the process and its limitations.

To avoid problems with skin properties, one uses the same skin models for both the 3D and SVS model (shown in Figure 3.18). The periodic modes computed for SVS and 3D FE models are computed for variable wavelengths. *y* symmetry is assumed to avoid in-plane shear modes. Simple periodicity in the *y*-direction is assumed to focus on periodic bending modes in the *x*-direction. At low wavelength/high frequency, cell wall bending occurs and this effect will be discussed in more detail.
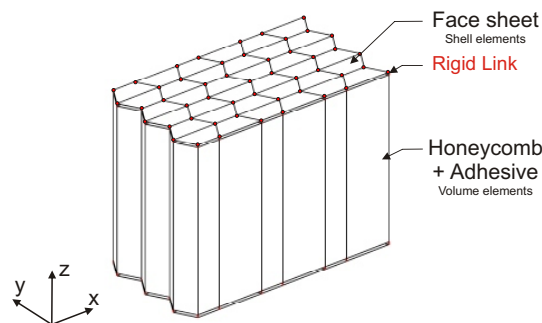

Figure 3.18: *SVS model with skin geometry of the 3D model*

Figure 3.19 illustrates the results of the proposed homogeneization procedure.

The top graph shows the frequency error on the first bending mode for multiple values of $G_{xz}^{\star}$. The bottom graph shows the evolution of the $G_{xz}^{\star}$ value for which the frequency error is null. The mean value of 26.94 MPa is valid for a fairly large wavelength range but one has divergence at both extremities. The high wavelength / low frequency divergence was never explained properly.

Figure 3.19: *Top: error on the first periodic bending mode frequency for various values of $G_{xz}^{\star}$. Bottom: Estimation of $G_{xz}^{\star}$ associated with no error. Detailed 3D model with 3 by 3 refinement (curves correspond to +0.8% to 0% mass)*

Figure 3.13 showed that the core has very limited strain energy and thus significant (diverging) modulus changes are needed to compensate for small frequency errors. For the nominal honeycomb of the study (AN20), beyond 100 cell lengths, i.e. below 250 Hz, the value of the shear modulus has too little influence on the bending energy to be estimated by this procedure. After many sensitivity studies, including the switch to identical skin models, it was found that only a mass correction would lead to a constant estimate of the shear modulus. The figure shows that an arbitrary increase of the core mass by a little more than 0.5% leads to nearly constant modulus. Figure 3.20 shows that a less refined model requires a similar although slightly smaller correction.

While the inertia representation by a homogeneous density does seem a proper approximation of the 3D inertia, the correction needed is extremely small and a second order effect in the inertia representation is plausible. In practice, honeycomb bonding procedure clearly induces uncertainties in the mass much larger than 0.5%.
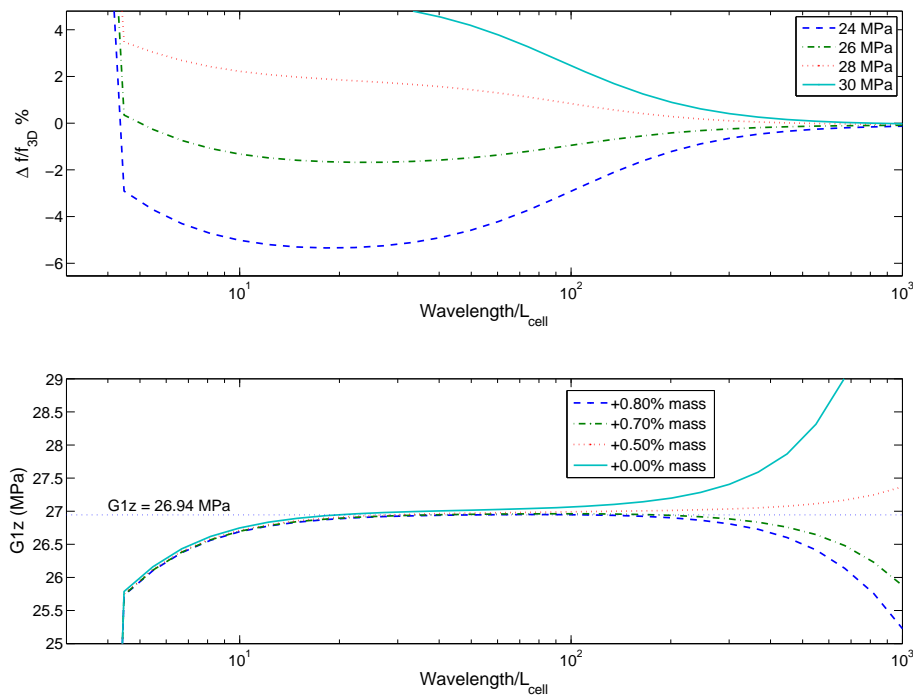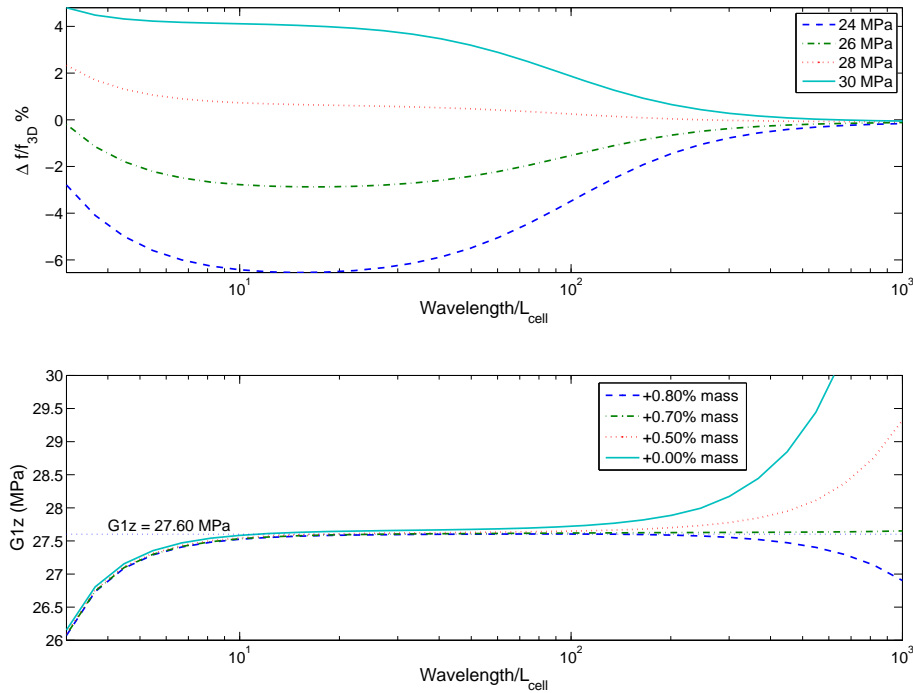
Figure 3.20: *Top: error on the first periodic bending mode frequency for various values of $G_{xz}^{\star}$. Bottom: Estimation of $G_{xz}^{\star}$ associated with no error. Detailed 3D model with 1 element per cell wall*

A second divergence is always for low wavelength, in the present case below 5 cell lengths. At low wavelength, cell wall bending first adds to the beam bending, see Figure 3.21 (left), then the cell wall bending mode becomes the first periodic mode that occurs (here near 10 kHz as shown in Figure 3.21 right). What explains the sharp divergence in case of 3 by 3 refinement of the cell walls. When using a 3D FE model with only one element per cell wall, see Figure 3.20, the full divergence disappears but one really cannot rely on the estimated modulus values below 10 cell lengths.

The presence of the divergences motivates the need for experiments evaluating the transverse shear for waves certain wavelength ranges. In the present case, the 30 to 200 cells length range (1500 Hz to 100 Hz), seems sufficiently sensitive to core properties and independent local bending effects. Curves of $G_{xz}^{\star}$ as function of wavelengths, estimated for 3D FE model with 1 and 3 elements per cell wall, have been superposed on Figure 3.22. Besides the divergence below 5 cell lengths, already mentioned, one observes that the mean value of effective $G_{xz}^{\star}$ obtained with the numerical procedure, for the 10 to 100 cells length range, only differ by 2.45%. To understand the origin of this difference, Figure 3.23 shows the relative error on the frequencies computed for the SVS FE model with refinement from 1 element (shown in Figure 3.18) to a division by 5 elements, taken as reference. As expected, for small wavelengths, ie high frequencies, the
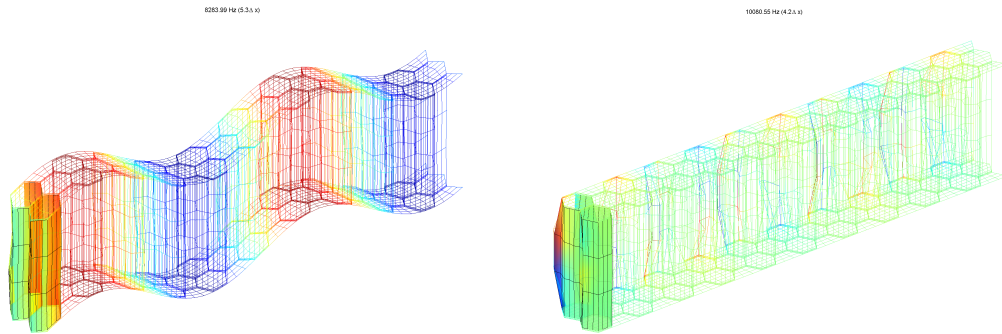
Figure 3.21: *Mode shape for wavelengths 5.3 cell lengths (left) and 4.2 cell lengths (right). Local cell wall bending occurrence*

refinement is influent because the exact deformation in the core is not linear and can only be reproduced with multiple elements. For wavelengths above 30 cell lengths the error is very small and cannot explain differing estimated moduli. The difference in this estimate is thus associated with the convergence of the 3D model.
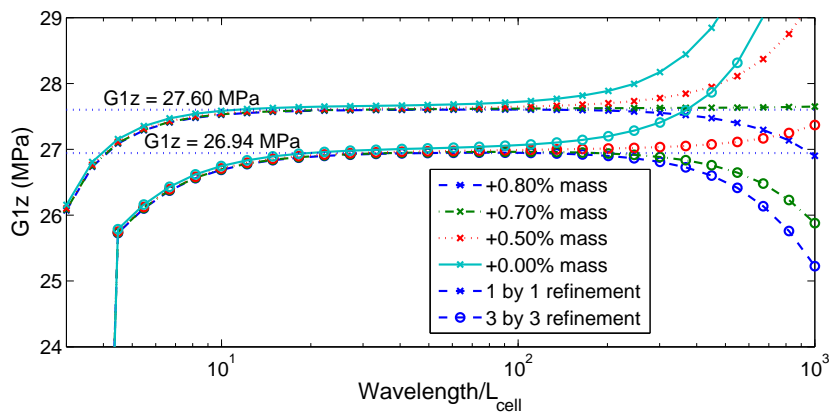
Figure 3.22: *Superposed estimations of $G_{xz}^{\star}$ associated with no error for detailed 3D model with 1 element and 3 elements par cell wall*
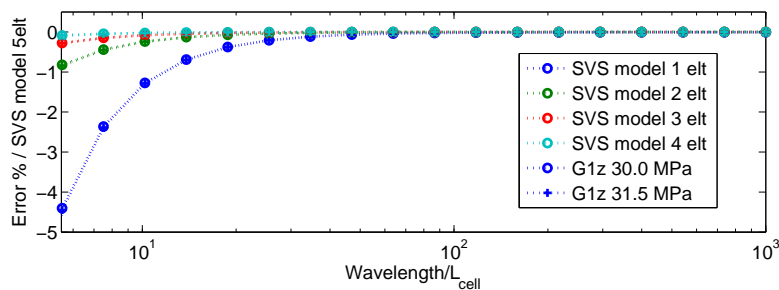
Figure 3.23: *Frequency error on the first periodic bending mode for refinement of 1 to 5 elements compared to the refinement of 5 elements - SVS FE model*

The updating of the shear modulus in transverse direction $G_{yz}^{\star}$ gives very similar results. The energy fractions show the same transition between skin and $G_{yz}^{\star}$ contributions. With an adaptation of the core mass, the modulus is constant at 17.82 MPa for all but very short wavelengths. As for the x-direction, the estimation of $G_{yz}^{\star}$ with refinement of 1 element per cell wall (Figure 3.24) presents a slightly different result from the estimation with refinement of 3 elements per cell wall, with only 0.45% difference.
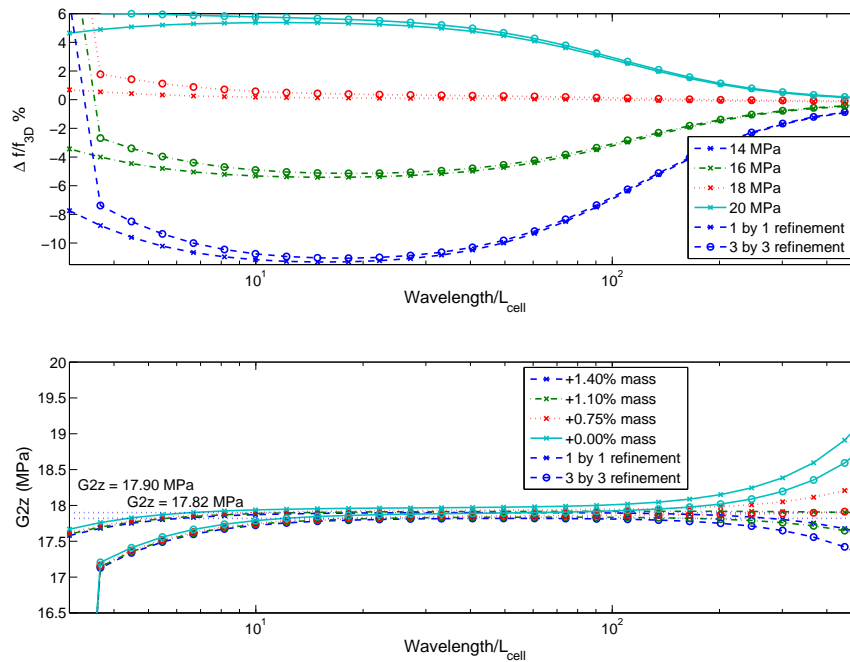
Figure 3.24: *Top: error on frequency of the first periodic bending mode for various values of $G_{yz}^{\star}$. Bottom: Estimation of $G_{yz}^{\star}$ associated with no error. Superposition for 3 elements and 1 element per cell*

To conclude the section, it is useful to remind that the motivation for the SVS model is to dissociate honeycomb cell and mesh geometry. Confirming that effective parameters estimated for a particular configuration can be reused with other meshes is thus important. Figure 3.25 illustrates the error on periodic wave frequency for elements of various sizes. The error is only significant for low wavelengths. But then skin bending plays a significant role there, so that using large elements are expected to induce errors (a 3 cells element for a 4 cells period is really coarse indeed).
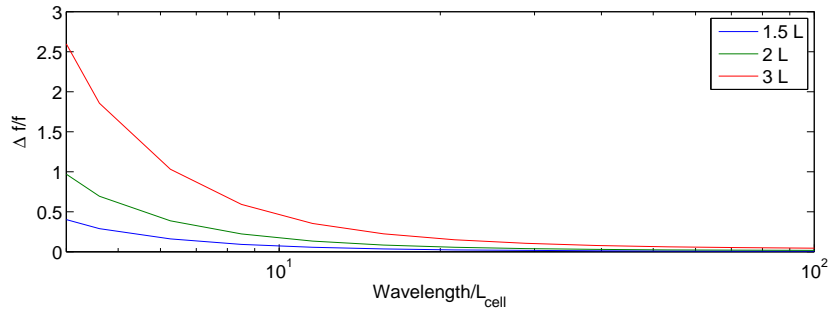
Figure 3.25: *Relative error (in %) on the frequency of the periodic bending mode for variable SVS element sizes*

Finally, Table 3.4 summarizes the formulations found in literature review for effective shear moduli $G^\star_{xz}$ and $G^\star_{yz}$. The numerical values are given for the AN20 Aluminum/Nomex specimen. The shear moduli found through numerical estimation are slightly lower than formulas of the literature, but it is not surprising since the glue, which is softer than Nomex, is taken into account in the proposed procedure.

Table 3.4: *Comparison of quoted estimation of $G^\star_{xz}$ and $G^\star_{yz}$*

| Author	Hyp.	$G^\star_{xz}$		$G^\star_{yz}$	
		formula	AN20	formula	AN20
Kelsey [11]	t'=2t	Up: $G\frac{t}{a}\frac{1+sin^2\theta}{(1+sin\theta)cos\theta}$	30.79	$G\frac{t}{a}\frac{cos\theta}{1+sin\theta}$	18.47
		Low: $G\frac{t}{a}\frac{1+sin\theta}{2cos\theta}$	27.71		
Gibson & Ashby [3]	t'=2t	Up: $G\frac{t}{a}\frac{1+sin^2\theta}{(1+sin\theta)cos\theta}$	30.79	$G\frac{t}{a}\frac{cos\theta}{1+sin\theta}$	18.47
		Low: $G\frac{t}{a}\frac{(2+sin\theta)^2}{5cos\theta(1+sin\theta)}$	30.79		
Grediac [28]	t'=2t	$G^{*low}_{xz}+\frac{0.787a}{h}\left(G^{*up}_{xz}-G^{*low}_{xz}\right)$	28.04	$G\frac{t}{a}\frac{cos\theta}{1+sin\theta}$	18.47
Meraghni [29]	t'=t	$G\frac{t}{a}\frac{1+2sin\theta}{2cos\theta(1+sin\theta)}$	24.63	$G\frac{t}{a}\frac{t+2asin\theta}{2(1+cos\theta)(t+asin\theta)}$	16.69
Shi [30]	t'=2t	$G\frac{t}{a}\frac{2-cos^2\theta+2*sin\theta}{4cos^3\theta}$	27.71	$G\frac{t}{2acos\theta}$	18.47
Chamis [22]	t'=t	$G\frac{3t}{4acos\theta}$	27.71	$G\frac{t}{2acos\theta}$	18.47
Noor & Burton [26]	t'=2t	Up: $G\frac{t}{a}\frac{1+sin^2\theta}{(1+sin\theta)cos\theta}$	30.79	$G\frac{t}{a}\frac{cos\theta}{1+sin\theta}$	18.47
		Low: $G\frac{t}{a}\frac{1+sin\theta}{5cos\theta}$	11.08		
Florens [25]	t'=2t	*num*	26.95	*num*	17.83

AN20: Aluminum-Nomex specimen, unit: MPa
G^{*low}_{xz} and G^{*up}_{xz} are Kelsey's ones,
num: direct numerical estimation,
t and *t'*: cell wall thicknesses (in the ribbon direction and sloping walls).

3.5.2 Validation on a full panel

The end objective of estimating effective parameters is to allow full panel predictions. This section thus compares free-free modes of a 0.40 m by 0.20 m rectangular panel for both the 3D and SVS models. The effective transverse shear moduli of the core, $G_{xz}^{\star} = 27MPa$ and $G_{yz}^{\star} = 17.8MPa$, were estimated separately in Section 3.5.1.

Figure 3.26 shows the very satisfactory results of the correlation. Examples of paired mode shapes are shown on Figure 3.27. Modes 16-17 correspond to a classical switch between modes. On the SVS, mode 16 has 5 nodal lines along x and 1 along y while the opposite is true for the 3D FEM. For modes 23-24, one has a combination. In the SVS model, mode 23 has 4-0 node lines and mode 24, 4-1 node lines. In the 3D model, the modes are close in frequency (1.6 % difference) and the number of node lines in the x-direction is unclear for both. This is visible in figure 3.28 were the node line is not in the middle. Such a dissymmetry can be due to the mesh (that has been built to be periodic and not symmetric) or to imperfect convergence of the eigenvalue solver.
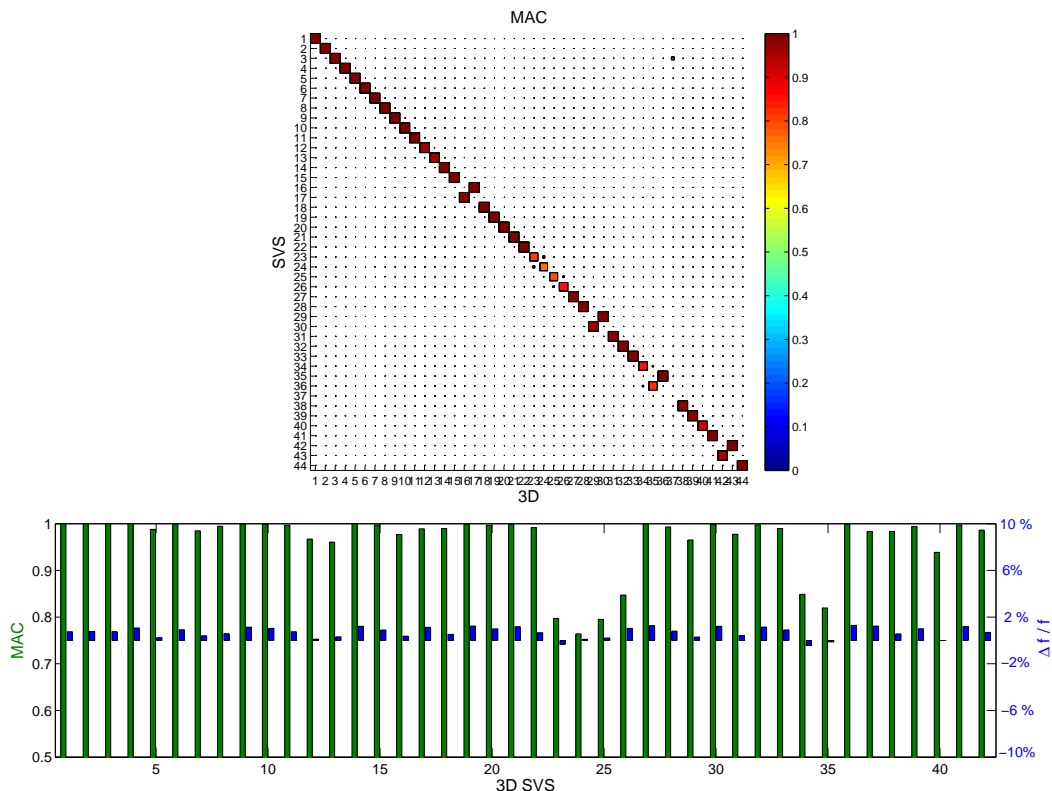
Figure 3.26: *SVS FEM/3D FEM correlation of a 0.4×0.20 m rectangular panel in free-free conditions*

Modeling of a viscoelastic honeycomb panel equipped with piezoelectric patches in view of vibroacoustic active control design

3D FEM Mode 6 at 1442 Hz

SVS FEM Mode 6 at 1429 Hz

3D FEM Mode 14 at 2171 Hz

SVS FEM Mode 14 at 2145 Hz
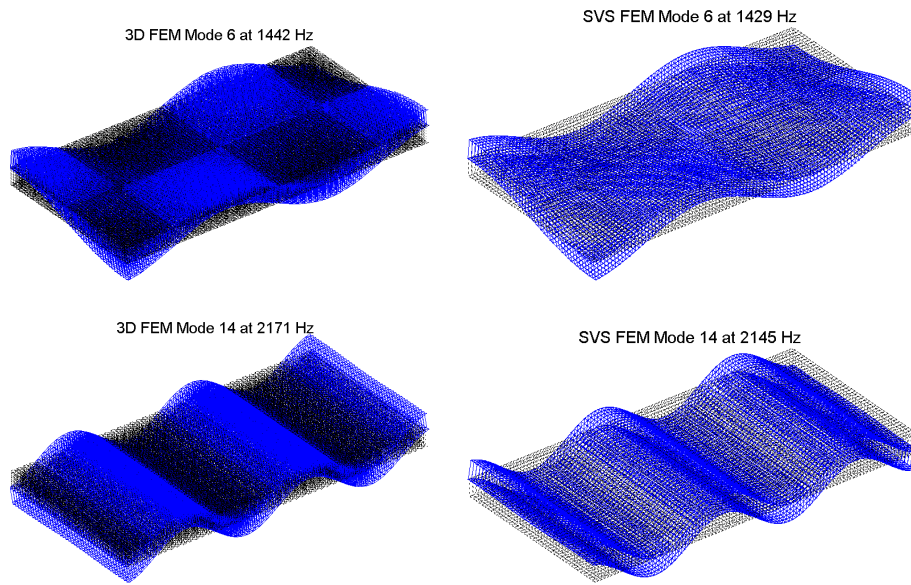
Figure 3.27: *Example of SVS/3D FEM modes correlated (6th, 14th)*

3D FEM Mode 23 at 2888 Hz

SVS FEM Mode 23 at 2898 Hz

3D FEM Mode 24 at 2936 Hz

SVS FEM Mode 24 at 2933 Hz
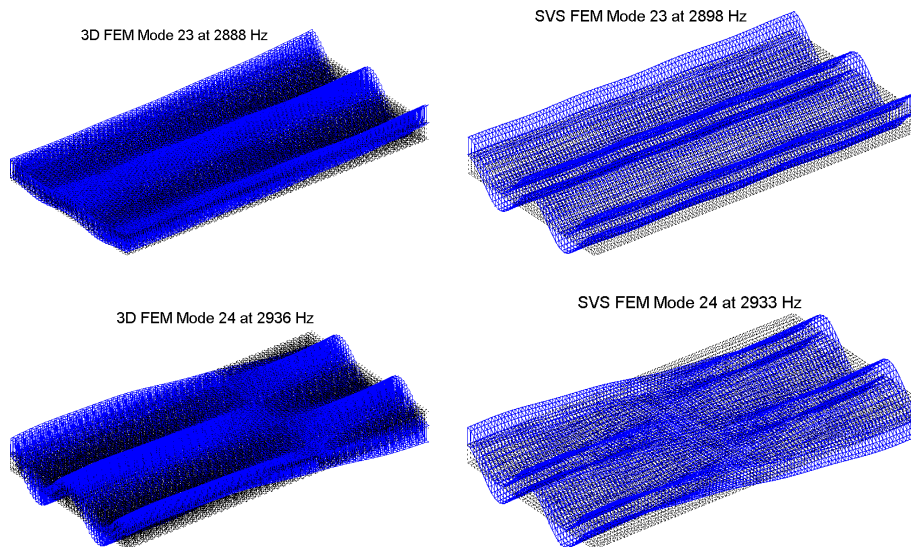
Figure 3.28: *Example of SVS/3D FEM modes poorly correlated (23rd, 24th)*

3.5.3 Influence of skin on the effective parameters

The procedure proposed in this chapter considers the whole sandwich including skins. This is consistent with the conclusion of Burton and Noor [26] that the face sheet thickness has no significant effect on the value of effective parameters. This section seeks to validate this conclusion, thus showing that the proposed approach is consistent with the many

methods presented in literature survey of section 2.3.2 that do not consider skins in the effective parameter estimation process.

As a first evaluation, one varied the skin modulus E_f in the range $[1/3, 1, 3]E_{f_0}$ with $E_{f_0} = 72.5$ GPa given in Table 3.2. Honeycomb core and adhesive properties are unchanged. Figure 3.29 clearly shows that the mean value does not depend on E_f (the change on the estimated shear modulus is lower than 0.2%). The divergence for low wavelength is very similar, which gives an indication that core dynamics are a major factor for this evolution.

The divergence for low frequency / high wavelength is significantly influenced by E_f. The analysis of the energy fractions shows that for soft skins, the drop of energy in the core occurs at lower wavelengths (higher frequencies). The divergence of the estimated modulus thus appears to be associated with an incorrect representation of the energy distribution when the energy in the core becomes small.

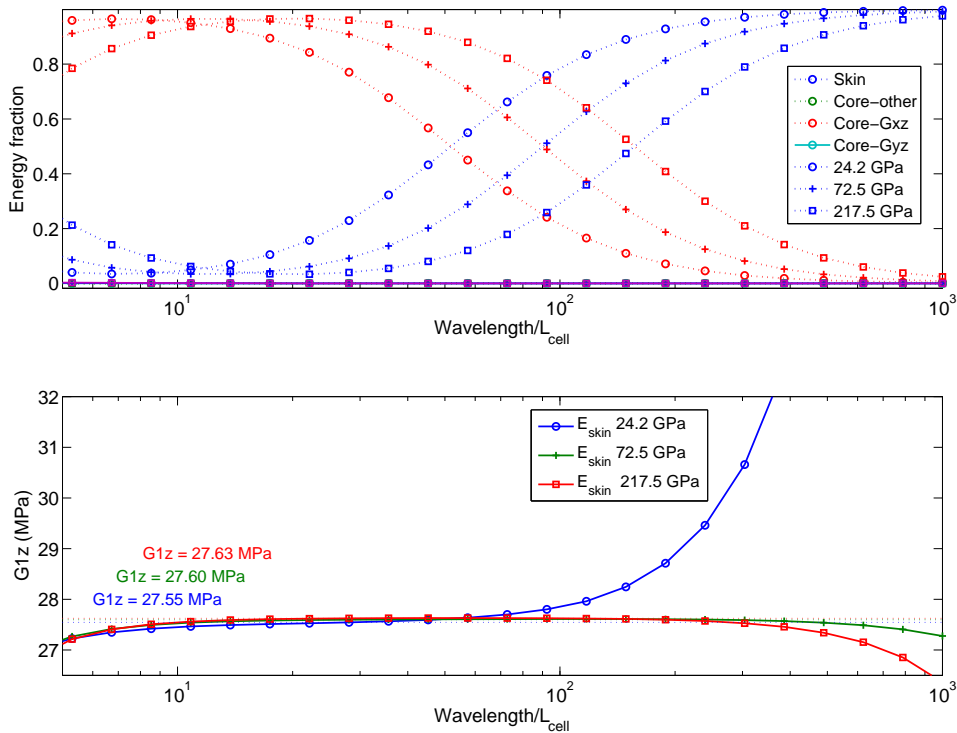**Figure 3.29:** *Top: Energy contribution of constituents for bending along x-direction - Face sheet Young modulus: $E_{f_0}/3$, E_{f_0} and $3E_{f_0}$. Bottom: Estimation of $G^\star_{xz}$ associated with no error - Core mass correction $+0.75\%$*

A similar study was performed by varying the skin thickness h_f. The low wavelength drop in core energy is clearly much more sensitive to this parameter, than to the skin

modulus. This confirms that the associated modes have a strong skin bending nature, as was already discussed in section 3.4.2. The impact on the estimated modulus is however quite small which confirms the validity of the homogeneization procedure.
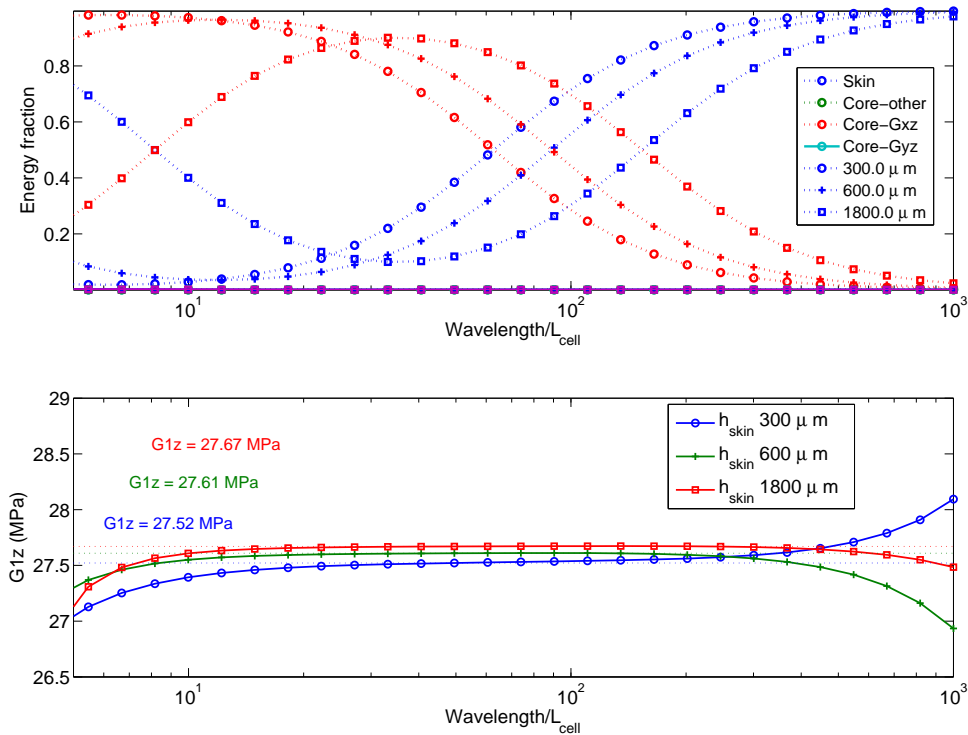
Figure 3.30: *Top: Energy contribution of constituents for bending along x-direction - Face sheet thickness: $h_{f_0}/2$, h_{f_0} and $3 * h_{f_0}$. Bottom: Estimation of $G^\star_{xz}$ associated with no error - Core mass correction $+0.75\%$*

Hohe [2] characterized the influence of the face sheets constraint on the estimation of the effective core parameters. His conclusion was that there is an important part of strain energy stored in the transition zone in the vicinity of the bonding to the face sheets and that therefore, the thickness of the core has an influence on the homogenization due to the contribution of the transition zone which could be more or less important. The strain energy in the honeycomb cells for wavelengths 60, 170 and 500, is displayed on Figure 3.31 and two skin moduli. While the strain energy distribution is clearly not uniform and significantly depends on the wavelength, a concentration near the bonding zone is only dominant for the soft skin 500 cell lengths wavelength. This case is also the only one where the highest energy is not found in the inclined cell walls. The analysis thus seems a possible starting point to explain the low frequency divergence on the equivalent moduli.
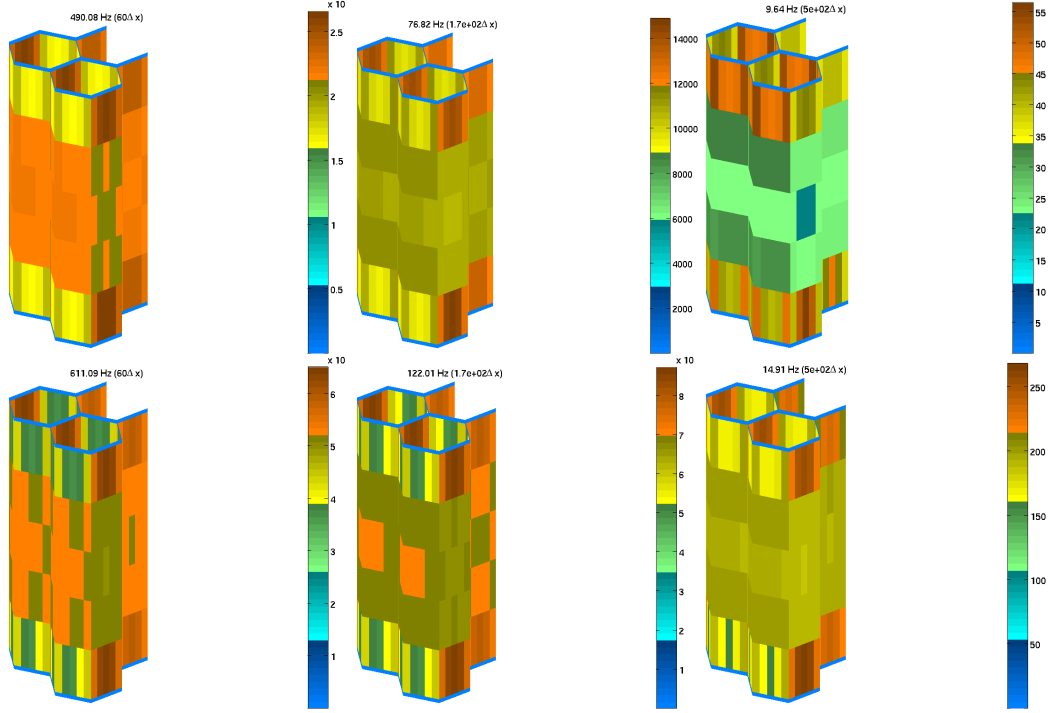
Figure 3.31: *Strain energy distribution in the core for wavelengths 60, 170 and 500. Top
: skin modulus=24 GPa. Bottom : skin modulus = 72 GPa*

3.5.4   A procedure to estimate glue properties

The proposed procedure to estimate constitutive parameters is clearly valid but requires
knowledge of constituent properties. Very often and in the proposed application, glue
properties are not well known. This section seeks to address the issue of estimating glue
and core properties separately.

The underlying logic is that modal tests, such as those presented in chapter 4, could
be used to evaluate effective parameters for multiple honeycomb thickness with identical
gluing processes. Based on these estimated effective parameters, the homogeneization
procedure proposed here could be reversed to separate constitutive parameters for the
glue and the honeycomb. The section seeks to evaluate the potential effectiveness of this
procedure to motivate a possible future implementation.

The basic assumption proposed here, is that the effective core shear modulus $G_{xz}^\star$ ver-
ifies the inverse rule of mixtures. It can be expressed as function of the pure honeycomb
effective shear modulus, noted $G_h^\star$, the equivalent glue layer effective shear modulus,
noted $G_g^\star$, and the ratio of their respective thickness to the core thickness. With notations
of the Table 3.2, one has

$$\frac{1}{G_{xz}^\star} = \frac{h_g}{h_h} \cdot \frac{1}{G_g^\star} + \frac{h_h - h_g}{h_h} \cdot \frac{1}{G_h^\star}. \tag{3.30}$$

Note that, here the equivalent core is divided into 2 equivalent layers for the bonding and 1 equivalent layer for the pure honeycomb core. Figure 3.32 gives the results of the effective parameter estimation for a range of core thicknesses. For the AN20 specimen, h_g is fixed to the value 0.6mm (0.3mm per core/skin bonding), and h_h varied from 5 to 25 mm.
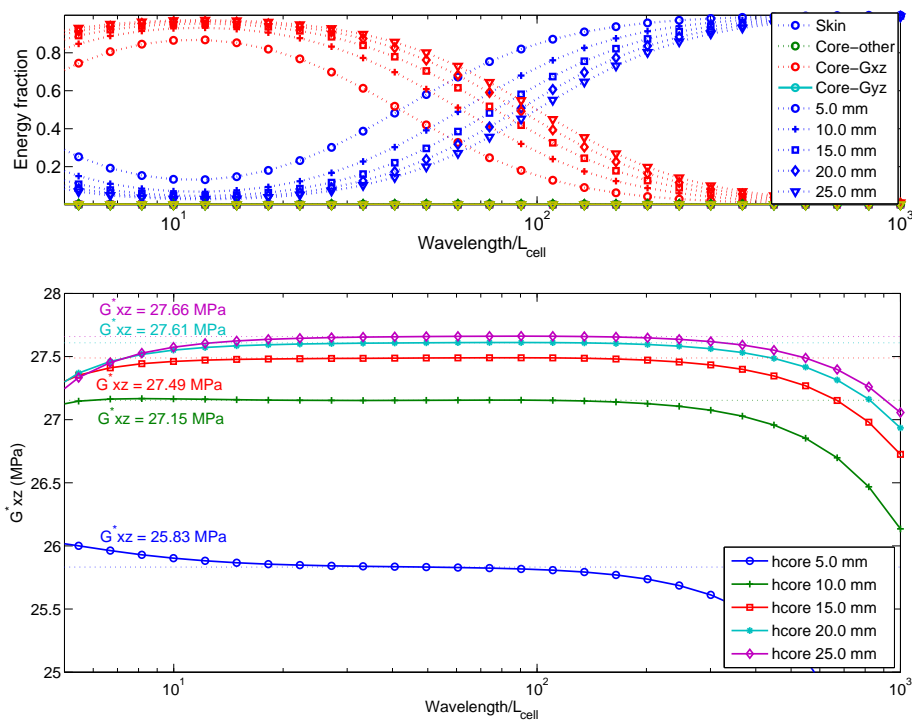

Figure 3.32: *Top: Energy contribution of constituents for bending along x-direction - Core thickness: 5, 10, 15, 20 and 25mm. Bottom: Estimation of $G^{\star}_{xz}$ associated with no error - Core mass correction $+0.75\%$*

By choosing extreme points, one deduces $G^{\star}_g = 16.08$ MPa and $G^{\star}_h = 28.2$ Mpa. Table 3.5 shows that the linear (3.30) gives a good accuracy on the effective parameters.

Table 3.5: *Comparison between the estimated core shear modulus $G_{xz}^{\star}$ through numerical homogeneization and the core modulus calculated from $G_g^{\star}$ and $G_h^{\star}$*

$G_{xz}^{\star}$ updated [MPa]	(3.30) [MPa]	Error [%]
25.83	25.83	0
27.15	26.94	-0.76
27.49	27.34	-0.56
27.61	27.54	-0.26
27.66	27.66	0
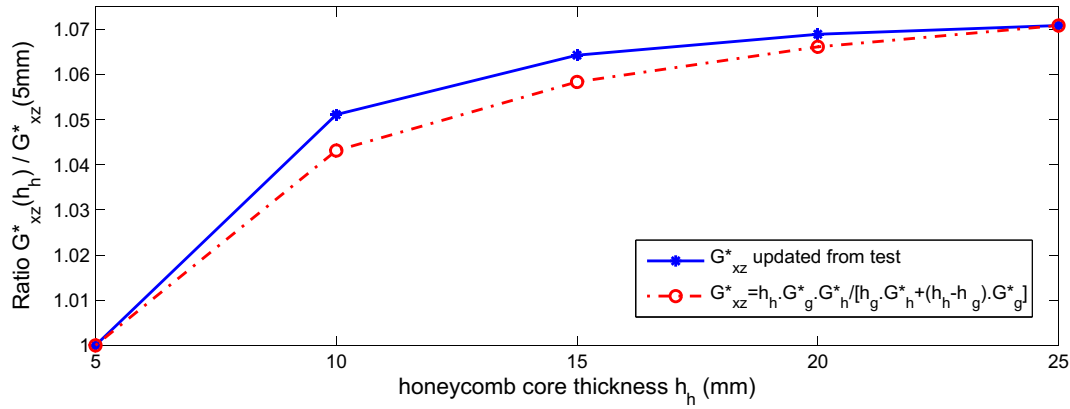
Figure 3.33: *Ratio $G_{xz}^{\star}(h_h)/G_{xz}^{\star}(5mm)$ for $G_{xz}^{\star}$ estimated through numerical homogeneization and calculated from $G_g^{\star}$ and $G_h^{\star}$ (3.30)*

A further step, that was not implemented, would update constitutive parameters of the 3D model (E_g, E_{nomex}) to match the effective parameters ($G_g^{\star}$, $G_h^{\star}$) found using experiments on a series of samples.

Chapter 4

Experimental identification of Nomex based sandwich composite properties

Contents

4.1   Introduction

While chapter 3 introduced a clear homogeneization procedure to estimate effective parameters from known cell geometry and constituent properties, it also pointed out that knowledge of these parameters was often a difficulty.

In the target application of panels, the honeycomb cores are made with Nomex paper. Nomex paper is based on short aramid fiber paper impregnated with phenolic resin. Extensive literature searches and reviews on mechanical and materials properties of Nomex paper used for Nomex honeycomb structure are present in Foo et al. [43], but this information could not be applied to the honeycomb being tested. In practice the starting point was thus an initial guess for elastic properties of glue and honeycomb listed in section 4.2.1. And this is probably a very standard case.

Two types of honeycomb sandwich were tested, Aluminum/Nomex and Carbon/Nomex. These test beams were cut in sandwich panels available at ONERA and referenced by AN20 and CN20. The aluminum skin minimizes unknowns in the skin properties, while the carbon skin is more representative or real applications. Dimensions and initial characteristics are given in section 4.2.1.

The presence of thin layers and geometric transitions that are very difficult to measure probably imply that the manufacturing process of honeycomb panels has an impact on the actual properties of their constituents. A methodology to estimate parameters from samples obtained from real panels is thus needed. Typical methodologies to measure such information are static and vibration tests.

Earlier experience with Nomex honeycomb at ONERA led to suspect that a viscoelastic behavior would be visible. Viscoelastic materials [44] are known to have frequency and temperature dependent properties. It was thus chosen to concentrate the proposed experiments on vibration tests, which allow testing at multiple frequencies, in a controlled environment, which allows analysis of temperature sensitivity. Modal tests are thus performed and model updating is used to estimate material characteristics for unknown constituents.

Test configurations and modal test results are described in section 4.2. The estimation of effective parameters is then addressed in section 4.3.

4.2   Modal tests

This section presents results of the modal test that were performed for later estimation of effective core properties. Section 4.2.1 discusses sample properties and section 4.2.2 the measurement configuration. Section 4.2.3 analyses properties of measured transfer functions and motivates the fact that the quantitative comparison can only be performed on identified modes, which are given in Section 4.2.4.

4.2.1 Test samples

Helicopter or aircraft trim panels are commonly made with non-metallic honeycomb core sandwich. Nomex based honeycomb has the major advantage to have a lower density than aluminum honeycomb. Nomex paper is based on short aramid fiber paper impregnated with phenolic resin.

Two types of honeycomb sandwich were tested, Aluminum/Nomex and Carbon/Nomex. These test beams were cut in sandwich panels available at ONERA and referenced by AN20 and CN20. The aluminum skin minimizes unknowns in the skin properties, while the carbon skin is more representative of real applications. To highlight the orthotropy of the honeycomb core, samples were cut in the longitudinal and transverse directions leading to four AN20L, AN20W, CN20L and CN20W beams. The (L) tests are however exploited in more detail since they correspond to the configuration instrumented with piezoelectric patches (see Section 5.3.1).

The dimensions are shown in Figure 4.1. AN20 and CN20 honeycomb sandwich only differ by their skins, the Nomex honeycomb core and adhesive layers are the identical.
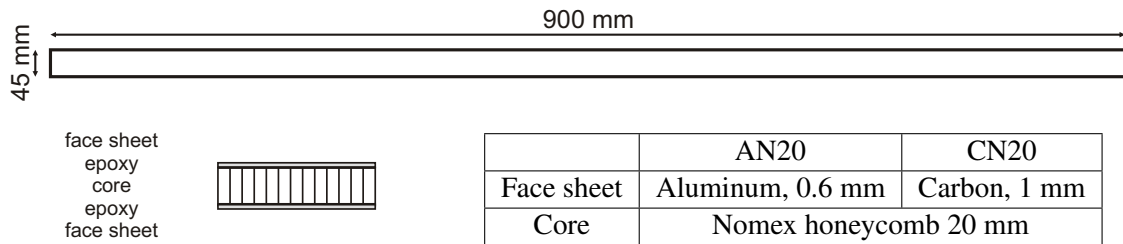

	AN20	CN20
Face sheet	Aluminum, 0.6 mm	Carbon, 1 mm
Core	Nomex honeycomb 20 mm	

Figure 4.1: *Definition test beams*

As skin properties of the CN20 Carbon skins were not well know, tensile tests were carried out on Carbon skin specimens, extracted from a sample of CN20 honeycomb sandwich. The specimens were 120mm long, 20mm large and 1mm thick, cut in both longitudinal (L) and transverse (W) orthotropic directions of the sandwich to verify the isotropic hypothesis. First, the thickness was measured with a microscope for more precision. For each sample, the thickness were measured in 3 or more points around the middle of the specimen, where the displacement has been measured during the tensile test, see Figure 4.2 (left). A force in the [0-3 kN] range was applied to the test specimen and displacement was measured in the centre. The results of the tests on 3 specimens in each direction are presented on Figure 4.2 (right). The mean value of the Young modulus in the longitudinal and transverse directions are $E_L = 44.2$ GPa and $E_W = 45.7$ GPa.
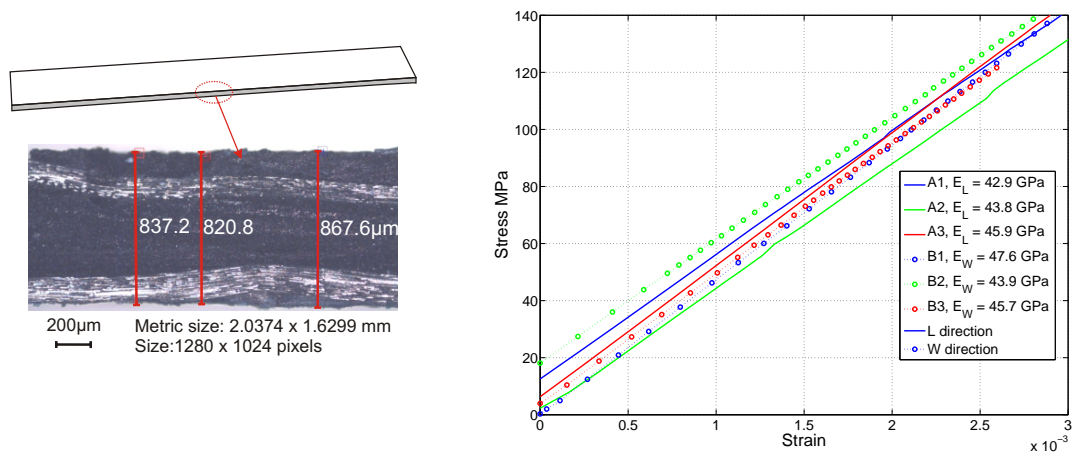
Figure 4.2: *Left: Side view of a Carbon face sheet specimen. Right: Young's moduli measured in longitudinal and transverse directions of the sandwich*

The isotropy of the carbon fiber reinforced composite face sheet is not perfect, but seems an acceptable hypothesis. The mean value chosen is 45 GPa.

Table 4.1 summarizes material values taken initially. Face sheet properties are considered well known, while honeycomb and glue parameters are considered very uncertain and will be the object of parameter estimation.

Table 4.1: *Definition of Aluminum/Nomex and Carbon/Nomex test beams parameters*

		Geometric parameters (thickness)		Material parameters (density, Young modulus)			
Face sheet	*Aluminum*	h_f	0.6	ρ_f	2.8	E_f	72.5
	Carbon	h_f	1	ρ_f	1.6	E_f	45
Honeycomb core	*Nomex*	h_h	20	ρ_h	1.38	$E_{h_{ref}}$	3
Glue	*Epoxy*	$h_g = h_f/2^{**}, t_g^*$	0.3, 0.1	ρ_g	1	$E_{g_{ref}}$	2

Length in mm, angle in rad, density in $10^3 kg/m^3$, elastic moduli in GPa.
* 3D detailed FEM assumption (Figure 3.3).
** glue modeled on the basis of the AN20 specimen.

4.2.2 Measurement configuration

Experiments in this chapter were conducted at the MSSMat laboratory of Ecole Centrale of Paris. The experimental setup is shown on Figure 4.3. To ensure the free-free conditions, the beam is suspended by 3 elastic strings. In the fourth corner the shaker is attached and hung by springs. The test beam, shaker, transducer and scanning mirror are put in a controlled environment chamber, so that tests can be made at different temperatures. All beams were tested at 25°C. Additional tests at 5°C and 45°C, were performed for the AN20L Aluminum/Nomex beam. Excitation forces are measured through
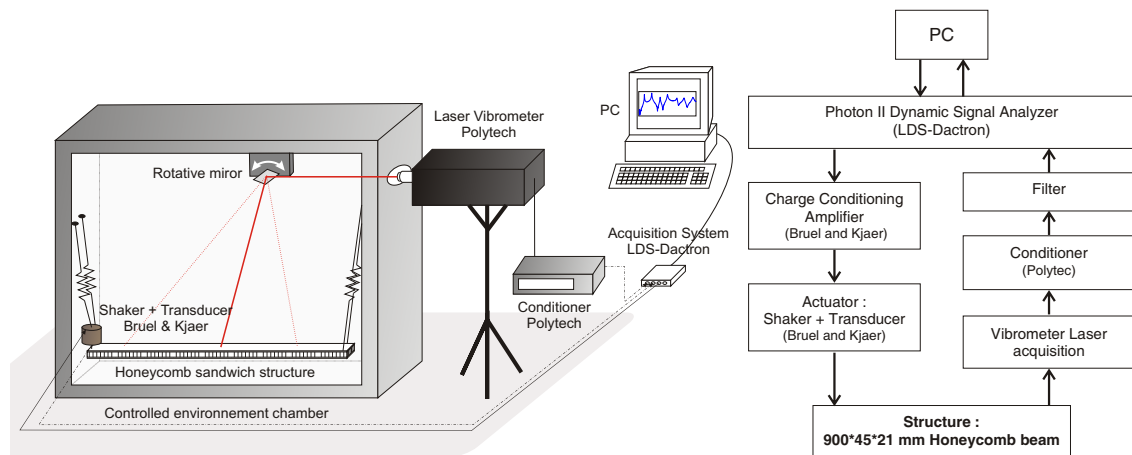

Figure 4.3: *Left: Experimental setup. Right: Acquisition chain.*

a (Bruel and Kjaer) load cell which is screwed trough the whole sandwich using fine hole (see, Figure 4.4, right). Velocities are measured using a Polytec laser vibrometer. An in house scanning mirror setup located within the environmental chamber is used to measure velocity at the various points.

The acquisition is performed using a Photon Analyzer from LDS-Dactron. The signal sent to the structure is a white noise in the 0 - 3 kHz range created by the analyzer. Load and velocity are measured and acquired into MATLAB using the Photon Active-X API. Spectrum estimation and averaging is performed using SDT functionality [34].
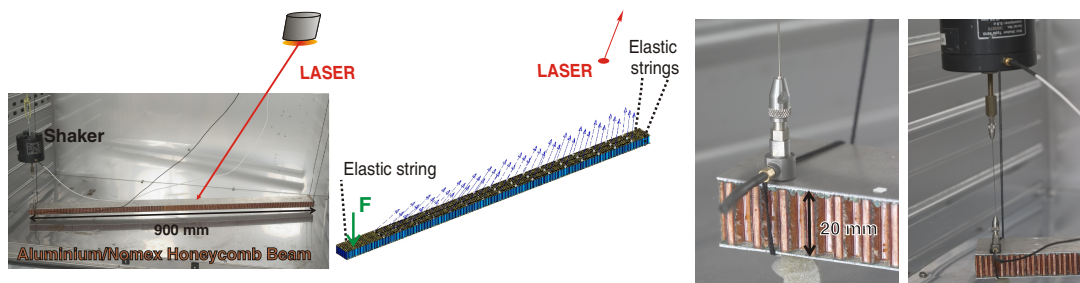

Figure 4.4: *Left: Experimental setup. Right: Shaker and Force transducer.*

Modeling of a viscoelastic honeycomb panel equipped with piezoelectric patches in view of vibroacoustic active control design

4.2.3 Frequency response functions

This section analyses raw frequency domain measurements to give a feel for the measurement quality and problems. Eventually only modes will be used in the updating process and these will be presented in the next section.

Figures 4.5 and 4.6 show the Frequency Response Functions measured at sensor 1 for the 4 beams (AN20L, AN20W, CN20L and CN20W) for test performed at 25°C. The curves indicate fairly good measurement quality up to 2.5 kHz. There is however a significant number of poorly excited modes that will be more difficult to identify.

The figures illustrate the shift on the resonance between beams along L or W directions. This shift is due to the orthotropy of the honeycomb core induced by the manufacturing process. This effect confirms the need for modeling the double thickness of the honeycomb cell walls in the longitudinal direction.
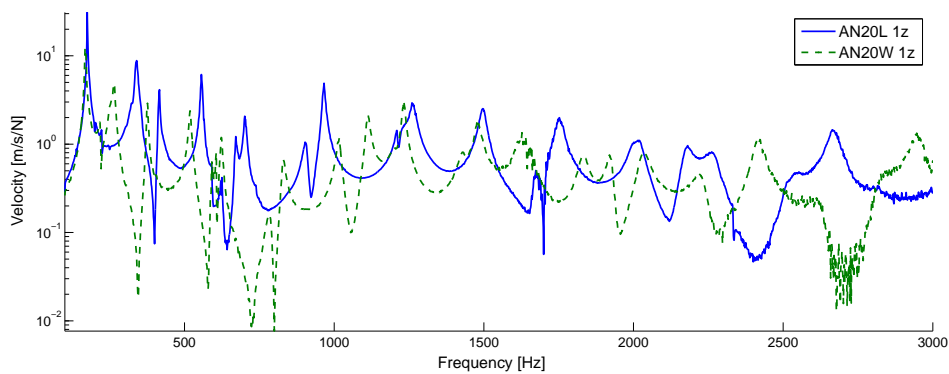

Figure 4.5: *Frequency Responses for AN20L and AN20W beams - sensor 1.*
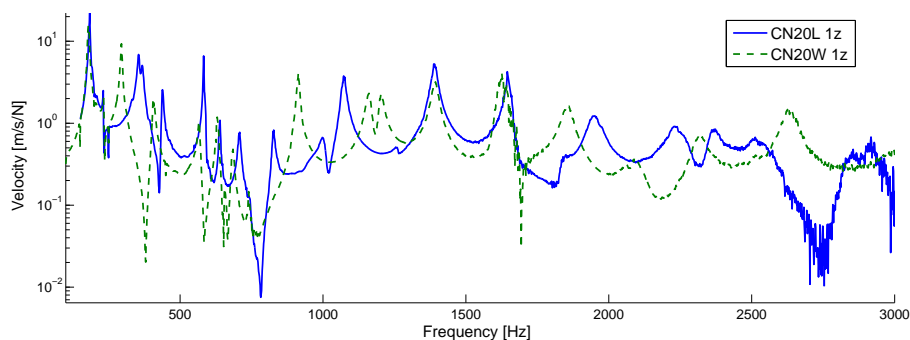

Figure 4.6: *Frequency Responses for CN20L and CN20W beams - sensor 1.*

Figure 4.7 gives a comparison of FRFs of the AN20L beam at 3 temperatures. The influence of the temperature is obvious and quite significant, with frequency shifts of the order of the frequency separation for some modes.

To confirm the impact on multiple sensors, mode indicator functions are more appropriate. Tests at 25°C and 45°C have 48 points, while only 39 points are available for the 5°C test where the measurement quality is significantly lower. Figures 4.8 and 4.9 give the multivariate mode indicator function (MMIF) [45] for the [200 800] and [200 3000] Hz ranges. The plots clearly confirm the temperature influence.
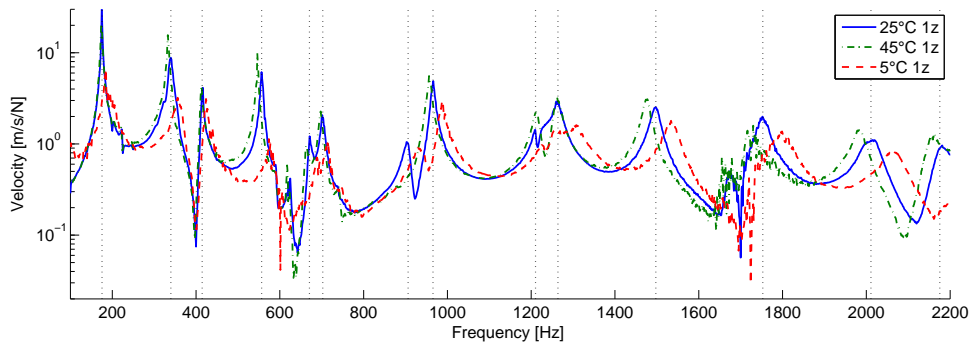

Figure 4.7: *Frequency Response at temperatures 5°C, 25°C and 45°C - AN20L beam, sensor 1z.*
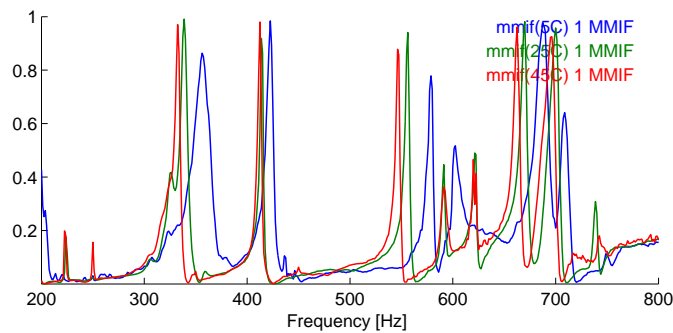

Figure 4.8: *Multivariate Mode Indicator Function for the 200 to 800 Hz.*
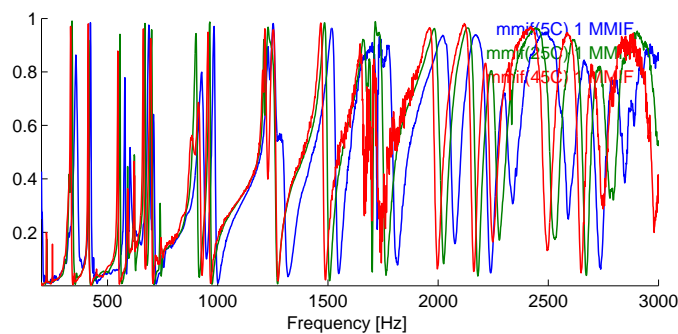

Figure 4.9: *Multivariate Mode Indicator Function for the 200 to 3000 Hz.*

Modeling of a viscoelastic honeycomb panel equipped with piezoelectric patches in view of vibroacoustic active control design

The MMIF is normally at 1 with minima near zero for resonances. The wide band plot shows that this is true in the 2-3 kHz range but not true at low frequency. The problem in these measurements was eventually tracked down to the presence of a low pass filter on the velocity measurement but not on the force. One thus has a significant phase error that changes with frequency. To allow proper identification, it is thus necessary to introduce a model that can account for such an error in series with the measurement. The modes identified in the next section thus use a series of narrow band estimates, which is a classical method to circumvent the phase problem. The problem was eventually corrected for piezoelectric tests described in section 5.3.2, but the tests of this chapter could not be redone.

4.2.4　Identified modes

Modal tests [46, 47] combine measured responses at multiple locations and in the present case acquired sequentially by displacing the vibrometer beam using the scanning mirrors. As illustrated on Figure 4.10, resonances seen at all sensors directly give an indication of mode shapes. In cases with noise or were damping is not very small and modes overlap, identification of a parametric model that fits the measured responses is needed for proper determination of mode shapes.

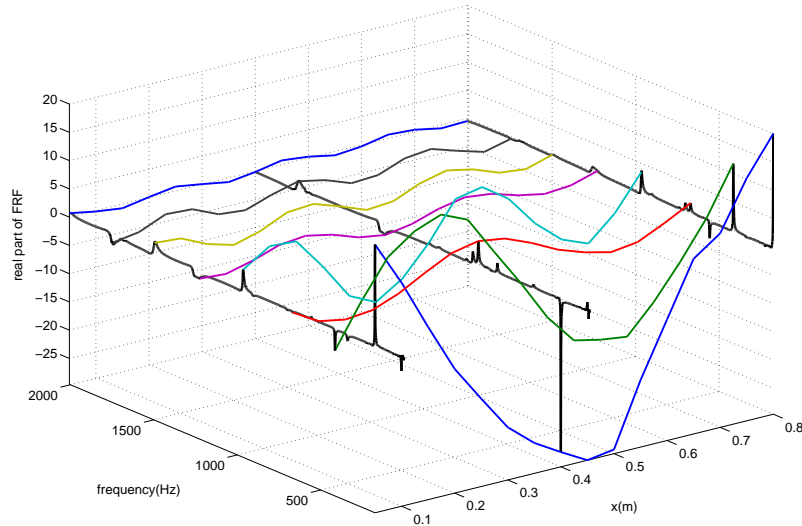**Figure 4.10:** *Real part of FRF plotted for all sensors along x.*

The pole/residue identification method [48] (base algorithm implemented in SDT [34]) is used here to extract modes from measured transfers. For each pole, the frequency f in Hz and the damping ratio ζ in % are given. In addition, the quality of the fit is quantified by the mean relative error on the Nyquist defined as follows. For pole j, and each

response H, the relative local Nyquist error e_j is evaluated by the ratio

$$e_j = \frac{\int_{\omega_j.(1-\zeta_j)}^{\omega_j.(1+\zeta_j)} |H_{Test} - H_{Id}|^2}{\int_{\omega_j.(1-\zeta_j)}^{\omega_j.(1+\zeta_j)} |H_{Test}|^2}. \tag{4.1}$$

which measures identification error around the resonance of the considered pole. For multiple responses, the mean over all sensors of the local Nyquist errors is given.

Mean Nyquist errors should be below 10% unless the response is small. Two examples with different qualities of fit are shown on Figure 4.11. On the top of the figure, local Nyquist plots show a comparison of the measured and the identified FRF around a peak, and allow a local evaluation of the quality of the fit, for response at sensor 1. On the bottom, the local error is plotted for all sensors (Response index). Mode 15 at 1497.5 Hz of AN20L beam at 25°C has small Nyquist error for the whole sensors, the mean error e is equal to 3 %, whereas mode 17 at 1752.9 Hz, has a mean error of 29 % and their properties cannot be considered as fully reliable (especially for mode shape correlation).
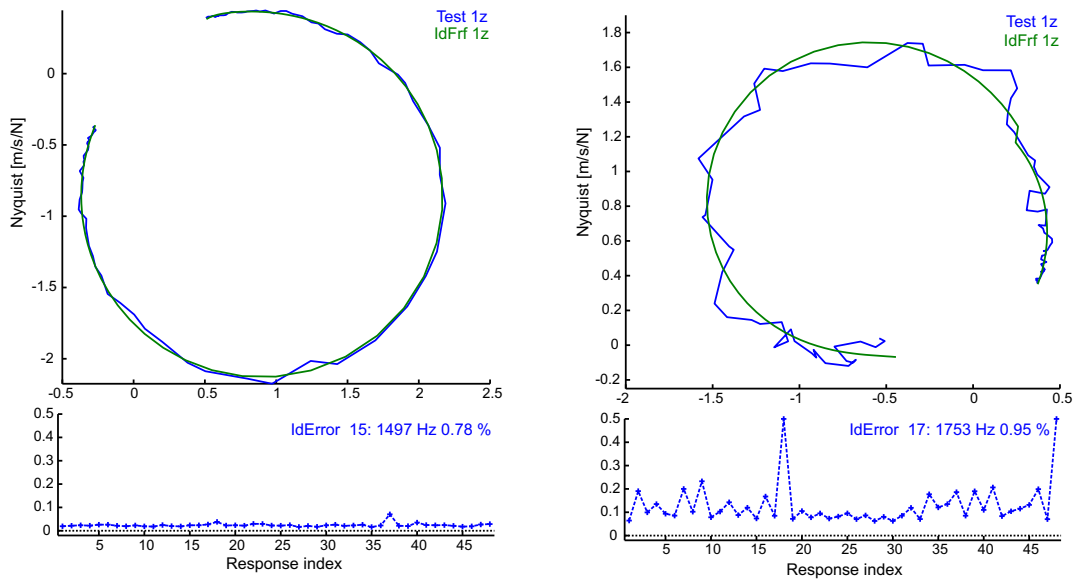
Figure 4.11: *Top: measured and identified local Nyquist plots around identified poles, sensor 1. Bottom: Nyquist error for all sensors. 15th and 17th identified poles of AN20L beam at 25°C.*

Table 4.2 gives identified modes for AN20L beam at 5°C, 25°C and 45°C. The difference in the mode numbers can be explained by the fact that some poorly excited modes are not necessarily visible in each set of transfer functions. In Table 4.3, mode shapes associated with first bending and torsion modes are plotted and matched at each temperature.
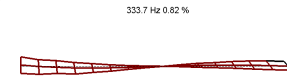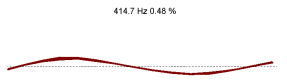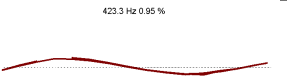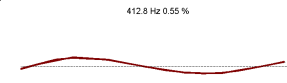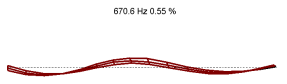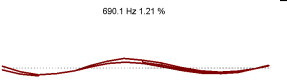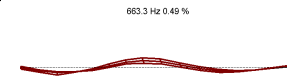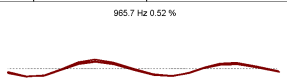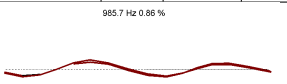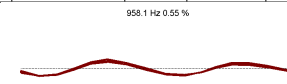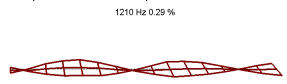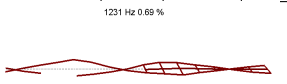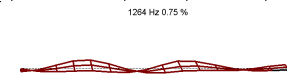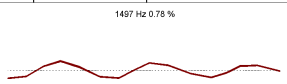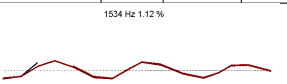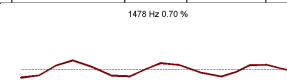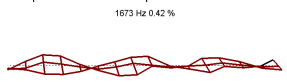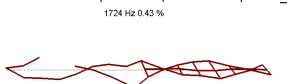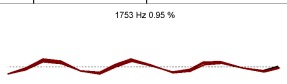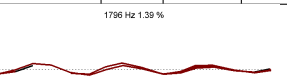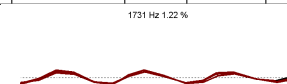
One can link the Nyquist error and the quality of the identified mode shape. From Torsion 1n to Bending 3n the error is below or close to 10%, the mode is easily identifiable. But for Bending 7n and Torsion 4n, the Nyquist error is around or above 20% and the shapes are not so perfect. For the first bending mode, the high level of e is explained by the small range $[\omega_1.(1-\zeta_1), \omega_1.(1+\zeta_1)]$, indeed e is calculated only with two measured points.

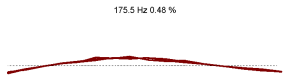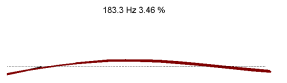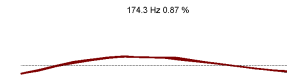**Table 4.2:** *Identified modes of AN20L beam in free-free conditions at 5, 25 and 45°C*

n	Test at 5°C			Test at 25°C			Test at 45°C		
	f	ζ	e	f	ζ	e	f	ζ	e
1	183.33	3.461	16	175.52	0.484	17	174.25	0.867	12
2	359.68	2.723	10	339.90	1.304	8	333.68	0.824	9
3	423.32	0.949	8	414.70	0.479	6	412.80	0.548	8
4	578.64	0.397	15	556.64	0.495	8	547.45	0.449	17
5	581.50	0.945	13	591.46	0.452	8	590.92	0.675	13
6	599.72	0.564	17	622.97	0.326	16	620.39	0.136	25
7	690.14	1.206	9	670.58	0.554	4	663.33	0.490	9
8	711.79	0.911	11	702.57	0.629	6	699.08	0.620	10
9	937.11	1.836	32	740.37	0.470	4	742.78	0.519	10
10	985.74	0.857	5	906.18	0.836	3	925.56	1.170	53
11	1230.77	0.690	4	965.70	0.523	3	958.12	0.553	8
12	1256.65	1.134	8	1210.48	0.294	3	1207.34	0.458	8
13	1307.54	1.127	5	1226.96	0.973	6	1215.33	0.863	10
14	1534.34	1.124	4	1263.98	0.940	4	1263.64	0.749	6
15	1724.13	0.426	35	1497.50	0.783	3	1477.85	0.697	12
16	1795.62	1.387	62	1672.50	0.418	18	1664.49	0.372	24
17	2061.29	1.080	9	1752.89	0.950	29	1731.13	1.219	37
18	2228.97	1.176	11	2011.65	2.393	8	1985.30	0.923	17
19	2332.30	1.411	16	2020.85	0.811	6	2156.88	0.856	8
20				2175.32	0.785	3	2235.44	1.005	11
21				2266.08	0.975	3	2488.96	1.249	26
22				2510.73	0.724	7	2646.45	0.804	52
23				2541.02	0.795	14			
24				2669.92	0.806	10			

Table 4.3 tracks the evolution of matched modes showing mode frequency (f in Hz), Nyquist error (n in %), shape, frequency shift (Δf/f in %) and MAC (Modal Assurance Criterion [49]) with respect to modes at 25°C.

Table 4.3: *Matched modes of AN20L beam in free-free conditions at 5°C, 25°C and 45°C*

Type	Test at 25°C			Test at 5°C					Test at 45°C				
	n	f	e	n	f	e	Δf/f	MAC	n	f	e	Δf/f	MAC
Bend 2n	1	175.5	17	1	183.3	16	4.4	92	1	174.3	12	-0.7	96
Torsion 1n	2	339.9	8	2	359.7	10	5.8	93	2	333.7	9	-1.8	98
Bend 3n	3	414.7	6	3	423.3	8	2.1	97	3	412.8	8	-0.5	98
Bend 4n + T2n	7	670.6	4	7	690.1	9	2.9	95	7	663.3	9	-1.1	92
Bend 5n	11	965.7	3	10	985.7	5	2.1	97	11	958.1	8	-0.8	93
Torsion 3n	12	1210.5	3	11	1230.8	4	1.7	95	14	1263.6	6	4.4	67
Bend 6n	15	1497.5	3	14	1534.3	4	2.5	98	15	1477.9	12	-1.3	95
Torsion 4n	16	1672.5	18	15	1724.1	35	3.1	56	16	1664.5	24	-0.5	27
Bend 7n	17	1752.9	29	16	1795.6	62	2.4	99	17	1731.1	37	-1.2	95

Modeling of a viscoelastic honeycomb panel equipped with piezoelectric patches in view of vibroacoustic active control design

To focus in data that will be used for effective parameter updating, bending mode frequencies and shifts are shown in Figure 4.12. The temperature effect is very clear, with a frequency shift around -1% when heating from 25°C to 45°C, and up to 4.4% cooling from 25°C to 5°C. This influence of temperature is typical of viscoelastic behavior as will be studied in Section 4.3.2.
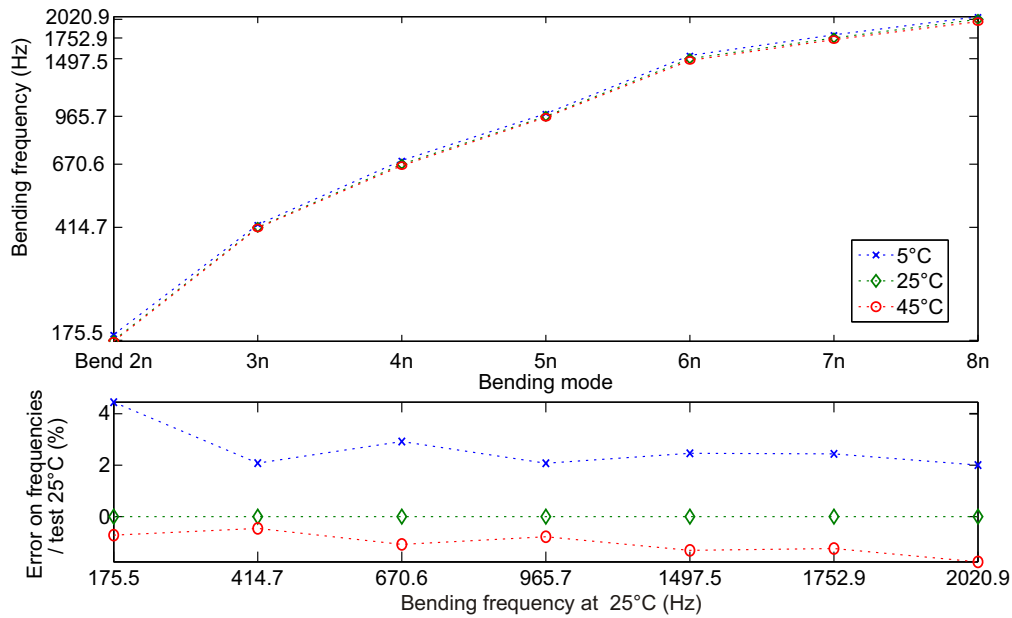
Figure 4.12: *Top: Matched bending modes at 5, 25 and 45°C. Bottom: Relative error of bending mode at 5 and 45°C regard to bending mode at 25°C*

The three other beams were not tested as thoroughly and modal results are only available at 25°C. The associated poles are listed in Table 4.4. On the whole, the measurement and thus also identification is of higher quality for Aluminum/Nomex beams. Thus, although Carbon skins properties have been measured, the update of honeycomb core shear moduli in section 4.3 was only performed for Aluminum/Nomex beams.

Modeling of a viscoelastic honeycomb panel equipped with piezoelectric patches in view of vibroacoustic active control design

Table 4.4: *Identified modes of AN20L, AN20W, CN20L and CN20W beams in free-free conditions at 25°C (f in Hz, ζ and e in %)*

n	Test AN20L			Test AN20W			Test CN20L			Test CN20W		
	f	ζ	e	f	ζ	e	f	ζ	e	f	ζ	e
1	175.5	0.484	17	168.7	0.734	15	183.2	0.617	14	178.7	1.259	13
2	339.9	1.304	8	265.1	1.426	19	355.5	0.953	4	233.1	0.596	4
3	414.7	0.479	6	375.7	0.474	8	368.5	1.239	7	294.9	0.769	5
4	556.6	0.495	8	518.7	0.730	4	437.7	0.581	7	406.6	0.731	7
5	591.5	0.452	8	623.4	0.536	36	583.3	0.246	17	566.6	0.675	6
6	623.0	0.326	16	774.6	0.327	2	639.0	0.337	13	630.6	0.372	8
7	670.6	0.554	4	800.6	0.008	2	708.0	0.607	2	656.4	0.600	7
8	702.6	0.629	6	829.2	0.693	4	826.4	0.635	8	741.0	0.416	11
9	740.4	0.470	4	1016.1	0.733	3	1004.9	1.368	20	913.7	0.431	6
10	906.2	0.836	3	1111.8	0.621	4	1072.6	0.668	5	1161.0	0.765	5
11	965.7	0.523	3	1232.2	0.459	3	1260.0	0.541	4	1202.1	0.740	4
12	1210.5	0.294	3	1433.6	0.670	12	1357.9	0.716	6	1391.6	0.785	6
13	1227.0	0.973	6	1479.3	0.677	3	1390.7	0.648	5	1622.7	0.741	29
14	1264.0	0.940	4	1656.6	0.175	28	1648.1	0.083	10	1857.5	0.954	10
15	1497.5	0.783	3	1830.9	0.901	5	1832.9	0.939	9	2073.7	1.146	34
16	1672.5	0.418	18	1923.6	0.470	5	1944.8	1.114	10	2321.9	0.830	21
17	1752.9	0.950	29	2032.2	0.950	4	2232.8	0.385	12	2526.0	0.463	21
18	2011.6	2.393	8	2226.3	0.945	7	2363.2	0.922	9	2638.3	0.671	15
19	2020.8	0.811	6	2422.0	0.667	56	2518.3	0.160	9	2788.7	0.303	14
20	2175.3	0.785	3	2622.0	0.936	15	2844.6	0.115	11	3015.1	0.127	16
21	2266.1	0.975	3	2814.6	0.897	28	2922.4	0.226	22	3232.3	0.207	23

4.3 Effective properties of Nomex honeycomb

The objective of modal tests shown in the previous section was to give a reference to allow estimation of unknown core properties.

Section 4.3.1 addresses correlation principles and gives results for the AN20L and AN20W beams.

Since one suspects viscoelastic behavior, updating of the core shear modulus is made mode by mode and for the 3 temperatures using tests on the AN20L beam which are the most complete. The result, presented in Section 4.3.2, confirms viscoelastic behavior.

Finally Section 4.3.3 discusses fitting an analytic viscoelastic model to the measured points.

4.3.1   Test/analysis correlation

The first step of test/analysis correlation is the spatial correlation relating model DOFs with sensor positions and directions. The construction of observation matrix relating spatial fields on DOFs (39420 DOF in the case of the SVS model) with observation at sensors (48 laser targets here) is based on the configuration shown in Figure 4.13. The matching performed in SDT uses the shape functions associated with the underlying elements and thus does not require coincidence of test and FEM nodes.
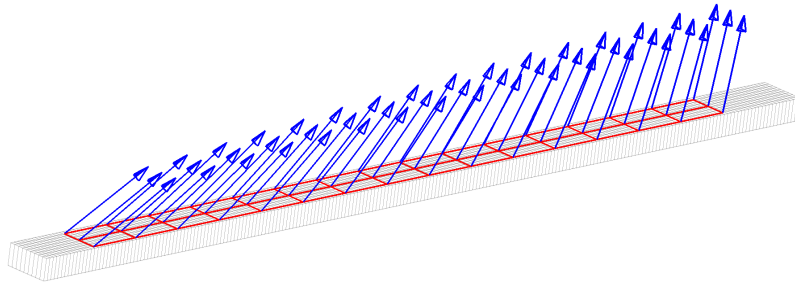
Figure 4.13: *Sensors, test wire-frame, FEM nodes*

Once topology correlation done, one can compare test and FEM modes at sensors using the Modal Assurance Criterion (MAC [49]). One reminds that a value close to 1 indicates good correlation. To compare transfers, one further needs to define input locations and affect a damping value to each FEM mode.

To start the correlation, one assumes elastic behavior and uses the effective shear moduli presented in Section 3.5.1. Sample superposition of test and FEM modes are shown in Figure 4.14, while Figure 4.15 gives the overall correlation in MAC and frequencies. The correlation is quite good despite the presence of additional test modes (in-plane modes in particular).

When considering bending modes only in Figure 4.16, the frequency error between paired modes shows an obvious increase with frequency (from -1.3 % for the first mode to 20% for the last). Similar results are found at other temperatures and shown in Figures 4.17 and 4.18.
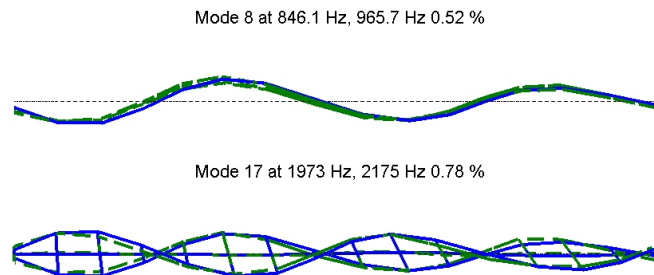
Figure 4.14: *Examples of paired test/analysis mode shapes. Top: Bending mode 5 nodes at 965.7 Hz. Bottom: Torsion mode 5 nodes at 2175 Hz.*
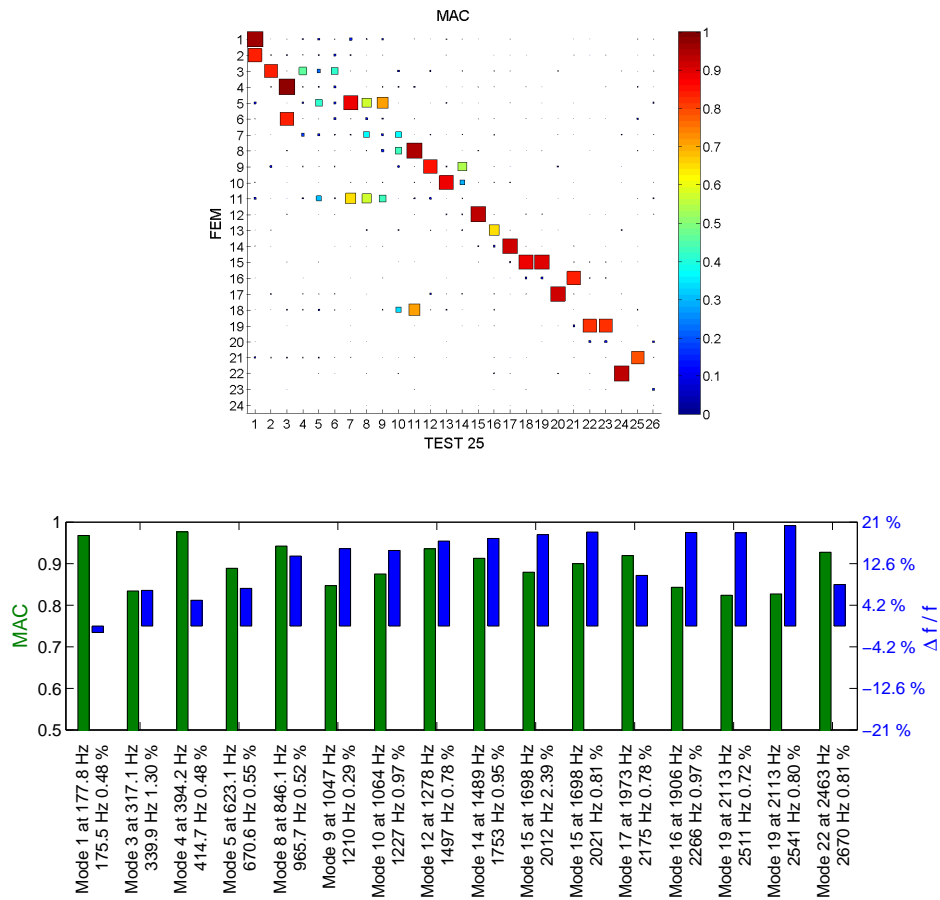
Figure 4.15: *MAC and frequency error at 25°C. All modes.*
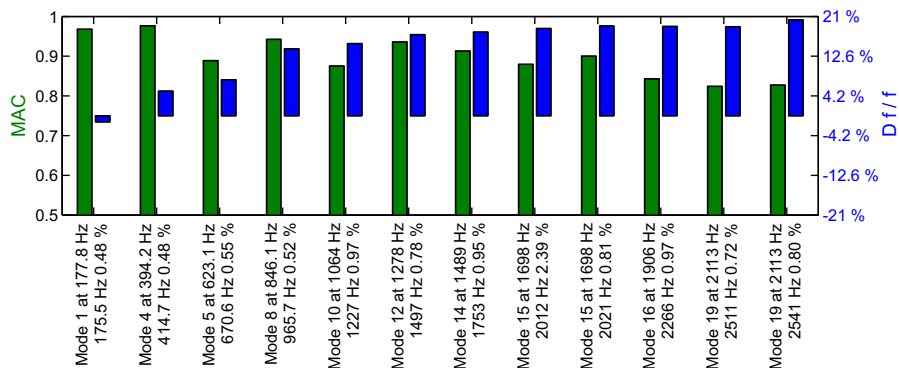
Figure 4.16: *MAC and frequency error for bending modes at 25°C.*

Modeling of a viscoelastic honeycomb panel equipped with piezoelectric patches in view of vibroacoustic active control design
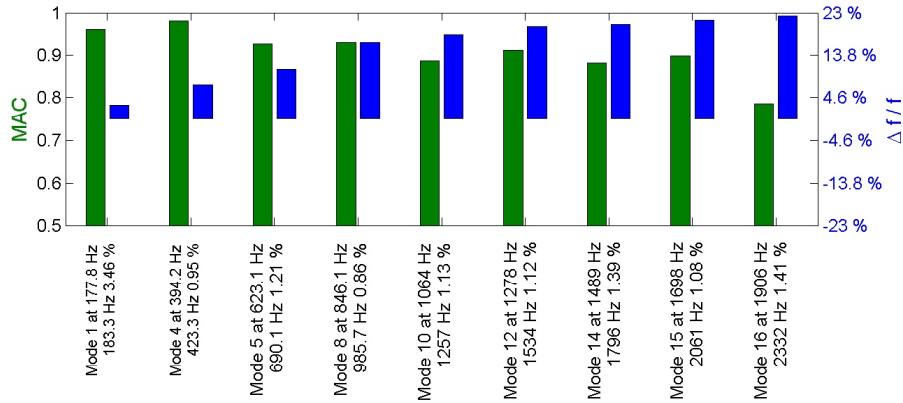
Figure 4.17: *MAC and frequency error for bending modes at 5°C.*
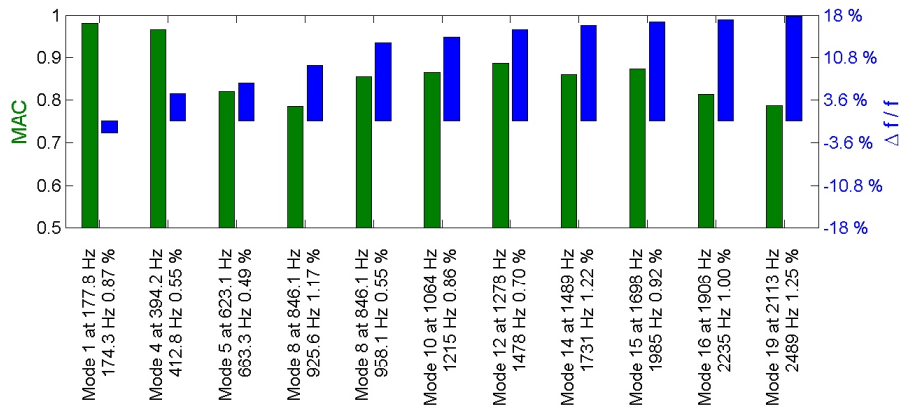
Figure 4.18: *MAC and frequency error for bending modes at 45°C.*

4.3.2 Estimated shear modulus as a function of frequency and temperature dependence

In the considered experiments, the skin properties are well known. As seen in Section 3.4.2, parameters with most influence on the modal frequencies are thus $G^{\star}_{xz}$ and $G^{\star}_{yz}$, for the L and W configurations respectively. Having a single influential parameter, running the parameter updating loop shown in Figure 4.19 is fairly direct and can be done for each bending mode in the test. In practice, the procedure can be somewhat lengthy so that reduced models described in Section 3.2.2 were used.
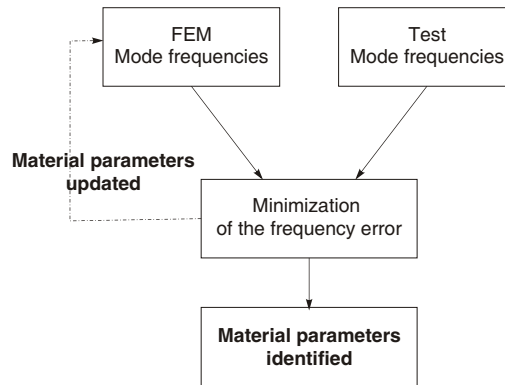
Figure 4.19: *Process of parameter estimation by updating*

The result of the procedure is a modulus value at each of the modal frequencies shown in Figure 4.20. Figure 4.12 showed a deviation of the bending frequencies increasing with frequency and decreasing with temperature. This translates here into a modulus with the same trends, which are typical for viscoelastic materials [44, 50]. In the considered experiments (see Table 4.2), the modal damping in not very well estimated and could not be used for a relevant validation of the viscoelastic behavior.
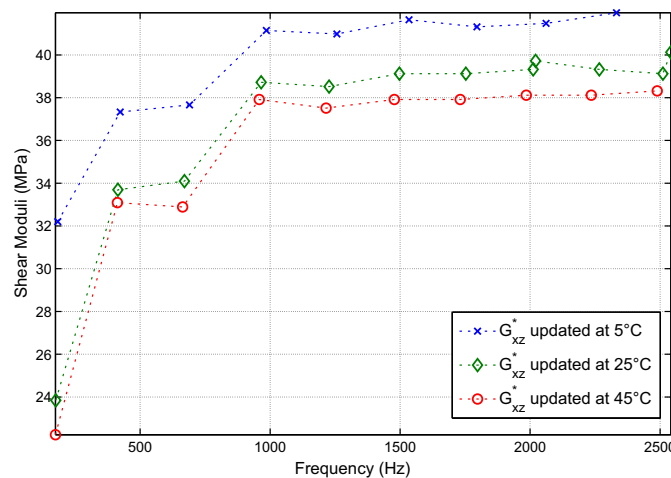
Figure 4.20: *Equivalent shear modulus $G_{xz}^{\star}$ of the core (honeycomb+glue) as a function of frequency and temperature.*

To gain a better understanding of possible errors in this procedure, Figure 4.21 gives the energy fraction associated with the $G_{xz}^{\star}$ and $G_{yz}^{\star}$ shear moduli in the test bandwidth. One clearly sees the bending modes with energy associated with $G_{yz}^{\star}$ increasing (20 % for the first mode, 48 % for the second, ...) and the torsion modes having decreasing energy (93 % for the first mode, ...). Above 2 kHz more complex shapes are found and the energy fraction associated with $G_{yz}^{\star}$ starts to pick up. The relatively small energy

fraction in the first mode may cast some doubt on the modulus value estimated for the first mode in Figure 4.20. Re-use of the estimated law on the CN20 beam equipped with piezoelectric patches will however confirm the value (Section 5.3.3).
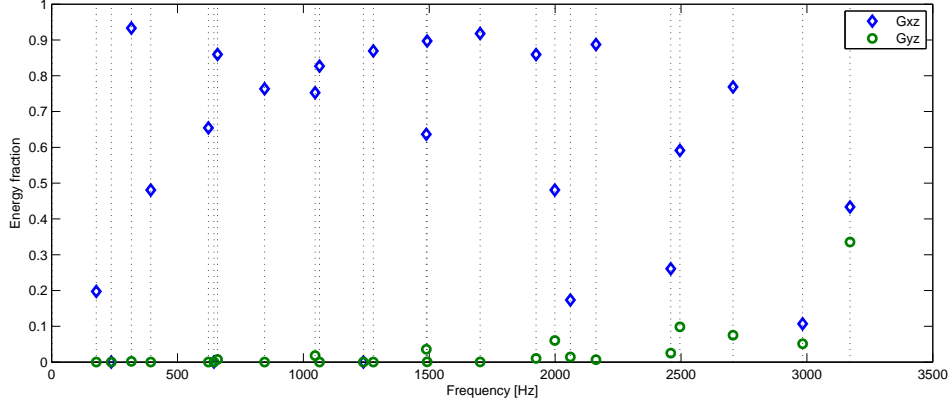
Figure 4.21: *Energy fraction relative to $G_{xz}^{\star}$ and $G_{yz}^{\star}$ shear moduli for AN20L test beam.*

One has thus demonstrated a modulus change from low to high frequency is nearly a factor 2 and one has a strong variation in the 0-1 kHz range which is the low frequency range where active control is typically considered to limit vibrations levels, when passive mechanisms are not yet efficient. To predict responses at all frequencies, an expression of G as a function of frequency is needed and a procedure is discussed in the next section.

4.3.3   Analytic representation of the complex modulus

Viscoelasticity problems can be solved as elasticity problems with a complex modulus that depends on frequency. This property is known as the elastic/viscoelatic equivalence principle [51, 44]. The complex modulus G is characterized by a constant storage moduli G' and loss factor η,

$$G(s) = G'(1+j\eta) \tag{4.2}$$

A four parameter fractional derivative model, function of the Lapace variable *s*,

$$G = G_{max} + \frac{G_{min} - G_{max}}{1 + (\frac{s}{\omega_0})^\alpha}, \tag{4.3}$$

is known to allow a compact representation of the frequency dependence of the modulus for many viscoelastic materials [52, 50]. The high G_{max} and low G_{min} frequency moduli correspond to real asymptotes, while the ω and α coefficients influence the frequency of the maximum loss factor and its value, which are related to the slope of the real modulus and the point at which this slope is maximum.

A simple non-linear least squares matching the analytic expression of $G' = \mathcal{R}e(G(s))$ and the estimated moduli at test frequencies, was used to estimate the four parameters in (4.3). The optimization was performed using the MATLAB `fminsearch` function. Results for both moduli (based on the AN20L and AN20W tests) are shown in figure 4.22.
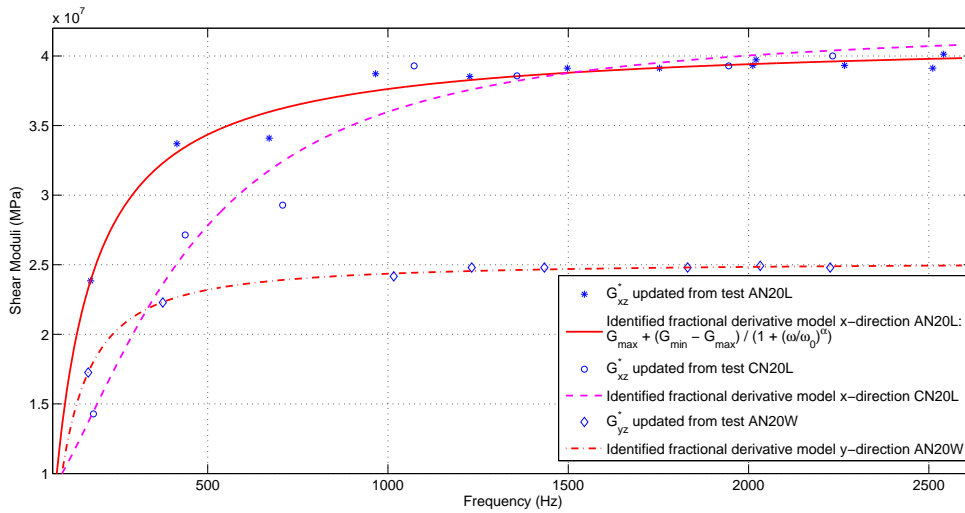
Figure 4.22: *Experimental transverse shear moduli G^*_{xz} and G^*_{yz} updated and viscoelastic law fitting. AN20L, CN20L and AN20W beams*

Figures 4.23 and 4.24 show the test/analysis correlation performed with the estimated $G^\star_{xz}(f)$ and $G^\star_{yz}(f)$. Correlation for the initial constant modulus is shown in Figure 4.23 for the AN20L and figure 4.24 for the AN20W. Clearly the frequency dependent modulus gives much better correlation in both configurations.
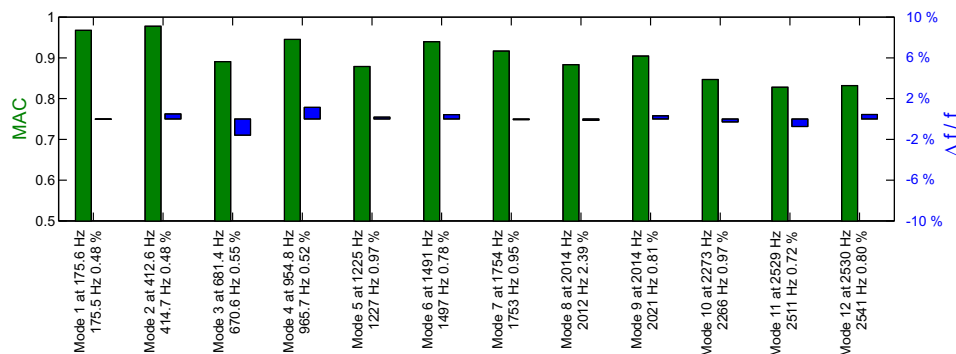
Figure 4.23: *Test/analysis correlation with updated G^*_{xz} at $25°C$ - MAC and frequency error for bending modes.*

Modeling of a viscoelastic honeycomb panel equipped with piezoelectric patches in view of vibroacoustic active control design
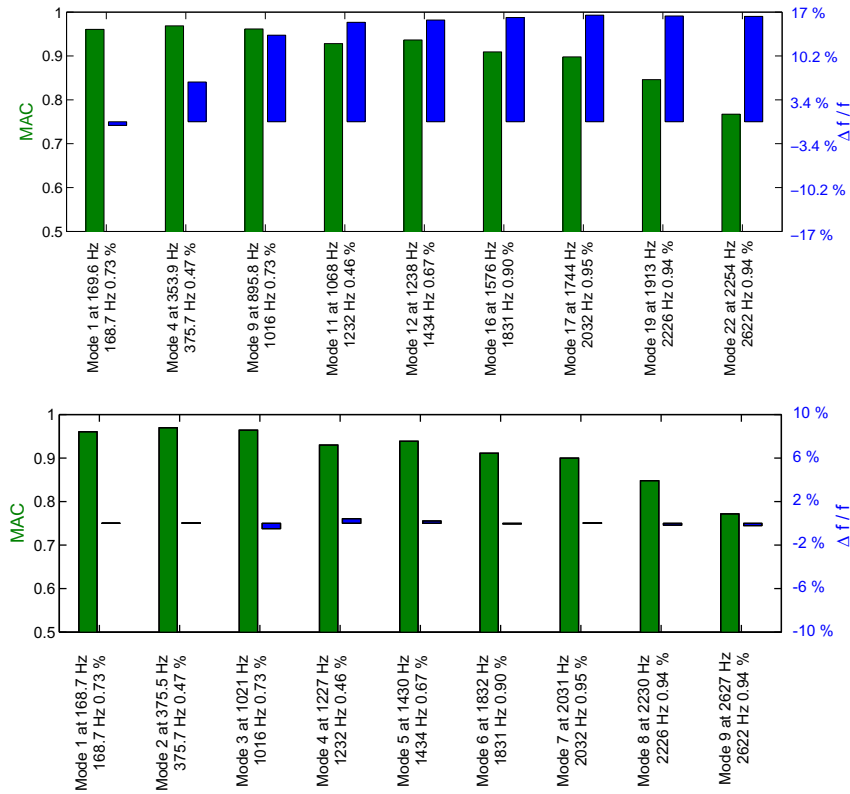
Figure 4.24: *Test/analysis correlation with $G_{yz}^* = 18$ MPa (top) and updated G_{yz}^* (bottom) at $25°C$ - MAC and frequency error for bending modes*

The effective core parameters, updated by test/analysis correlation on Aluminum/Nomex specimen, should be characteristic of the core itself. Thus, the frequency dependent effective parameters were reused for Carbon/Nomex sandwich beam. Due to sequencing of the tests, this validation is done for the piezoelectric excitation to laser measurement that will be introduced in the next chapter. Figure 4.25 clearly indicates that for a modulus adapted at 700 Hz, resonances below are too high (the modulus is overestimated), while resonances above are underestimated (the modulus is too low). Using the analytic representation of the shear modulus $G_{xz}^\star(f)$, predictions fit the measured responses extremely well.

Note that the transfer is obtained by using (3.15) to build the dynamic stiffness at each frequency and the fixed basis reduction procedure outlined in figure 3.5 to speed computations.

Modeling of a viscoelastic honeycomb panel equipped with piezoelectric patches in view of vibroacoustic active control design
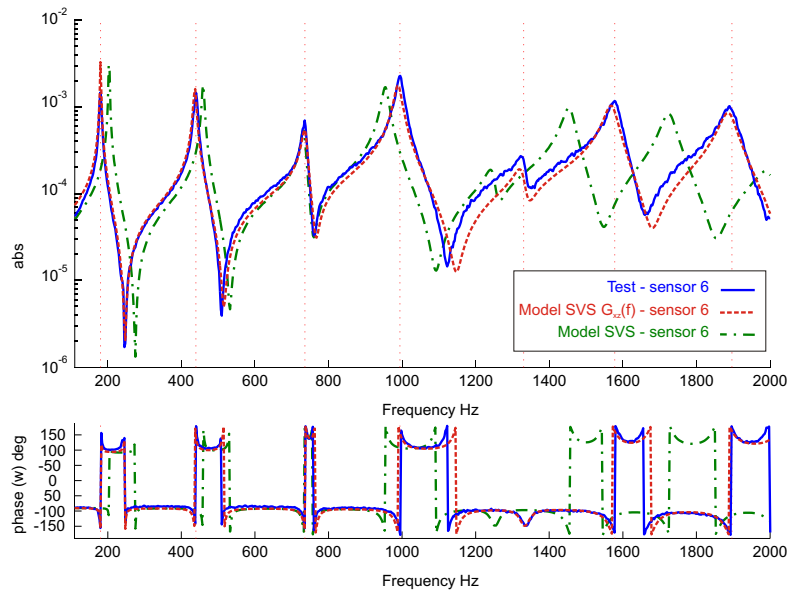
Figure 4.25: *Test/Analysis Frequency Response Functions of a Carbon/Nomex honeycomb beam - Piezo 1 actuator - Laser sensor 6*

The good quality of end prediction should not occult the fact that these tests were not very well calibrated. To illustrate the issue, one generated multiple estimates of $G(s)$ for variations in the CN20 skin properties considered to be within realistic error bounds. The values shown in Figure 4.26, clearly demonstrate the need to test skin properties with high accuracy.
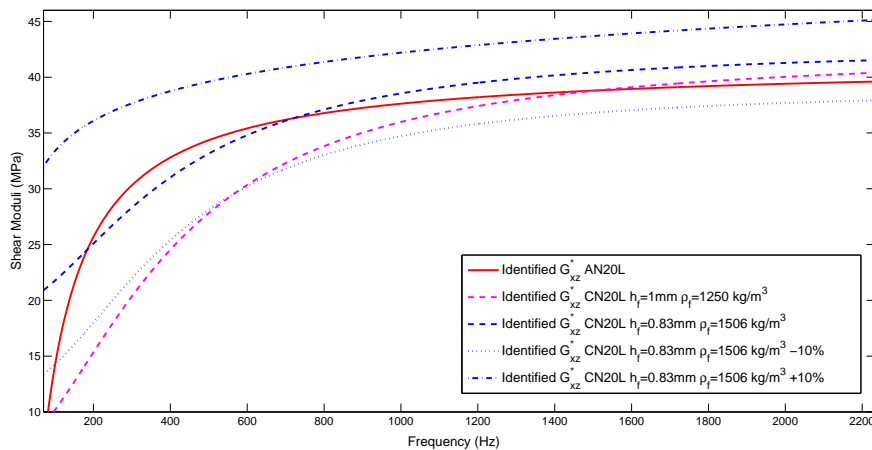
Figure 4.26: *Influence of skins thickness on the viscoelastic law of experimental transverse shear modulus G_{xz}^* for CN20L beam, $h_f = 1mm$ and 0.83mm, compared to G_{xz}^* for AN20L beam*

Modeling of a viscoelastic honeycomb panel equipped with piezoelectric patches in view of vibroacoustic active control design

Chapter 5

Finite Element Model of Honeycomb panel equipped with piezoelectric patches

Contents

5.1   Introduction

Piezoelectric materials are ceramics with the property of producing electric charge under external force. This direct effect of piezoelectricity is used for sensing. The reverse property, which consists of creating a strain in the medium under electric field, is used for piezoelectric actuators. For more details on piezoelectric materials, see Preumont's handbook [10]. Rectangular piezoelectric actuators and sensors are classically used for active structural acoustic control (ASAC) on honeycomb sandwich composite trim panels. Other shapes of patch can be found in literature, but only rectangular patches available on the market [53] are studied here.

The issue of this chapter is to understand how a piezoelectric patch coupled with the sandwich behaves and how to improve its efficiency. With this intention, The CN20L sandwich specimen with Carbon fibers reinforced composite for skins and Nomex based honeycomb core (described in Section 4.2.1), equipped with piezoelectric patches, is modeled and tested. Preliminary updating of the CN20L beam have been made, presented in Section 4.3.

Section 5.2 recalls existing finite element formulation of piezoelectric medium, developed by Piefort [9]. This FE formulation is implemented in the existent SVS FE model of honeycomb core sandwich composite in MATLAB/SDT. In Section 5.3 the FE analysis of CN20L beam equipped with 3 piezoelectric patches is compared with vibrating tests. One searches to validate the FE model of honeycomb sandwich with integrated piezoelectric patches by comparing the modal behavior and frequency responses.

Experiments have revealed a local behavior of the piezoelectric actuator. Section 5.4 addresses this local phenomenon, and in particular the ability of the FE model to reproduce the behavior in the vicinity of the actuator. Some additional experiments with refined measuring grid have been led to validate those observations.

In Section 5.5, one is interested to the use of a simplified FE model, which is compared with the previous FEM, for industrial purpose.

5.2   Models of piezoelectric medium

A piezoelectric patch bonded on plate structure is clasically modeled by a multi-layer approach [9]. Using the multi-layer laminate theory, without piezoelectric behavior, summarized in Section 2.2.3, the electro-mechanical coupling of the piezoelectric medium is first introduced (Section 5.2.1). Finite element (FE) approach is applied to piezoelectric multi-layer laminate and leads to state space model (Section 5.2.2). Then, theoretical resolution of this FE problem is presented in Section 5.2.3. Models presented in this section are implemented in MATLAB/SDT and validated on honeycomb beam specimen equipped with piezoelectric patches, Midé [53] QuickPack QP20W, bonded on the skins (Section 5.3).

5.2.1 Multi-layer plate formulation with piezoelectric laminate

In this section, the global multi-layered laminate theory is used for piezoelectric laminate. The layers are constituted with piezolectric material, then electrical equations that governs the medium and their coupling with the linear elasticity have to be considered.

From this section, the notations of the IEEE standard [54] are used,

Table 5.1: *IEEE standard and elasticity notations*

	Elasticity	IEEE Std.
Stress (N/m^2)	$\{\boldsymbol{\sigma}\}$	$\{\mathbf{T}\}$
Strain	$\{\boldsymbol{\varepsilon}\}$	$\{\mathbf{S}\}$

One recalls that engineering notation is used for strain vector (see Section 2.2.2).

In the scope of the piezoelectric patch FE model, the following assumptions are set, see [54] for justification

- quasi-electrostatic approximation,

- thermoelectric coupling neglected,

- linear piezoelectricity,

- uniform electric field and displacement across the thickness and oriented along the normal direction to the multilayer mesh-plane.

Under these hypotheses, the electrical and mechanical constitutive equations for 3D piezoelectric material are coupled [55]

$$\{\mathbf{S}\} = \left[\mathbf{s^E}\right]\{\mathbf{T}\} + [\mathbf{d}]^T\{\mathbf{E}\} \tag{5.1}$$

$$\begin{Bmatrix} S_{11} \\ S_{22} \\ S_{33} \\ S_{23} \\ S_{31} \\ S_{12} \end{Bmatrix} = \underbrace{\begin{bmatrix} s_{11} & s_{12} & s_{13} & 0 & 0 & 0 \\ s_{12} & s_{22} & s_{23} & 0 & 0 & 0 \\ s_{13} & s_{23} & s_{33} & 0 & 0 & 0 \\ 0 & 0 & 0 & s_{44} & 0 & 0 \\ 0 & 0 & 0 & 0 & s_{55} & 0 \\ 0 & 0 & 0 & 0 & 0 & s_{66} \end{bmatrix}}_{\text{Orthotropic material compliance}} \begin{Bmatrix} T_{11} \\ T_{22} \\ T_{33} \\ T_{23} \\ T_{31} \\ T_{12} \end{Bmatrix} + \underbrace{\begin{bmatrix} 0 & 0 & d_{31} \\ 0 & 0 & d_{32} \\ 0 & 0 & d_{33} \\ 0 & d_{24} & 0 \\ d_{15} & 0 & 0 \\ 0 & 0 & 0 \end{bmatrix}}_{\text{PZT piezoelectric coupling}} \begin{Bmatrix} E_1 \\ E_2 \\ E_3 \end{Bmatrix}$$

$$\{\mathbf{D}\} = [\mathbf{d}]\{\mathbf{T}\} + \left[\boldsymbol{\varepsilon^T}\right]\{\mathbf{E}\} \tag{5.2}$$

Modeling of a viscoelastic honeycomb panel equipped with piezoelectric patches in view of vibroacoustic active control design

$$
\left\{ \begin{array}{c} D_1 \\ D_2 \\ D_3 \end{array} \right\} = \underbrace{\left[\begin{array}{cccccc} 0 & 0 & 0 & 0 & d_{15} & 0 \\ 0 & 0 & 0 & d_{24} & 0 & 0 \\ d_{31} & d_{32} & d_{33} & 0 & 0 & 0 \end{array} \right]}_{PZT\ piezoelectric\ coupling} \left\{ \begin{array}{c} T_{11} \\ T_{22} \\ T_{33} \\ T_{23} \\ T_{31} \\ T_{12} \end{array} \right\} + \underbrace{\left[\begin{array}{ccc} \varepsilon_{11}^T & 0 & 0 \\ 0 & \varepsilon_{22}^T & 0 \\ 0 & 0 & \varepsilon_{33}^T \end{array} \right]}_{Permittivity} \left\{ \begin{array}{c} E_1 \\ E_2 \\ E_3 \end{array} \right\}
$$

where, $\{\mathbf{D}\}$ is electric displacement (C/m^2), $\{\mathbf{E}\}$ is the electric field (V/m), $\{\mathbf{S}\}$ the strain and $\{\mathbf{T}\}$ the stress (N/m^2). The matrix $[\mathbf{s^E}]$ is the compliance under constant electric field, $[\mathbf{d}]$ the piezoelectric constants (m/V or C/N) and $[\boldsymbol{\varepsilon^T}]$ is the dielectric constants under constant stress matrices.

In equations (5.1) and (5.2), directions 1 and 2 coincide with the orthotropic directions of the piezoelectric sample, and direction 3 with the direction of the polarization. For PZT material, considered here, the piezoelectric coefficients verify $d_{32} = d_{31}$ and $d_{24} = d_{15}$.

Equations (5.1) and (5.2) can be rewritten in the single matrix form

$$
\left\{ \begin{array}{c} \mathbf{T} \\ \mathbf{D} \end{array} \right\} = \left[\begin{array}{cc} [\mathbf{c^E}] & -[\mathbf{e}]^T \\ [\mathbf{e}] & [\boldsymbol{\varepsilon^S}] \end{array} \right] \left\{ \begin{array}{c} \mathbf{S} \\ \mathbf{E} \end{array} \right\}, \tag{5.3}
$$

or to have a symmetric constitutive law [56]

$$
\left\{ \begin{array}{c} \mathbf{T} \\ \mathbf{D} \end{array} \right\} = \left[\begin{array}{cc} [\mathbf{c^E}] & [\mathbf{e}]^T \\ [\mathbf{e}] & -[\boldsymbol{\varepsilon^S}] \end{array} \right] \left\{ \begin{array}{c} \mathbf{S} \\ -\mathbf{E} \end{array} \right\}. \tag{5.4}
$$

The matrix $[\mathbf{c^E}]$ refers to the stiffness when the electric field is constant. $[\mathbf{e}]$ relates the electric charge per unit area $\{\mathbf{D}\}$ to the strain under a zero electric field (short-circuited electrodes), and is linked to the piezoelectric constants matrix $[\mathbf{d}]$ by

$$
[\mathbf{e}] = [\mathbf{d}]\left[\mathbf{c^E}\right]. \tag{5.5}
$$

$[\boldsymbol{\varepsilon^S}]$ is the permittivity under constant strain matrix and verifies

$$
\left[\boldsymbol{\varepsilon^S}\right] = \left[\boldsymbol{\varepsilon^T}\right] - [\mathbf{e}][\mathbf{d}]^T. \tag{5.6}
$$

The Mindlin's first order plate theory assumptions are summarized here. In addition, piezoelectric hypothesis are given, to obtain the constitutive equations of the piezoelectric Mindlin shell, formulated by Piefort [9].

Plate formulation consists in assuming one dimension, the thickness along $\mathbf{x_3}$, negligible compared with the surface dimensions. Thus $T_{33} = 0$ on the bottom and upper faces, and assumed to be neglected throughout the thickness. Under Mindlin assumptions, a fiber normal to the mid-plane remains straight after deformation but no longer orthogonal

to the mid-plane (see Figure 2.1). The transverse shear strains are assumed to be constant through the thickness. With IEEE Std. notations and by gathering the in-plane and out-of-plane strains, one writes for each layer k

$$
\begin{aligned}
\text{In-plane} \quad \{\mathbf{S}\}_k &= \{\mathbf{S^m}\}_k + z\{\boldsymbol{\kappa}\}_k, \\
\text{Out-of-plane} \quad \{\boldsymbol{\gamma}\}_k &
\end{aligned}
\tag{5.7}
$$

where $\{\mathbf{S^m}\}_k$ is the mid-plane strain of layer k. $\{\mathbf{S^m}\}_k$, $\{\boldsymbol{\kappa}\}_k$ and $\{\boldsymbol{\gamma}\}_k$ are related to the displacement field according to the kinematic model (2.17) (where $\{\boldsymbol{\varepsilon}^m\}_k = \{\mathbf{S^m}\}_k$). In the same way, one notes

$$
\begin{aligned}
\text{In-plane} \quad \{\mathbf{T}\}_k &= \{T_{11} \ T_{22} \ T_{12}\}_k^T, \\
\text{Out-of-plane} \quad \{\boldsymbol{\tau}\}_k &= \{T_{23} \ T_{13}\}_k^T,
\end{aligned}
\tag{5.8}
$$

and the reduced in-plane elastic coefficients set up in-plane stiffness matrix $\left[\mathbf{q_p^E}\right]_k$ (in (2.11) q_{ij} for $i,j = 1,2,6$) and transverse shear elastic coefficients set up transverse shear stiffness matrix $\left[\mathbf{q_t^E}\right]_k$ (in (2.11) q_{ij} for $i,j = 4,5$), see Section 2.2.2 for details on reduced stiffness matrix.

It is assumed that the electric field $\{\mathbf{E}\}$ and displacement $\{\mathbf{D}\}$ are uniform across the thickness of each layer and oriented along the normal direction to the multilayer mesh-plane (direction $\mathbf{x_3}$), one has

$$
\{\mathbf{E}\}_k = \left\{ \begin{array}{c} 0 \\ 0 \\ E_k = -\frac{\phi_k}{h_k} \end{array} \right\}, \quad \{\mathbf{D}\}_k = \left\{ \begin{array}{c} 0 \\ 0 \\ D_k \end{array} \right\},
\tag{5.9}
$$

with ϕ_k the difference of electric potential across the layer and h_k the layer thickness.

Finally, the linear piezoelectricity for each piezoelectric layer k provides that the piezoelectric principal axes are parallel to the structural orthotropy axes and that the poling direction is the direction $\mathbf{x_3}$. And it is assumed that no shear strain is induced by a transverse electric field ($e_{34} = e_{35} = e_{36} = 0$) which is the case for PZT piezoelectric laminate.

By simplification of (5.4), and using the notations introduced above, one obtains the constitutive equations for the piezoelectric layer k

$$
\{\mathbf{T}\}_k = \left[\mathbf{q_p^E}\right]_k \{\mathbf{S}\}_k - \{e_{31} \ e_{32} \ 0\}_k^T E_k,
\tag{5.10}
$$

$$
\{\boldsymbol{\tau}\}_k = \left[\mathbf{q_t^E}\right]_k \{\boldsymbol{\gamma}\}_k,
\tag{5.11}
$$

$$
D_k = \{e_{31} \ e_{32} \ 0\}_k \{\mathbf{S}\}_k + \varepsilon_k E_k.
\tag{5.12}
$$

Notice that, for PZT material, non zero elements of matrix $[\mathbf{e}]$ are e_{31}, e_{32}, e_{33}, e_{24}, e_{15}, and since $E_1 = E_2 = 0$, no shear strain is induced by the transverse electric field, and $-[\mathbf{e}]^T\{\mathbf{E}\} = \{-e_{31} \; -e_{32} \; -e_{33} \; 0 \; 0 \; 0\}^T E_3$.

From the definition of the stress resultants, given in equations (2.18) to (2.20), and by including electro-mechanical coupling, the formulation for piezoelectric plate relates $\{\mathbf{N}\}$, $\{\mathbf{M}\}$, $\{\mathbf{Q}\}$ and $\{\mathbf{D}\}$ to $\{\mathbf{S^m}\}_k$, $\{\boldsymbol{\kappa}\}_k$ and $\{\boldsymbol{\gamma}\}_k$ and $\{\boldsymbol{\phi}\}_k$,

$$
\begin{aligned}
\{\mathbf{N}\} &= \int_z \{\mathbf{T}\}\, dz = \int_z \left[\mathbf{R_T^k}\right]^{-1}_{(1,2,6)} \left[\mathbf{q_p^E}\right]_k \left[\mathbf{R_S^k}\right]_{(1,2,6)} \{\mathbf{S}\}_k - \left[\mathbf{R_T^k}\right]^{-1}_{(1,2,6)} \{e_{31}\; e_{32}\; 0\}^T_k E_k\, dz \\
&= \sum_k \int_{z_{k-1}}^{z_k} \left[\mathbf{R_T^k}\right]^{-1}_{(1,2,6)} \left[\mathbf{q_p^E}\right]_k \left[\mathbf{R_S^k}\right]_{(1,2,6)} \left(\{\mathbf{S^m}\}_k + z\{\boldsymbol{\kappa}\}_k\right)\, dz \\
&\quad - \sum_k \int_{z_{k-1}}^{z_k} \left[\mathbf{R_T^k}\right]^{-1}_{(1,2,6)} \{e_{31}\; e_{32}\; 0\}^T_k E_k\, dz,
\end{aligned}
\tag{5.13}
$$

$$
\begin{aligned}
\{\mathbf{M}\} &= \int_z z\{\mathbf{T}\}\, dz \\
&= \sum_k \int_{z_{k-1}}^{z_k} \left[\mathbf{R_T^k}\right]^{-1}_{(1,2,6)} \left[\mathbf{q_p^E}\right]_k \left[\mathbf{R_S^k}\right]_{(1,2,6)} \left(z\{\mathbf{S^m}\}_k + z^2\{\boldsymbol{\kappa}\}_k\right)\, dz \\
&\quad - \sum_k \int_{z_{k-1}}^{z_k} z\left[\mathbf{R_T^k}\right]^{-1}_{(1,2,6)} \{e_{31}\; e_{32}\; 0\}^T_k E_k\, dz,
\end{aligned}
\tag{5.14}
$$

and

$$
\begin{aligned}
\{\mathbf{Q}\} &= \int_z \{\boldsymbol{\tau}\}\, dz \\
&= \sum_k \int_{z_{k-1}}^{z_k} \left[\mathbf{R_T^k}\right]^{-1}_{(4,5)} \left[\mathbf{q_t^E}\right]_k \left[\mathbf{R_S^k}\right]_{(4,5)} \{\boldsymbol{\gamma}\}_k\, dz.
\end{aligned}
\tag{5.15}
$$

$$
\begin{aligned}
D_k &= \{e_{31}\; e_{32}\; 0\}_k \left[\mathbf{R_S^k}\right]_{(1,2,6)} \{\mathbf{S}\}_k + \varepsilon_k E_k \\
&= \{e_{31}\; e_{32}\; 0\}_k \left[\mathbf{R_S^k}\right]_{(1,2,6)} \left(\{\mathbf{S^m}\}_k + z_{mk}\{\boldsymbol{\kappa}\}_k\right) + \varepsilon_k E_k
\end{aligned}
\tag{5.16}
$$

Note that $\displaystyle\int_{z_{k-1}}^{z_k} \frac{z}{h_k}\, dz = \frac{z_{k-1}+z_k}{2} = z_{mk}$.

$\left[\mathbf{R_T^k}\right]$ (see (2.32)) and $\left[\mathbf{R_S^k}\right]$ (see (2.33)) are the rotation matrices, associated to the angle θ_k, relating the stress and strain in any structural basis to the stress and strain in the piezoelectric material principal basis,

$$
\left[\mathbf{R_T^k}\right] = \left[\begin{array}{c|c} \left[\mathbf{R_T^k}\right]_{(1,2,6)} & [\mathbf{0}] \\ \hline [\mathbf{0}] & \left[\mathbf{R_T^k}\right]_{(4,5)} \end{array}\right], \quad \left[\mathbf{R_S^k}\right] = \left[\begin{array}{c|c} \left[\mathbf{R_S^k}\right]_{(1,2,6)} & [\mathbf{0}] \\ \hline [\mathbf{0}] & \left[\mathbf{R_S^k}\right]_{(4,5)} \end{array}\right]
\tag{5.17}
$$

One has $\left[\mathbf{R_T^k}\right]^{-1} = \left[\mathbf{R_S^k}\right]^T$, thus $\left[\mathbf{R_T^k}\right]^{-1}_{(1,2,6)} \{e_{31}\ e_{32}\ 0\}^T_k = (\{e_{31}\ e_{32}\ 0\}_k \left[\mathbf{R_S^k}\right]_{(1,2,6)})^T$. And $\{e_{31}\ e_{32}\ 0\}_k \left[\mathbf{R_S^k}\right]_{(1,2,6)}$ will be written $\{\mathbf{G_k}\}$. One recalls

$$\left[\mathbf{R_S^k}\right]_{(1,2,6)} = \begin{bmatrix} cos^2\theta_k & sin^2\theta_k & sin\theta_k cos\theta_k \\ sin^2\theta_k & cos^2\theta_k & -sin\theta_k cos\theta_k \\ -2sin\theta_k cos\theta_k & 2sin\theta_k cos\theta_k & cos^2\theta_k - sin^2\theta_k \end{bmatrix}, \qquad (5.18)$$

In a compact form, Mindlin piezoelectric plate formulation is

$$\left\{ \begin{array}{c} \mathbf{N} \\ \mathbf{M} \\ \mathbf{Q} \\ \vdots \\ D_k \\ \vdots \end{array} \right\} = \left[\begin{array}{ccc|ccc} \mathbf{A} & \mathbf{B} & \mathbf{0} & \cdots & h_k\{\mathbf{G_k}\}^T & \cdots \\ \mathbf{B} & \mathbf{D} & \mathbf{0} & \cdots & z_{mk}h_k\{\mathbf{G_k}\}^T & \cdots \\ \mathbf{0} & \mathbf{0} & \mathbf{F} & \cdots & [\mathbf{0}] & \cdots \\ \hline \vdots & \vdots & \vdots & \ddots & 0 & \\ \mathbf{G_k} & z_{mk}\mathbf{G_k} & \mathbf{0} & & -\varepsilon_k & \\ \vdots & \vdots & \vdots & 0 & & \ddots \end{array} \right] \left\{ \begin{array}{c} \mathbf{S^m} \\ \mathbf{\kappa} \\ \mathbf{\gamma} \\ \vdots \\ -E_k \\ \vdots \end{array} \right\}. \qquad (5.19)$$

If needed it is possbile to use the matrix $[\mathbf{H}] = \frac{5}{6}[\mathbf{F}]$ instead of $[\mathbf{F}]$, where $\frac{5}{6}$ is a shear correction factor, to improve the model of the shear effect. The matrices $[\mathbf{A}],[\mathbf{B}],[\mathbf{D}]$, $[\mathbf{F}]$ are respectively the extensional stiffness, the extension/bending coupling, the bending stiffness and the transverse shear stiffness matrices, classical stiffness matrices for a composite laminate given by (2.40) to (2.42).

5.2.2   Finite element formulation of a piezoelectric plate

Given the constitutive law (5.19), the principle of virtual work can be simply used to extend a classical shell element to include one additional electric DOF, ϕ_k, per piezoelectric layer which is assumed constant over the element, and in SDT is common to all elements covered by an electrode (the potential is associated with a single electric DOF for all elements of a given property).

The displacement field at any integration point, identified by coordinates (r,s) in the reference element is related to displacement at nodes by the means of shape functions

$$\{\mathbf{u}(r,s)\} = \left[\mathcal{N}_u(r,s)\right]\{\mathbf{q_i}\}, \qquad (5.20)$$

The strain vector and the electric field can then be related to the nodal displacements and potential by the shape functions derivatives $[\mathcal{B}_\mathbf{u}]$ and division by thickness for the

electric displacement $[\boldsymbol{\mathcal{B}}_\phi]$

$$\begin{bmatrix} \mathbf{S^m}(r,s) \\ \boldsymbol{\kappa}(r,s) \\ \boldsymbol{\gamma}(r,s) \\ -\mathbf{E_k} \end{bmatrix} = \begin{bmatrix} \boldsymbol{\mathcal{B}}_u(r,s) & \mathbf{0} \\ \mathbf{0} & \boldsymbol{\mathcal{B}}_\phi \end{bmatrix} \begin{Bmatrix} \mathbf{q_i} \\ \boldsymbol{\phi_k} \end{Bmatrix}, \tag{5.21}$$

or giving all the components

$$\begin{Bmatrix} S^m_{xx} \\ S^m_{yy} \\ \gamma^m_{xy} \\ \kappa_{xx} \\ \kappa_{yy} \\ \kappa_{xy} \\ \gamma_{xz} \\ \gamma_{yz} \\ \vdots \\ -E_k \\ \vdots \end{Bmatrix} = \begin{bmatrix} \mathcal{N}_{,x} & 0 & 0 & 0 & 0 \\ 0 & \mathcal{N}_{,y} & 0 & 0 & 0 \\ \mathcal{N}_{,y} & \mathcal{N}_{,x} & 0 & 0 & 0 \\ 0 & 0 & 0 & 0 & \mathcal{N}_{,x} \\ 0 & 0 & 0 & -\mathcal{N}_{,y} & 0 & & 0 \\ 0 & 0 & 0 & -\mathcal{N}_{,x} & \mathcal{N}_{,y} \\ 0 & 0 & \mathcal{N}_{,x} & 0 & \mathcal{N} \\ 0 & 0 & \mathcal{N}_{,y} & -\mathcal{N} & 0 \\ \hline & & & & & \ddots & 0 \\ & & 0 & & & \frac{1}{h_k} \\ & & & & & 0 & \ddots \end{bmatrix} \begin{Bmatrix} u_x \\ u_y \\ w \\ \theta_x \\ \theta_y \\ \vdots \\ \phi_k \\ \vdots \end{Bmatrix} \tag{5.22}$$

where $\mathcal{N}_{,x}$, $\mathcal{N}_{,y}$ are the derivative of the shape functions with respect to cartesian coordinates at the current integration point and $\{\mathbf{q_i}\}$ are the DOFs at element nodes.

For each element the element formulation is obtained by integrating over the element the work of generalized strains (5.22) for generalized stresses (5.19). The result takes the form

$$\begin{aligned} [\mathbf{M_{uu}}]_e\{\ddot{\mathbf{q}}_{\mathbf{i}}\} + [\mathbf{K_{uu}}]_e\{\mathbf{q_i}\} + [\mathbf{K_{u\phi}}]_e\{\boldsymbol{\phi_i}\} &= \{\mathbf{F_{mech}}\}_e \\ [\mathbf{K_{\phi u}}]_e\{\mathbf{q_i}\} + [\mathbf{K_{\phi\phi}}]_e\{\boldsymbol{\phi_i}\} &= \{\mathbf{Q_k}\}_e \end{aligned} \tag{5.23}$$

with $[\mathbf{M_{uu}}]_e$ the element mass (electro-statics are assumed so there is no mass for electric terms),

$$[\mathbf{M_{uu}}]_e = \int_{V_e} \rho \, [\boldsymbol{\mathcal{N}_u}]^T [\boldsymbol{\mathcal{N}_u}] dV_e, \tag{5.24}$$

$[\mathbf{K_{uu}}]_e$ the mechanical stiffness matrix,

$$[\mathbf{K_{uu}}]_e = \int_{V_e} [\boldsymbol{\mathcal{B}_u}]^T [\mathbf{c^E}] [\boldsymbol{\mathcal{B}_u}] dV_e, \tag{5.25}$$

$[\mathbf{K_{u\phi}}]_e$ the piezoelectric coupling matrix,

$$[\mathbf{K_{u\phi}}]_e = [\mathbf{K_{\phi u}}]_e^T = \int_{V_e} [\boldsymbol{\mathcal{B}_u}]^T [\mathbf{e}]^T [\boldsymbol{\mathcal{B}_\phi}] dV_e, \tag{5.26}$$

and $\left[\mathbf{K}_{\phi\phi}\right]_e$ the capacitance matrix,

$$\left[\mathbf{K}_{\phi\phi}\right]_e = -\int\limits_{V_e} \left[\boldsymbol{\mathcal{B}}_{\phi}\right]^T \left[\boldsymbol{\varepsilon}^{\mathbf{S}}\right] \left[\boldsymbol{\mathcal{B}}_{\phi}\right] dV_e. \tag{5.27}$$

For Mindlin piezoelectric plate, the matrices $[\mathbf{K}_{\mathbf{uu}}]_e$, $\left[\mathbf{K}_{\mathbf{u}\phi}\right]_e$ and $\left[\mathbf{K}_{\phi\phi}\right]$ take the following forms

$$[\mathbf{K}_{\mathbf{uu}}]_e = \int\limits_{S_e} [\boldsymbol{\mathcal{B}}_{\mathbf{u}}]^T \begin{bmatrix} \mathbf{A} & \mathbf{B} & \mathbf{0} \\ \mathbf{B} & \mathbf{D} & \mathbf{0} \\ \mathbf{0} & \mathbf{0} & \mathbf{F} \end{bmatrix} [\boldsymbol{\mathcal{B}}_{\mathbf{u}}] dS_e \tag{5.28}$$

$$\left[\mathbf{K}_{\mathbf{u}\phi}\right]_e = \left[\mathbf{K}_{\phi\mathbf{u}}\right]_e^T = \int\limits_{S_e} [\boldsymbol{\mathcal{B}}]^T \begin{bmatrix} \cdots & \{\mathbf{G_k}\}^T & \cdots \\ \cdots & z_{mk}\{\mathbf{G_k}\}^T & \cdots \\ \cdots & \mathbf{0} & \cdots \end{bmatrix} dS_e \tag{5.29}$$

$$\left[\mathbf{K}_{\phi\phi}\right]_e = -S_e \begin{bmatrix} \ddots & & 0 \\ & \varepsilon_k/h_k & \\ 0 & & \ddots \end{bmatrix} \tag{5.30}$$

with $\{\mathbf{G_k}\} = \{e_{31}\ e_{32}\ 0\}_k \left[\mathbf{R_S^k}\right]_{(1,2,6)}$ and S_e the element area.
or giving all the components

$\{\mathbf{F_{mech}}\}_e$ is the external mechanical force,

$$\{\mathbf{F_{mech}}\}_e = \int\limits_{S_e} [\boldsymbol{\mathcal{N}_{\mathbf{u}}}]^T \{\mathbf{P_S}\} dS_e + [\boldsymbol{\mathcal{N}_{\mathbf{u}}}]^T \{\mathbf{P_C}\}. \tag{5.31}$$

If the software implementation considers potentials ϕ_k that are constant over electrodes, and thus common to multiple elements, Q_k corresponds to the total charge on the electrode and is equal to the integral of the electric displacement over the electrode area,

$$Q_k = \int\limits_{S_e} D_k dS_e \tag{5.32}$$

The non uniformity of the charge under an electrode will be illustrated later (see Section 5.3.4, Figures 5.16 to 5.18).

5.2.3   Resolution

Once assembled the model takes the form

$$\begin{bmatrix} \mathbf{Z_{uu}} & \mathbf{K_{u\phi}} \\ \mathbf{K_{\phi u}} & \mathbf{K_{\phi\phi}} \end{bmatrix} \left\{ \begin{array}{c} \mathbf{q_{mech}} \\ \boldsymbol{\phi_k} \end{array} \right\} = \left\{ \begin{array}{c} \mathbf{F_{mech}} \\ \mathbf{Q_k} \end{array} \right\} \tag{5.33}$$

with the classical dynamic stiffness $[\mathbf{Z}] = [\mathbf{M}]s^2 + [\mathbf{K}]$.

When simulating the response, one needs to consider sensor and actuator configurations.

Piezoelectric patches used as sensors have a charge that remains zero (open circuit mode). One can thus condense the electric DOF. Indeed, one considers an electrostatic behavior (no $M_{\phi\phi}$ or $M_{\phi u}$) and assumes $Q_k = 0$, one thus has

$$\left\{ \begin{array}{c} \mathbf{q_{mech}} \\ \boldsymbol{\phi_k} \end{array} \right\} = \begin{bmatrix} \mathbf{I} \\ -\left[\mathbf{K_{\phi\phi}} \right]^{-1} \left[\mathbf{K_{\phi u}} \right] \end{bmatrix} \{ \mathbf{q_{mech}} \} = [\mathbf{T}] \{ \mathbf{q_{mech}} \} \tag{5.34}$$

This relation can be used to eliminate the electric contribution from the system equations which become

$$[\mathbf{T}]^T [\mathbf{Z}][\mathbf{T}] \{ \mathbf{q_{mech}} \} = [\mathbf{T}]^T \{ \mathbf{F} \} \tag{5.35}$$

From this condensation it clearly appears that a patched used as sensor induces a shift of frequencies from a configuration without piezoelectric coupling.

Piezolectric patches used as actuators have a difference of potential ϕ_k that is enforced. One can thus use the electric part of (5.33) to determine the charge

$$\{ \mathbf{Q_k} \} = \begin{bmatrix} \mathbf{K_{\phi u}} & \mathbf{K_{\phi\phi}} \end{bmatrix} \left\{ \begin{array}{c} \mathbf{q_{mech}} \\ \boldsymbol{\phi_k} \end{array} \right\} \tag{5.36}$$

and consider the system equations with no piezoelectric coupling and an electric load

$$[\mathbf{Z_{uu}}] \{ \mathbf{q_{mech}} \} = \{ \mathbf{F_{mech}} \} - \begin{bmatrix} \mathbf{K_{u\phi}} \end{bmatrix} \{ \boldsymbol{\phi_k} \} \tag{5.37}$$

It clearly appears that the dynamic stiffness of this configuration, is that of the purely mechanical model with no piezoelectric coupling. The modes of $[\mathbf{Z_{uu}}]$ correspond to the case with ϕ_k set to zero. In other words, the actuator configuration leads to closed circuit modes.

In the resolution process implemented in [34], electrodes are declared to be either open or closed circuit which allows a condensation or elimination of electrical DOFs before computation of modes and static correction for inputs which are used to build the state-space model.

5.3   Validation on the honeycomb beam actuated by piezoelectric patch

In this section, the FE model of honeycomb beam CN20L with piezoelectric patches QuickPack Midé QP20W, implemented in MATLAB/SDT is compared with tests.

The test case and the setup are first presented in sections 5.3.1 and 5.3.2.

A test/analysis correlation has been made, and the modal behavior of the beam is compared, considering or not the viscoelastic law of the honeycomb core (Section 5.3.3).

A specification of the QuickPack Midé QP20W is that it is made of a stack of two piezoelectric layers. It is thus possible to plug the electrodes to favor membrane or bending behavior of the patch depending on the effect expected on the structure actuated. The Section 5.3.4 focuses on the validation of the FE model, with respect to tests, for the specific membrane or bending actuator of the patch QP20W.

5.3.1   Test case characteristics

The beam tested in this chapter is the CN20L Carbon/Nomex honeycomb sandwich beam, 900mm long, 45mm large and 22mm thick, equipped with 3 piezoelectric patches Quick-Pack Midé QP20W. This beam have been previously tested without patch, the results of the estimation of the equivalent core parameters as a function of frequency are given in Chapter 4. The beam properties are recalled in Table 5.2, the piezoelectric patch ones are given in Table 5.3.

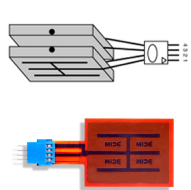**Table 5.2:** *Definition of Carbon/Nomex composite properties*

	Geometric Parameters		Material Parameters		
Carbon face sheet	h_f	1	ρ_f	1.6	$E_{f_{ref}}$ 45
Nomex Honeycomb	h_h, t a, b, θ	20, 7.62 10^{-2} 2.75, 2.75, $\frac{\pi}{6}$	ρ_h	1.38	$E_{h_{ref}}$ 3
Epoxy glue	h_g, t_g	0.3, 0.1	ρ_g	1	E_g 2

Length in mm, angle in rad, density in $10^3 kg/m^3$, elastic moduli in GPa

Piezoelectric patches used for experiments on the Carbon/Nomex honeycomb beam are Midé [53] QuickPack Actuators QP20W, whose specifications are given in Table 5.3. It is a strain-type actuator that consists of two piezoelectric layers encapsulated in a film. For standard QuickPack strain actuators, the material is industry type PZT-5A, its properties are given in Table 5.4.

Table 5.3: *Midé QuickPack QP20W properties*

Specifications			
Device size	2.00×1.50×0.03 (in)	50.8×38.1×0.76 (mm)	
Device weight	0.28 (oz)	7.94 (g)	
Active elements	1 stack of 2 piezos		
Piezo wafer size	1.81×1.31×0.01 (in)	46.0×33.3×0.25 (mm)	
Device capacitance	0.20 (μF)		
Full scale voltage range	±200 (V)		

Table 5.4: *Piezoelectric material Properties*

Property	Symbol	Units	Value
Density	ρ	kg/m^3	7700
Dielectric Constant	$\varepsilon^T/\varepsilon_0 \; \varepsilon_0 = 8.85 \times 10^{-12}$	F/m	1800
Coupling Coefficients	k_p		0.63
	k_{33}		0.70
	k_{31}		0.30
	k_t		0.40
Piezoelectric Charge Coefficients (Displacement Coeff)	d_{33}	$C/N * 10^{-12}$	350
	$d_{31}=d_{32}$*	$m/V * 10^{-12}$	-179
	d_{15}	*not given by Midé, reference value [10]: 500*	
Piezoelectric Voltage Coefficients (Voltage Coeff)	g_{33}	$V.m/N * 10^{-3}$	24.2
	g_{31}		-11.0
Elastic Moduli	c_{11}^E	$N/m^2 * 10^{10}$	6.9
	c_{33}^E		5.5

* the poling direction is $\mathbf{x_3}$ and PZT is supposed to be isotropic in-plane $(\mathbf{x_1}, \mathbf{x_2})$

By default, the QuickPack Midé QP20W, with two piezoelectric layers, has 4 electrodes not connected with each other. The connection is determined and made by users. Associated issues will be discussed in Section 5.3.4.

5.3.2 Experimental Setup

To validate the piezoelectric plate model and its integration on the full honeycomb SVS model, the beam was tested in free-free conditions up to 2 kHz. Three piezoelectric patches were bonded on the beam as shown in Figure 5.1. Piezo 1 and Piezo 2 were bonded on one side at two different locations, Piezo 3 on the other side of the beam, just below piezo 1, in a configuration classically thought to lead to a collocated input/output pair.
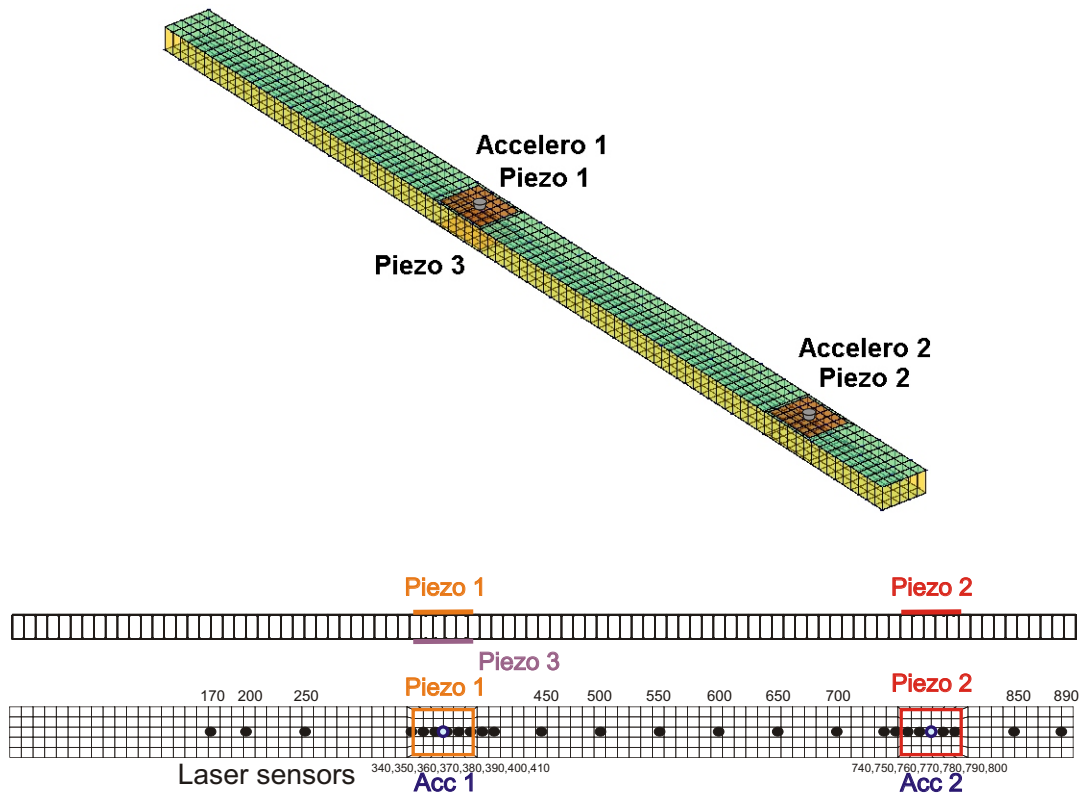

Figure 5.1: *Test beam with piezoelectric patches*

Two experimental modal tests were conducted on the beam. The first one, performed at the Marcus Wallenberg Laboratory for Sound and Vibration Research (MWL) of KTH Stockholm University, focused on the overall modal behavior of the beam. The results are discussed in Sections 5.3.3 and 5.4.1. Inputs considered were piezoelectric actuator, shaker and hammer. Two accelerometers were available to measure the z-acceleration at the Piezo 1 and Piezo 2 positions. Additionally, a laser vibrometer (from Polytech) was used to measure the z-velocity of the beam in 26 points centered on the beam upper side and shown in Figure 5.1. Membrane and bending actuation were considered to cross-check the validity of the setup (Section 5.3.4).

Exploitation of this test eventually motivated a second one focusing on the local mechanical deformation under the patches, see Section 5.4.2. The second test was per-

formed at MSSMat laboratory of Ecole Centrale of Paris. The overall setups are illustrated in figure 5.2. A voltage amplifier (from Treck) was used to drive the piezoelectric patches which were connected in parallel to favor membrane actuation (see discussion in Section 5.3.4).
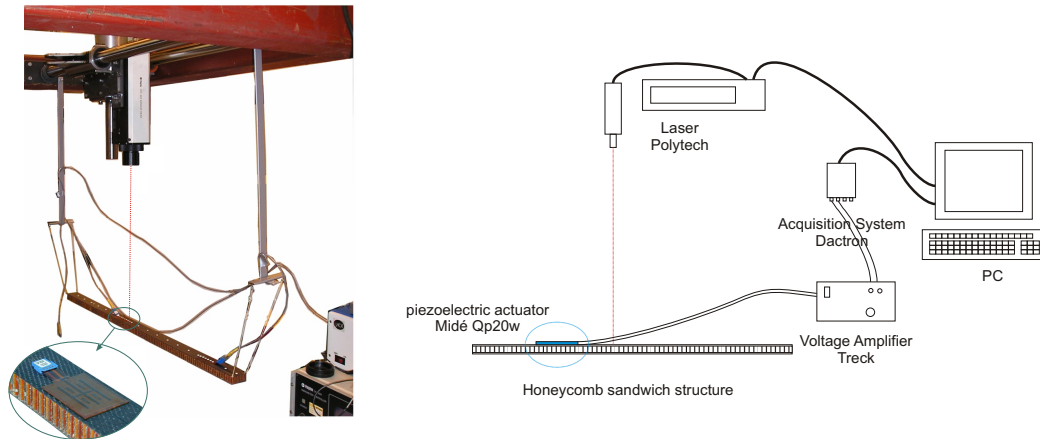

Figure 5.2: *Experimental Setup. Left : picture of setup used at KTH. Right : functional representation of setup (for tests at KTH and ECP)*

Test analysis correlation initially showed significant phase errors. Significant energy was thus spent diagnosing the problem which was eventually associated with the voltage amplifier. As shown in Figure 5.3, the overall transfer of the test has the vibration transfer in series with an amplifier at the input and a velocimeter filter at the output. Figure 5.4 shows the initial measurement, the measured amplifier transfer and the corrected structural transfer which is the one that should be correlated with the model.
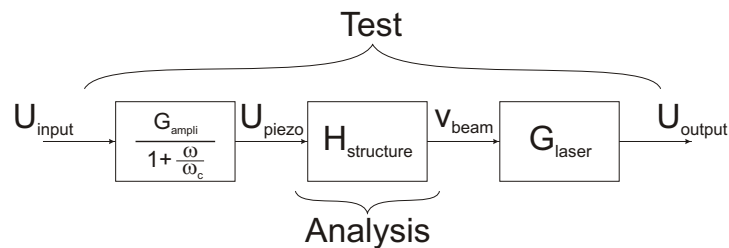
Figure 5.3: *Functional representation of the measurement loop*

Modeling of a viscoelastic honeycomb panel equipped with piezoelectric patches in view of vibroacoustic active control design
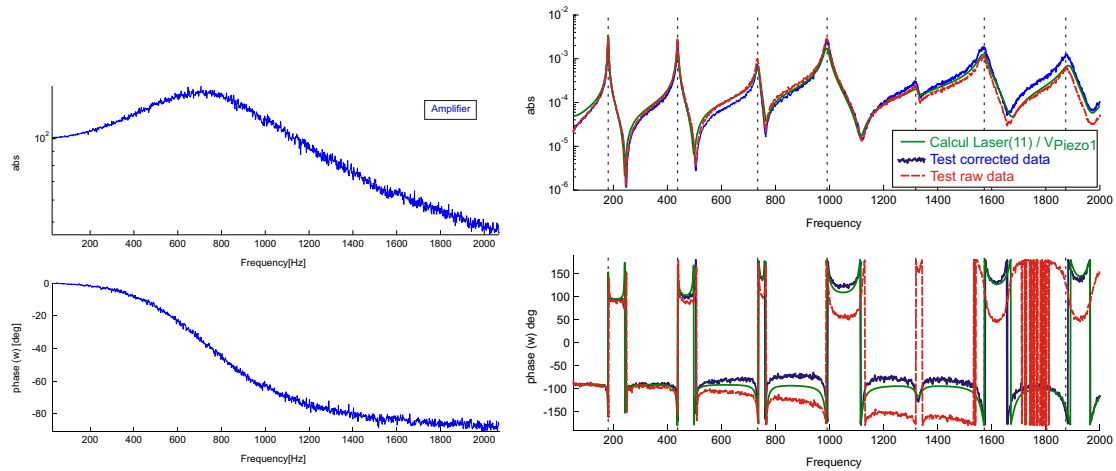
Figure 5.4: *Frequency Response Functions amplifier transfer, structure transfer compared with model transfer and raw measured transfer, (velocity/piezo voltage)*

The account for lowpass filter of the voltage amplifier allows to have a model transfer in good agreement with the corrected measured structure transfer.

5.3.3 Correlation of modal properties

Finite element model presented in Section 5.2 has been implemented in MATLAB/SDT. One recalls that for piezoelectric shell a single electric degree of freedom (DOF) is considered for each difference of potential through the thickness of each piezoelectric layer. And this DOF is thus common for all elements covered by a given electrode. This differs notably from the strategy used in piezoelectric volume elements, where the electric potential is defined at physical nodes and electrodes are defined as constraints: one grounded electrode and an equipotentiality constraint for the other. In the QP20W application, each patch has two piezoelectric layers and is thus associated with two electric DOFs.

For the implementation, the first strategy for the integration of the piezoelectric component in honeycomb beam model is an adaptation of the mesh to conform to the patch limits. One assumes the behavior of the elements covered by the piezoelectric material, shown in grey on Figure 5.5, to be that of a single shell with three layers, the skin and the piezoelectric layers. Laminated shell properties are computed using formulas described earlier. The influence of glue, which is sometimes important was neglected here due to a very low thickness (estimated at 0.03 mm). An electric DOF is also affected to each piezoelectric layer of the element.

The material properties for piezolectric layers are elastic properties (E, G, ν, ρ) and piezoelectric constants d and dielectric constants ε.
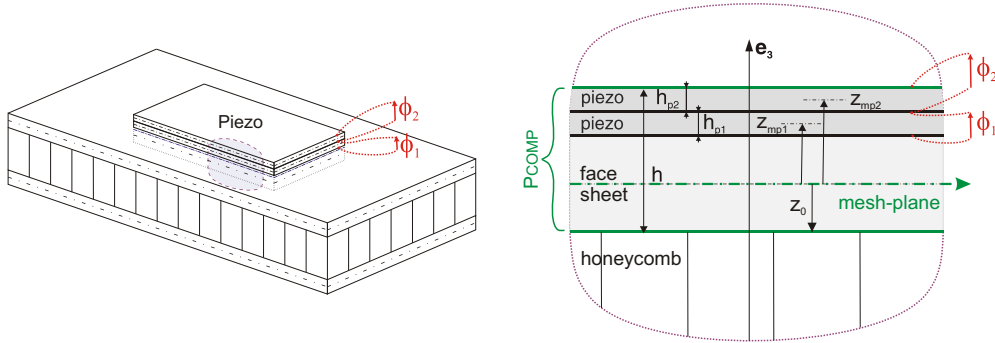
Figure 5.5: *Modeling of sandwich beam with piezoelectric layers*

The modal test/analysis correlation is performed from the first test made at KTH Universtiy. The significant spatial resolution was meant to allow simple test/analysis correlation. The results shown in Figure 5.6 and Table 5.5 indicate a very good correlation in shaped, but errors in frequency that have a global trend. As shown in Section 4.3, Nomex based honeycomb and/or glue have a viscoelastic behavior which causes the error on modal frequencies seen here.
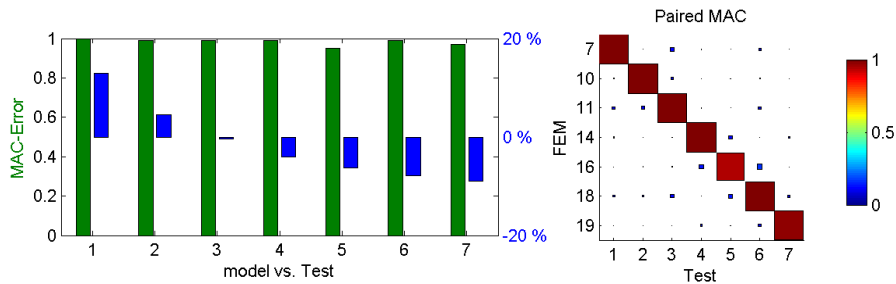
Figure 5.6: *Test/Analysis correlation on Carbon/Nomex (CN20L) beam without parameter frequency dependence*

Table 5.5: *Test/Analysis correlation on CN20L beam without frequency dependence*

Test		Model		$\Delta F/F$	MAC
n	f(Hz)	n	f(Hz)	%	
1	180.4	7	203.7	12.9	100
2	439.4	10	459.2	4.5	99
3	735.7	11	732.4	-0.4	99
4	994.4	14	954.4	-4.0	99
5	1330.1	16	1245.9	-6.3	95
6	1576.9	18	1454.3	-7.8	99
7	1893.5	19	1725.1	-8.9	97

Figure 5.8 clearly illustrates that once the correct viscoelastic behavior is used, given on Figure 5.7, frequency errors are quite small. Table 5.6 shows mode frequencies and shapes of the Carbon/Nomex beam actuated by the patch Piezo 1, measured with laser vibrometer, accounting for frequency dependence of the core properties. Modes are well correlated, MAC is higher than 95% for the 7 first bending modes, and the frequency error is lower than 1.4 %.
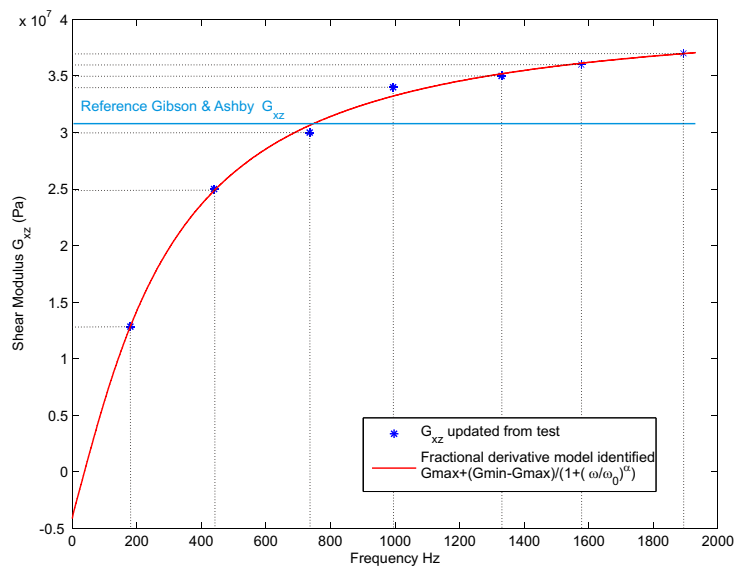

Figure 5.7: *Viscoelastic law $G_{xz}^{\star}(f)$ of Nomex core including the glue updated from test*
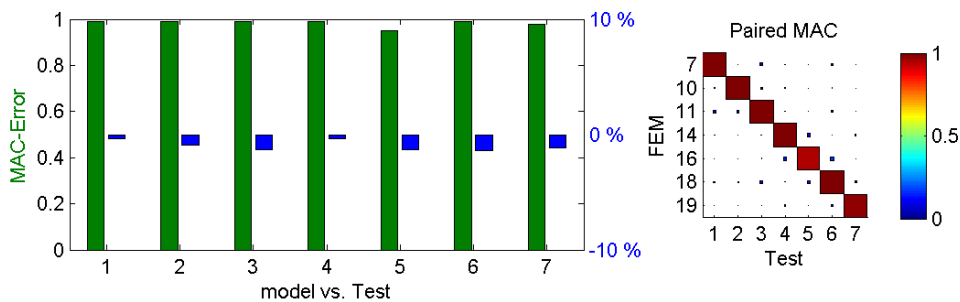
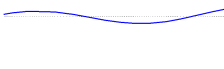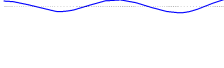**Figure 5.8:** *Test/Analysis correlation on Carbon/Nomex beam with frequency dependence of $G_{xz}^{\star}$*

Table 5.6: *Test analysis correlation on Carbon/Nomex beam*

Test				Model			ΔF/F	MAC
mode	f (Hz)	ζ	shape	mode	f (Hz)	shape		
1	180.4	0.015		7	179.7		-0.4	99
2	439.4	0.0088		10	435.5		-0.9	99
3	735.7	0.0069		11	726.3		-1.3	99
4	994.4	0.0087		14	990.7		-0.4	99
5	1330.1	0.010		16	1312.8		-1.3	95
6	1576.9	0.010		18	1554.5		-1.4	99
7	1893.5	0.014		19	1871.3		-1.2	98

The viscoelastic law $G_{xz}^{\star}(f)$ has been used to obtain frequency transfer that accounts for the frequency dependence. Figure 5.9 shows the transfers obtained by taking into account the frequency dependence (red dash curve), which is very similar to the test transfer (blue solid curve). Whereas with a constant shear modulus $G_{xz}^{\star}$, simulated resonances are shifted compared to test ones (green dash-dot curve).

Overall, the modal behavior is very well represented by the finite element model which is clearly validated. The experiments however showed that out of resonance, the dynamic behavior of the beam includes very local effects that were not reported elsewhere. These local effects will be analyzed in much more detail in Section 5.4.
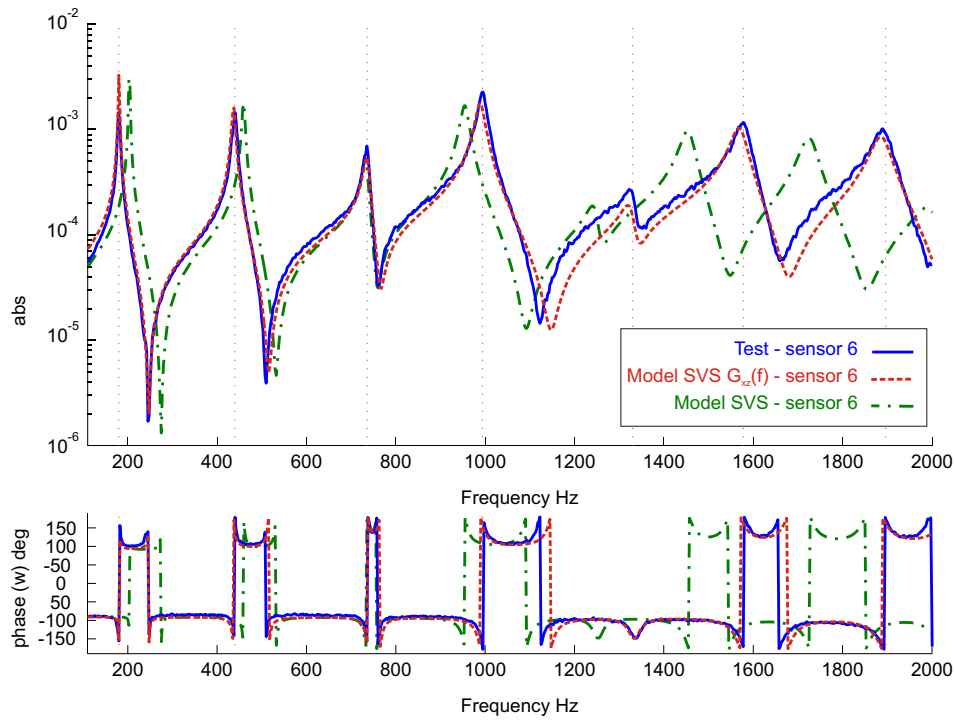
Figure 5.9: *Test/Analysis Frequency Response Functions of a Carbon/Nomex honeycomb beam - Piezo 1 actuator - Laser sensor 6*

5.3.4   Membrane and bending actuation

To analyze the local effects in Section 5.4, it is important to understand how the patch actuation works. When a voltage is applied, a patch polarized in the x_3 direction stretches in its plane (x_1, x_2). Due to the offset of the patch from the mid-plane of the shell, this membrane load induces moments and membrane loads that are located at the edge of the patch. On classical beam models [57, 10, 9], one represents two loads at the edges. For surface models considered here one really has a distribution of bending moment and in-plane load along the edge of the patch, as represented on Figure 5.10.

Figure 5.10: *Moments and membrane loads induced at the edge of the patch*

Modeling of a viscoelastic honeycomb panel equipped with piezoelectric patches in view of vibroacoustic active control design

For the QuickPack QP20W, the two piezoelectric layers (electrodes) can be connected in parallel or in series depending on the voltage delivered by the amplifier. One can also use equal potential on both ele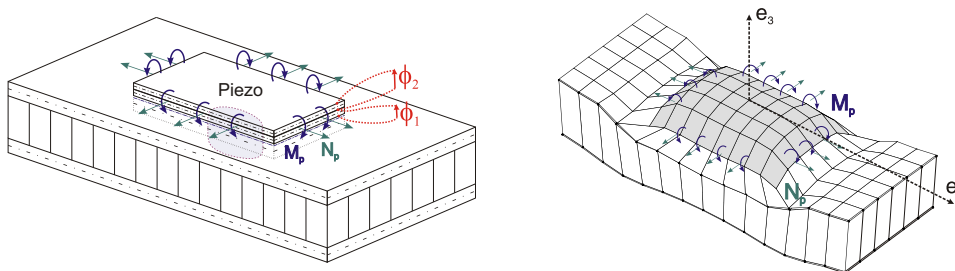ctrodes to favor membrane actuation and opposite potential to favor bending. If the electrodes are connected in phase, the moments induced on the edges of each layer tend to compensate for each other and the overall effect is a membrane actuator. Connected in phase opposition, the moments on the edges add up and generate a more efficient bending actuator. The Figure 5.11 sums up the possible cabling of the two electrodes of the QuickPack QP20W patch.
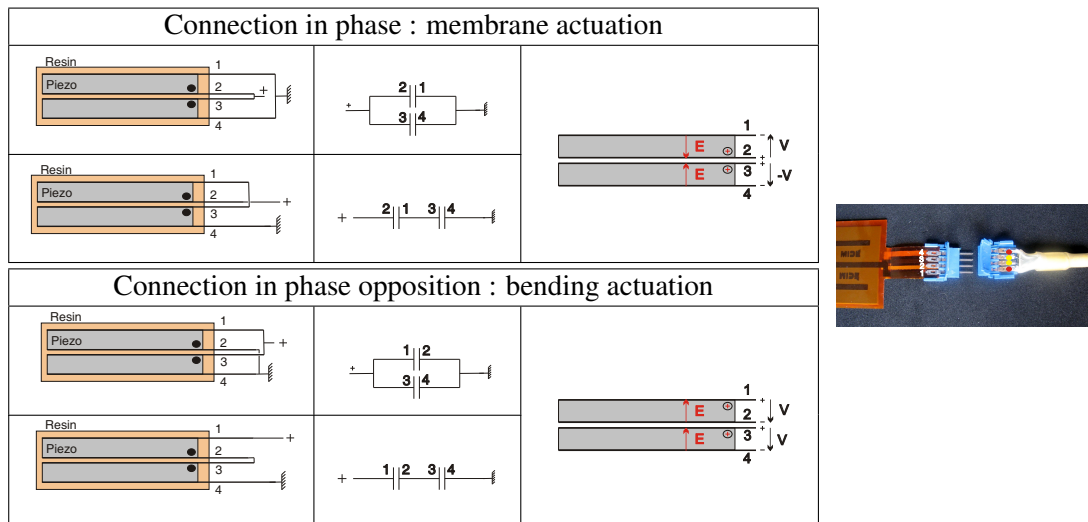
Figure 5.11: *Electrodes connection - side view and circuits - top view*

To verify the setup and illustrate the local effects, tests in both configurations were performed. Figures 5.12 and 5.13 illustrate the transfer between Piezo 1 to laser output with both cabling configurations. Test and analysis are also superposed in the second figure to confirm the quality of the model. Cabling 1 (membrane actuation) is clearly much better in the present case with much higher induced vibration and bigger distance between pole and zero.
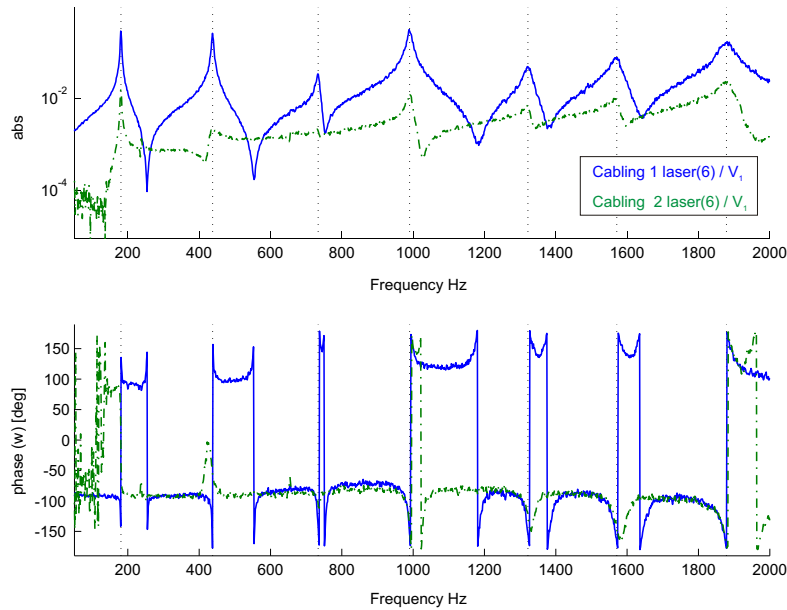
Figure 5.12: *Frequency Response Functions between actuator Piezo 1 and laser sensor 6 - cabling 1 and cabling 2*
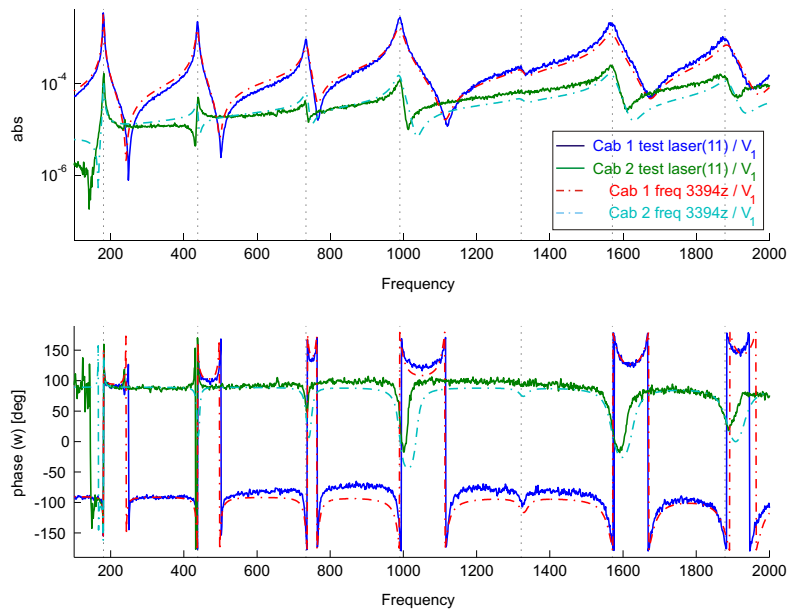
Figure 5.13: *Compared test/analysis FRF between actuator Piezo 1 and z-velocity of node 3394 (center of the patch) - cabling 1 and cabling 2*

To further illustrate the higher efficiency of cabling 1, the impedance $\frac{Q_{Piezo1}}{V_{Piezo1}}$ of piezo-electric patch 1 was computed and is shown in Figure 5.14. The efficiency of a piezoelectric actuator is directly proportional to the distance between pole and zero. For widely

separated poles and zeros, the phase excursion would be 180°. For cabling 2 (bending actuation with 2 electrodes of the patch in phase opposition), the first 3 modes show a maximum phase below 1°. The potential of the actuator is thus extremely small. This confirms that cabling 2 is not appropriate to control the considered beam. Cabling 1 (membrane actuation) has a significantly higher potential but the maximum phase remains quite small.
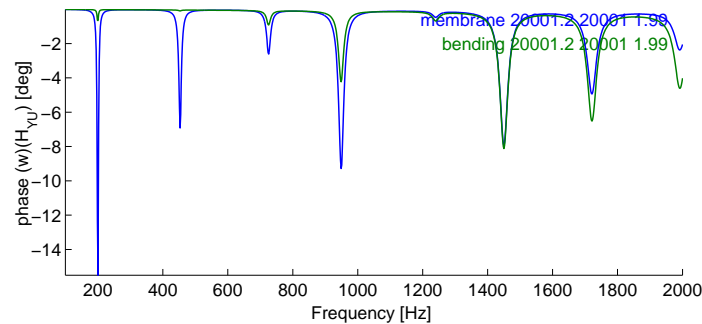
Figure 5.14: *Phase of impedance (transfer from tension to charge) at Piezo 1 - Cabling 1 (membrane) and Cabling 2 (bending)*

To gain further understanding, one computed the quasi-static response for an actuation at 10 Hz. Figures 5.15 and 5.16 display the mechanical z-displacement and charge distribution in the actuator elements. The charge is displayed at the 4 integration points of each element, which do not correspond to nodes, so that no mesh is shown.


Figure 5.15: *Quasi-static response at 10 Hz for bending and membrane actuation. Mechanical displacement. Color proportional to vertical displacement.*

The mechanical displacement clearly shows that skin bending actuation induces almost no global bending at this frequency. Membrane actuation induces overall bending but also a very significant local bending below the patch. This effect is critical for the poor performance of piezoelectric actuators in the present case and will be analyzed in more detail in the next section.

The charge distributions the two electrode of the patch used as actuator, shown in Figure 5.16, give useful information on how the patch really behaves. The charge distribution is very far from being uniform. The top electrode Q2 shows the most variations, as expected since it is located further away from the neutral axis. In membrane actuation, the mean charge is significantly higher, and the difference between minimum and maximum charge smaller than in bending actuation. This is consistent with a higher efficiency of the membrane actuation with 2 electrodes of the patch in phase.
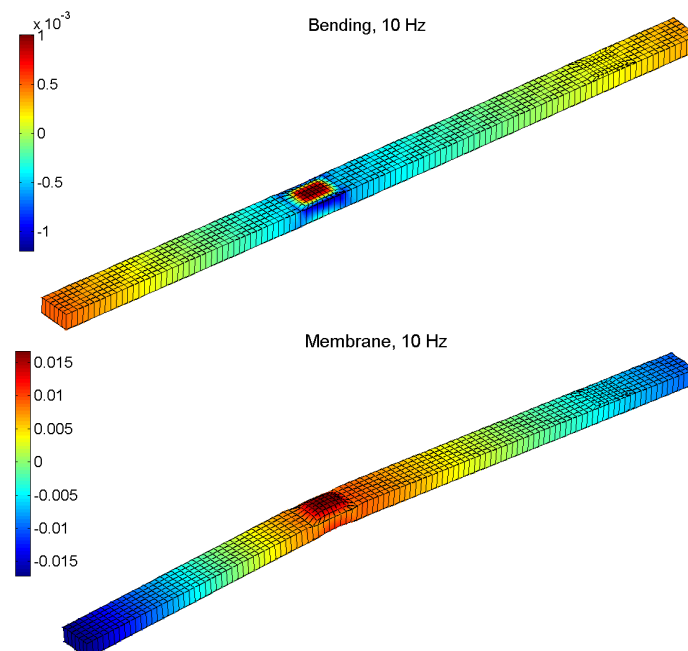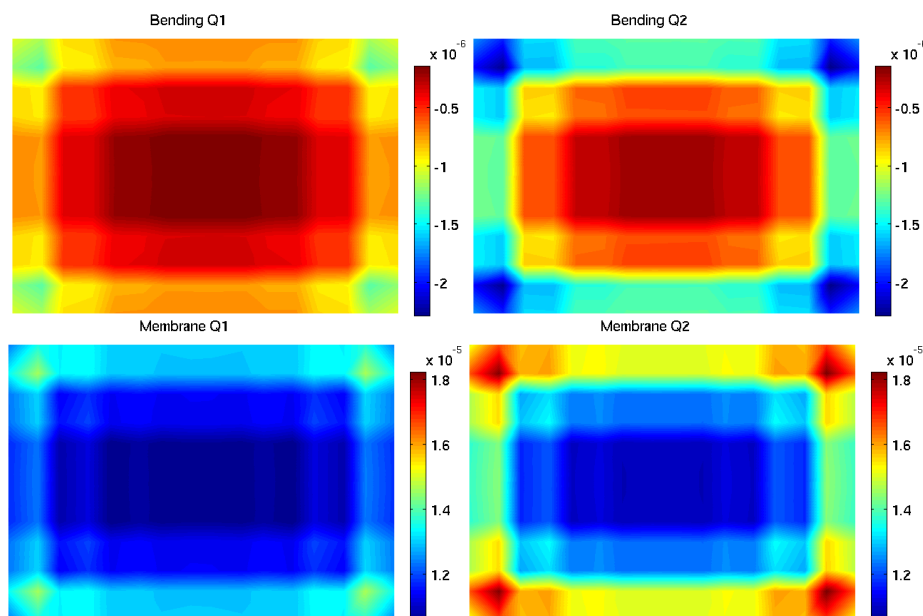

Figure 5.16: *Quasi-static response at 10 Hz for bending and membrane actuation. Charge in the top Q2 (shown right) and bottom Q1 (shown left) electrodes shown with the same scale*

Figure 5.17 for vertical bending, and Figure 5.18 for in-plane bending and torsion show the charge distributions of the three patches for the two first bending modes (charge distributions in bottom and top electrodes are shown left and right). Piezo 3 is used as actuator, whereas Piezo 1 and Piezo 2 as sensors. The most variations are again found for the top electrode Q2. The display can be used to verify that the average charge over the surface of sensors is equal to zero as expected. This distribution is however not uniform as was found to actuators.
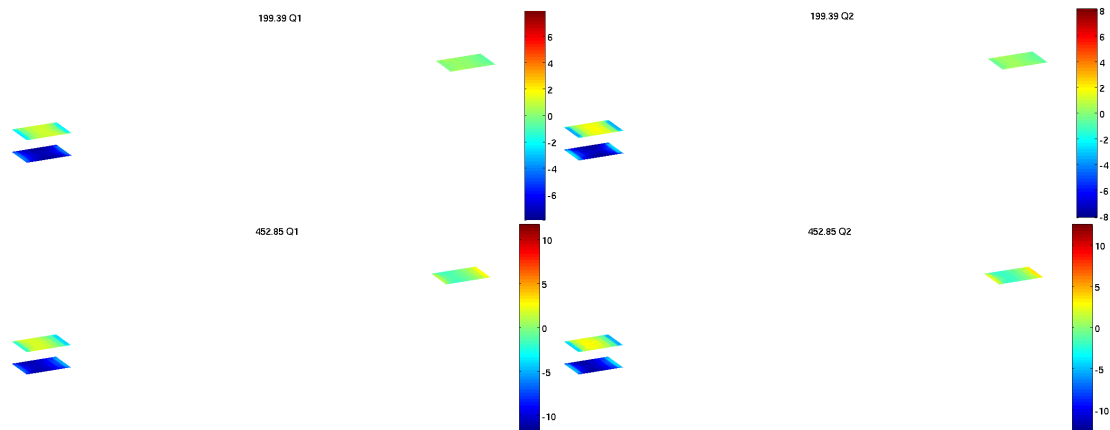
Figure 5.17: *Bending response at 199.39 Hz (top) and 452.85 Hz (bottom) for membrane actuation (Piezo 3). Charge in the top Q2 (shown right) and bottom Q1 (shown left) electrodes shown with the same scale*
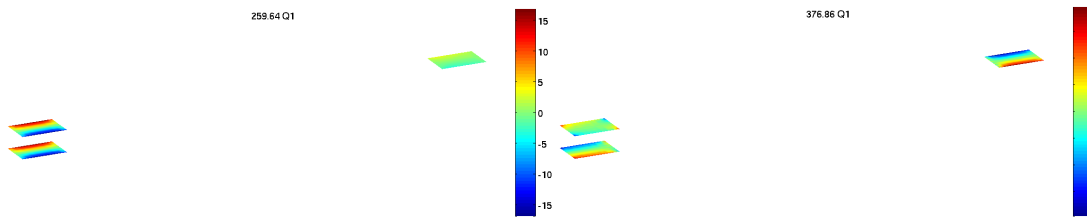
Figure 5.18: *In-plane bending at 259.64 Hz (left) and twisting at 376.86 Hz (right) responses for membrane actuation (Piezo 3). Charge in bottom Q1 electrode*

5.4   Residual flexibility: experimental measurement and implications

This section will focus on the illustration of local bending effects of the patches. The detailed mechanical behavior of the structure under the patches has been the object of very few studies. Its impact in the configuration studied in this work is very significant. It is believed that such effects may reduce the performance of active control to some level in a large number of configurations, hence the emphasis placed on the detailed validation of these effects here.

Section 5.4.1 details the results found in the initial modal test that indicate local bending in the vicinity of the patch. As such effects have not been publicized in the literature, section 5.4.2 details a refined test with detailed measurements over the patch surface.

5.4.1   First test along the beam center

The first indications of the issue where found analyzing forced responses of the beam modal test. Figure 5.19 shows test results indicating that the for frequencies away from the resonance, the piezoelectric patch shows significant distortion in phase with the mode before resonance and in opposition after resonance.
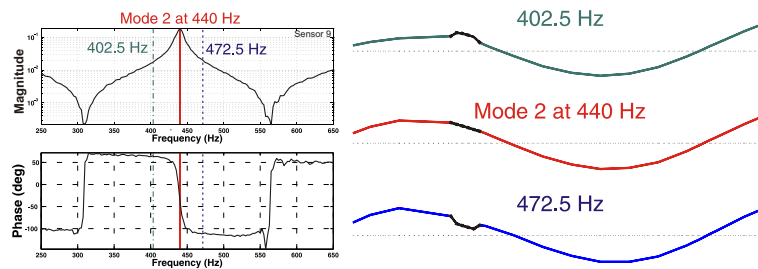
Figure 5.19: *Left : Transfer from patch 1 to displacement at the middle of the patch around the frequency of test mode 2. Right : shape before, at, and after resonance. Carbon/Nomex honeycomb core beam*

For a test using actuation on Piezo 3 (placed on the bottom skin), Figure 5.20 shows a similar effect with a smooth mode and local bending of the top skin for forced responses at off-resonance frequencies.
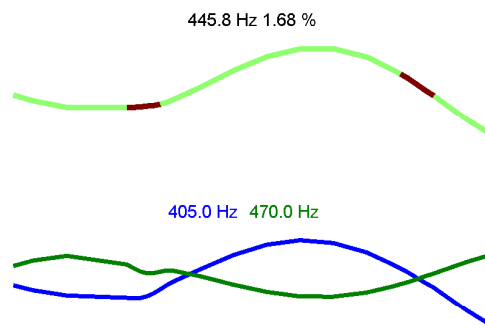
Figure 5.20: *Test deflection shape measured by laser on the top face, beam actuated by piezo3 placed on the bottom face. Top: identified mode. Bottom: responses at off-resonance frequencies.*

As shown in Figure 5.21 and the superposition in Figure 5.22, these experimental results are very well reproduced by the model. In Figure 5.22 the shapes are normalized to optimize the match, since calibration information needed for a direct superposition was missing in the test. With this adjustment, the superposition is almost perfect thus showing the FEM validity.
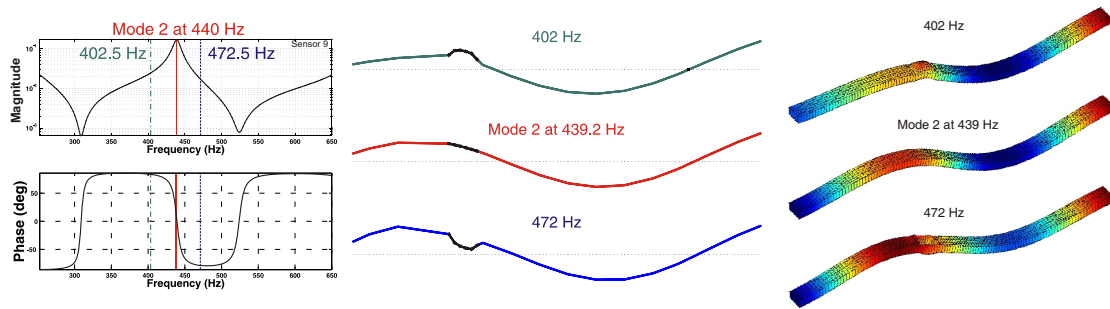
Figure 5.21: *Analysis of the CN20L beam, actuator: patch 1. Shape before, at the 2nd mode, and after resonance*
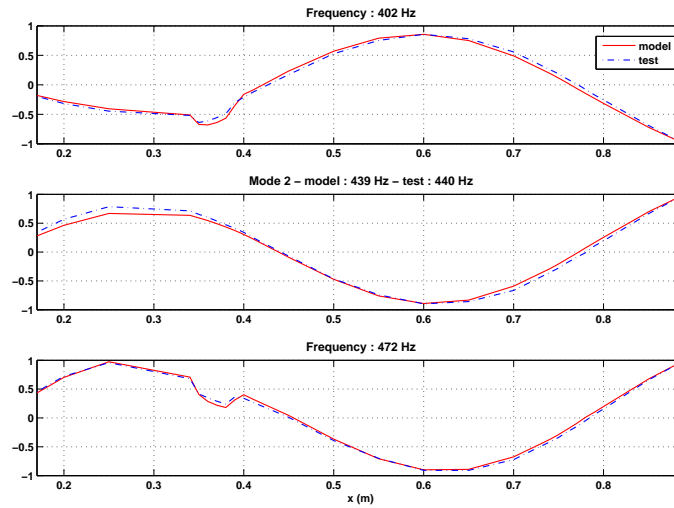
Figure 5.22: *Test and simulation deflection shape comparison*

5.4.2   Local behavior in vicinity of the patch

To give a clearer validation of the local behavior around the patch a second modal test was performed at ECP with a much denser test mesh around the patch shown in figure 5.23.
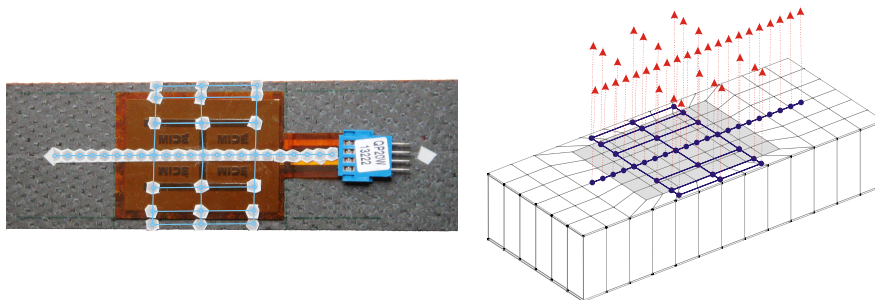
Figure 5.23: *Measurement locations for the modal test focusing on the patch behavior*

The density of measuring points has been increased in the vicinity of the patch to show the blister. The test and simulations in Figure 5.24 reveal the same phenomenon on the patch. In Figure 5.25, the quantitative comparison of the local patch deflection in x and y directions confirms the nearly perfect correlation. Measurement errors are visible, especially in x direction because the sensors were really close (only 3.8 mm between each reflector).
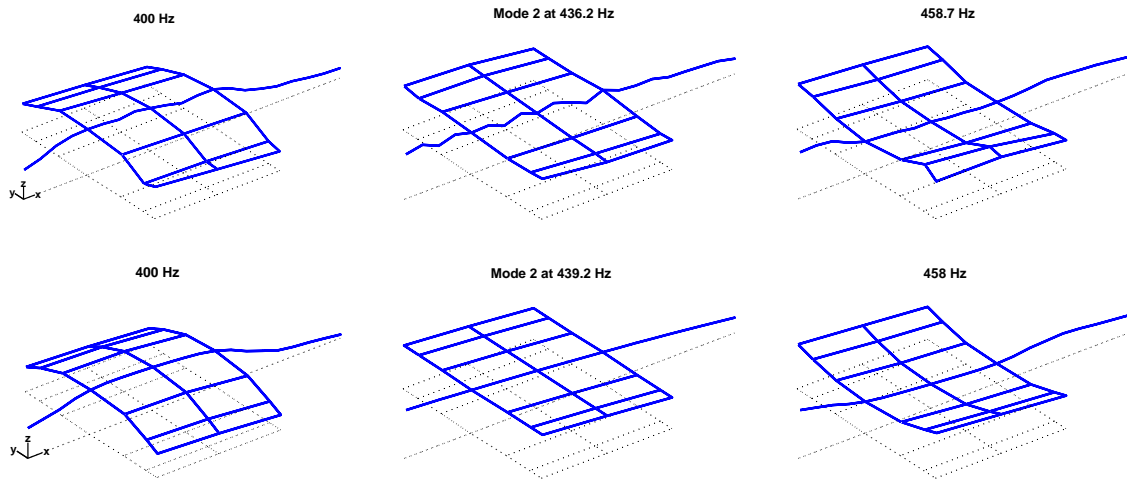
Figure 5.24: *Response before resonance at 400Hz, at resonance 436Hz, and after resonance at 458Hz. Top: test. Bottom : simulation*
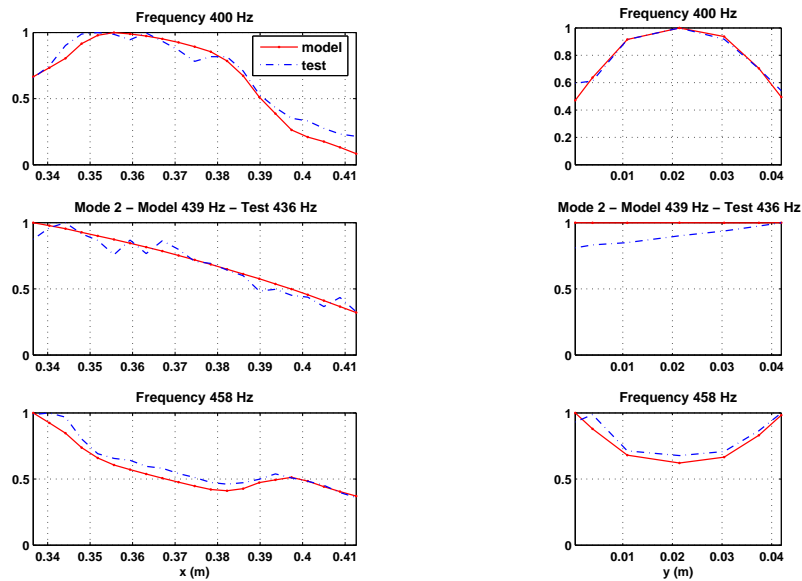
Figure 5.25: *Local blister shape comparison on the x and y axes.*

Modeling of a viscoelastic honeycomb panel equipped with piezoelectric patches in view of vibroacoustic active control design

With a validated model, one can give a clearer explanation of the phenomenon. The static deformation due to the actuator has a blister shape shown in Figure 5.26 (see also Figure 5.15 for a global view). In the low frequency range, this static deformation has a major contribution at all frequencies except resonances. For modes (at resonances), only the passive characteristics of the actuator have an influence so that a smooth shape is found.
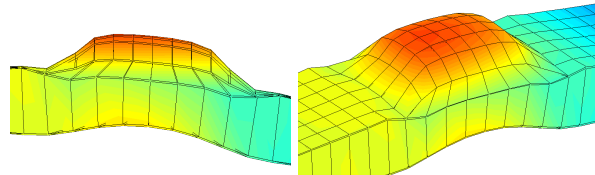
Figure 5.26: *Blister of piezoelectric actuator. Simulated response at 375 Hz*

To underline the importance of this result, one computed the impedance of actuator Piezo 1. As outlined for Figure 5.14, a significant phase excursion is needed for efficient actuation. Figure 5.27 compares the phase for a model with or without static correction. It immediately appears that ignoring static correction would give the false impression of an efficient setup.
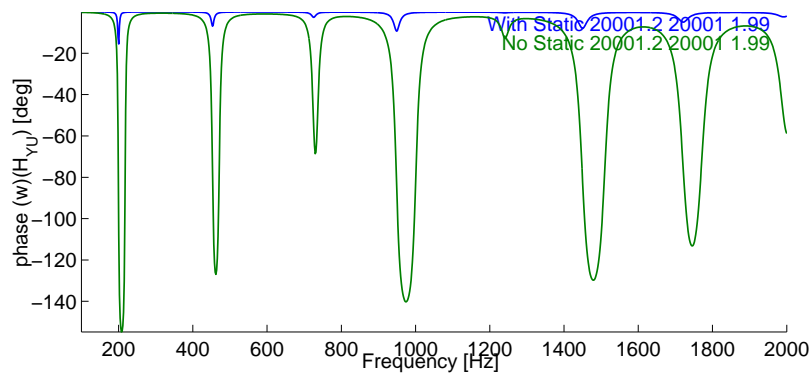
Figure 5.27: *Phase of impedance (transfer from tension to charge) at Piezo 1. Cabling 1 (membrane). Blue : with static correction. Green: without static correction.*

5.5 Using piezo models for design

With the proposed modeling strategy being clearly validated in earlier sections, this section focuses on the practical implementation of the modeling strategy. A simplification of the model of patch plus skin is presented in Section 5.5.1, the purpose is to generate more quickly the meshing for any placement configuration and for any size of patch. As shown previously, the efficiency of the piezoelectric patch on the nominal honeycomb sandwich (CN20, Carbon/Nomex honeycomb of 20 millimeter-thick) is limited by the local effect in vicinity of the patch. The performances of patch actuation are discussed in Section 5.5.2 by comparing the position of open an closed circuit poles for several configurations of sandwich thickness. Section 5.5.3 adresses to the modeling of a realistic trim panel.

5.5.1 Integration strategy

The model considered in previous sections implies significant adaptations. As shown in Figure 5.28/a, the mesh is adapted in the vicinity of the patch and two composite properties are considered. One for the standard honeycomb skin (shown in blue in the figure) and one for the patch which includes multiple layers for the skin plus two layers for the patch, as shown in figure 5.10.

This approach is fine for a small beam model and if only few configurations of patch locations are considered. Indeed, the adaptation of the mesh under the patches would be quite time consuming for a large panel where multiple patch configurations would need to be tested. Furthermore, many articles in the litterature consider that the piezoelectric patch is glued using a viscoelastic material. In such cases, a volume layer is needed to represent shear appropriately.

The idea tested here is thus to use separate elements to model the skin and the piezoelectric patch, with linear constraints used to account for the offset between the two. The shear stiffness of the glue layer (G/h) is deemed sufficiently high to suppose perfect bonding and thus omit glue modeling.

An automated procedure was introduced to mesh the patch. Based on a given rectangular shape, skin elements strictly under the patch are projected to the patch mid-surface. The boundary between the projected elements and the edge of the reference rectangle is then meshed automatically. The resulting model is shown in Figure 5.28/c. This approach is deemed more acceptable than an adaptation of the honeycomb mesh because it only affects a small part of the model and would be adapted for the reuse of nominal modes of the nominal panel. As an intermediate validation, a model with two separate layers (skin and piezo) but an adapted underlying mesh is also considered and shown in Figure 5.28/b.
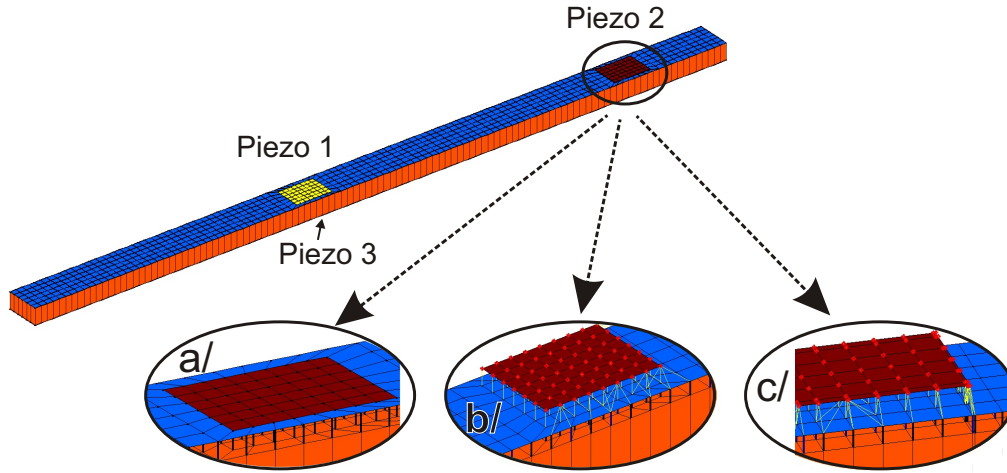
Figure 5.28: *Piezoelectric patch model strategy: a/ adapted meshing and integrated patch, b/ adapted meshing and 2 layers (patch and face sheet), c/ non-adapted meshing and 2 layers*

To compare these models, electric and mechanical transfers are shown in Figures 5.29 and 5.30. For piezo to mechanical and piezo cross transfers, the responses are almost perfectly superposed. For the impedance $\dfrac{Q_{Piezo2}}{V_{Piezo2}}$ however, there is a significant offset of about 30 % on the static response. This error can reasonably be attributed to the lack of adaptation of the mesh on the patch edges.
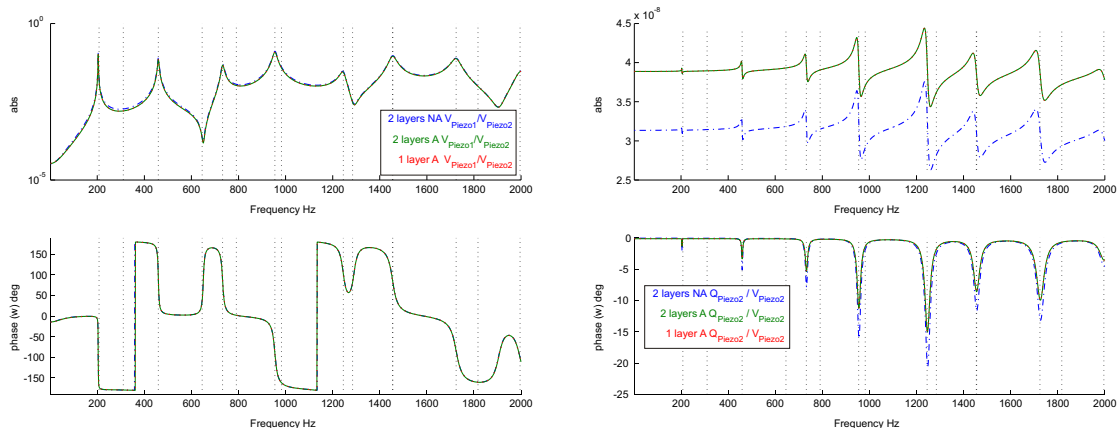
Figure 5.29: *Electric transfers for the 3 strategies. Input actuator Piezo 2 (Voltage). Left: output sensor Piezo 1 (Voltage). Right: output charge generated on Piezo 2*
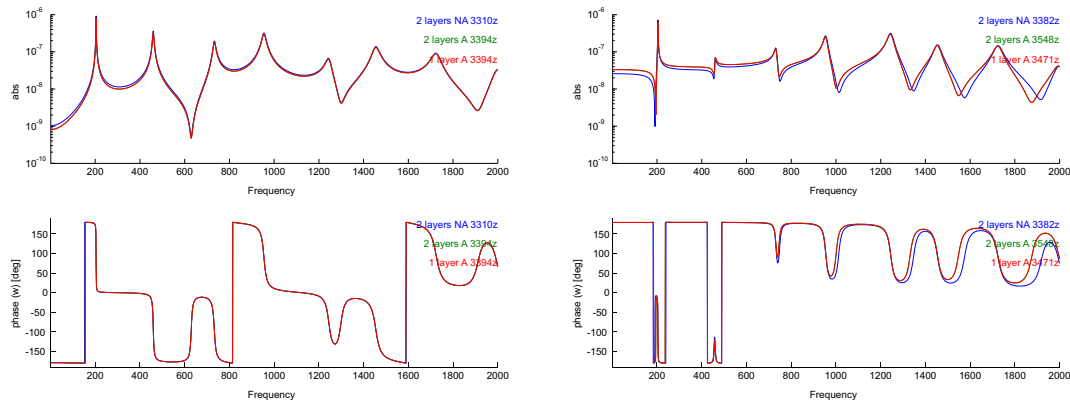
Figure 5.30: *Sample piezo to laser sensor transfers*

The problem on static response is illustrated in Figure 5.31 which shows the quasi-static shape generated by the actuation (since the structure is free floating, one shows the deformation at 1 Hz which avoids problems linked to rigid body modes). The deformations clearly show that the blister shape under the patch cannot be perfectly reproduced due to the lack of mesh adaptation.
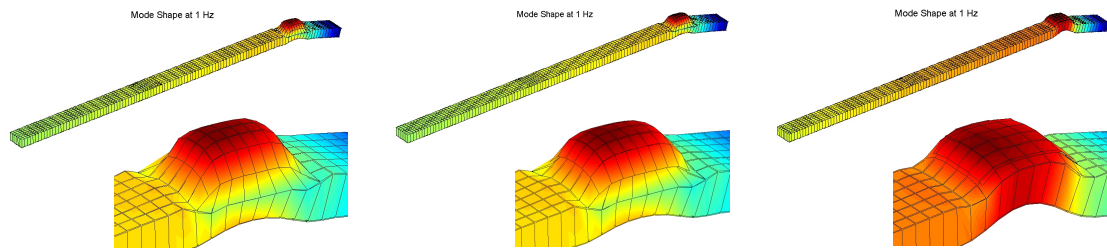
Figure 5.31: *Shape at 1Hz for the 3 model strategies of the piezoelectric actuator (Piezo2)*

The proposed strategy using multiple partially adapted meshes through the thickness, is thus limited by the ability to reproduce local effects under the patch. The local nature of this effect is clearly considered a design flaw of the considered configuration. With better designs, the patch would induce bending with much greater wave length and the mesh adaptation would probably be not as necessary.

5.5.2   Geometric properties and performance

The poor performance of the proposed configuration was clearly related to local bending of the skin under piezoelectric actuation. This was illustrated through the phase of impedances in Figures 5.14 and 5.27. Another classical approach is to compare the position of open an closed circuit poles. Figure 5.32 shows that these are indeed very close in the chosen nominal configuration.
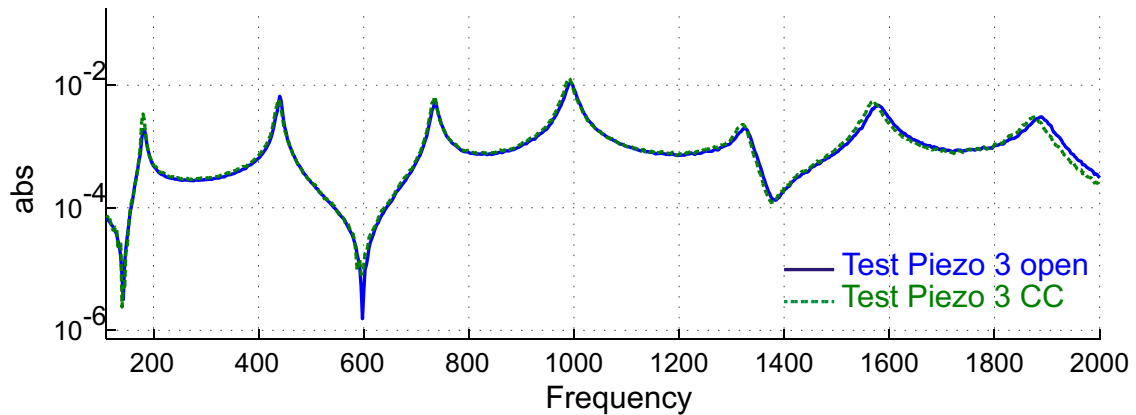
Figure 5.32: *Measured electric transfers between actuator Piezo 2 and sensor Piezo 1 with Piezo 3 open or short-circuit*

To confirm intuition that the impact of the blister shape will depend on the panel characteristics, Figure 5.33 displays the evolution of the shift of frequency between open and closed loop configurations for input at actuator Piezo 2. As expected, diminution of the core thickness leads to lower frequencies. A less trivial result is that the frequency shift augments significantly (in the nominal 20 mm configuration a shift of 0.1 % is only obtained above 1 kHz, with a 1 mm core it is found for the third mode around 200 Hz). This shows that the proposed actuators would be appropriate for plate actuation and that the problem comes from the honeycomb sandwich layup.
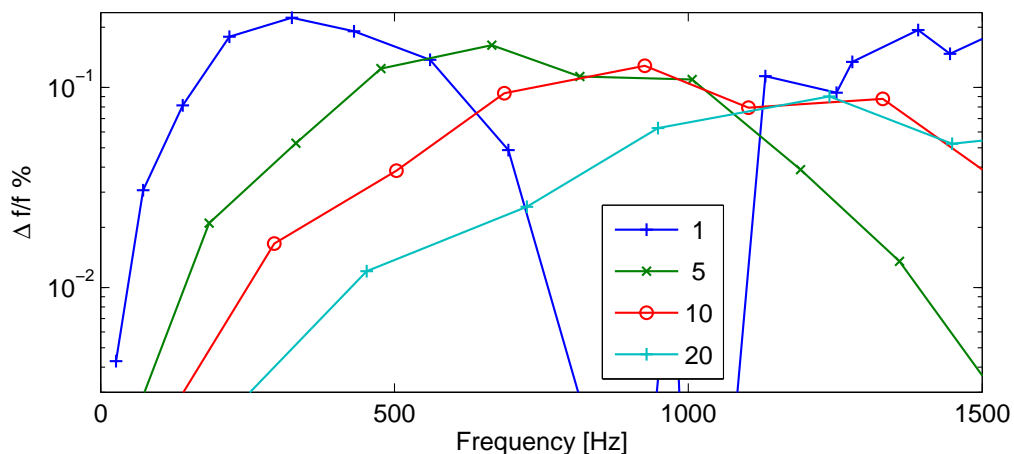
Figure 5.33: *Open/closed loop frequency shift (in %) as a function of core thickness (from 1 to 20 mm). Actuator 2.*

5.5.3   Application to a realistic trim panel

The industrial objective of this study was to be able to predict the effect of the active control on helicopter trim panel made of honeycomb sandwich. The VASCo mock-up shown in Figure 5.34 was developed by ONERA DMAE department in Toulouse to allow a wide range of tests on a cabin representative of generic NH90 helicopter. The internal volume is $2.9{\times}2.5{\times}2.2\ m^3$. The mock-up is composed of several frames and longerons, Carbon - honeycomb sandwich panels having a structural and acoustic role, side doors, a floor, and a roof. Loudspeakers and shakers are implemented to simulate aerodynamic sources and gear box excitations [58], the conditions in the cabin are close to acoustic measurement in a real helicopter cabin.
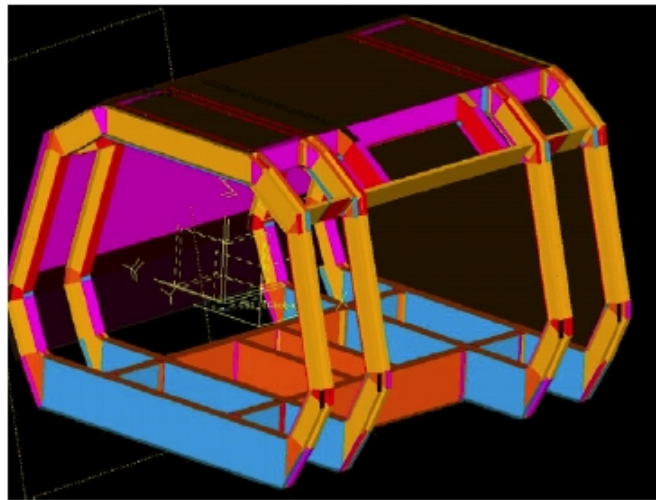
Figure 5.34: *VASCo mock-up*

The helicopter trim panel chosen for validation is made with glass fiber laminate for the face sheets, Nomex based honeycomb and melamine foam for the core, skins and core are glued with epoxy resin, honeycomb and foam with glue redux 382H. The panel is located at the trim roof. Its size is 1160×1240 mm, with 10 attachment points to the cabin around the panel and 4 more around the centre. The attachment is done using blocks which are considered elastic in the computation. Properties of the layup are given in Table 5.7 and figure 5.35, which also shows the location of piezoelectric patches.

Modeling of a viscoelastic honeycomb panel equipped with piezoelectric patches in view of vibroacoustic active control design

**Table 5.7:** *Definition of VASCo sandwich properties*

	Geometric Parameters		Material Parameters			
Glassfiber face sheet	h_f	1	ρ_f	1700	E_f	21000
Epoxy resin	h_r	0.4	ρ_r	1200	E_r	4000
Nomex Honeycomb	h_h	2.6	ρ_h	96	E_h	1
Glue redux 382H	h_g	0.15	ρ_g	1050	E_g	1950
Melamine foam	h_m	14	ρ_m	11.7	E_m	0.35

Length in mm, density in kg/m^3, elastic moduli in MPa
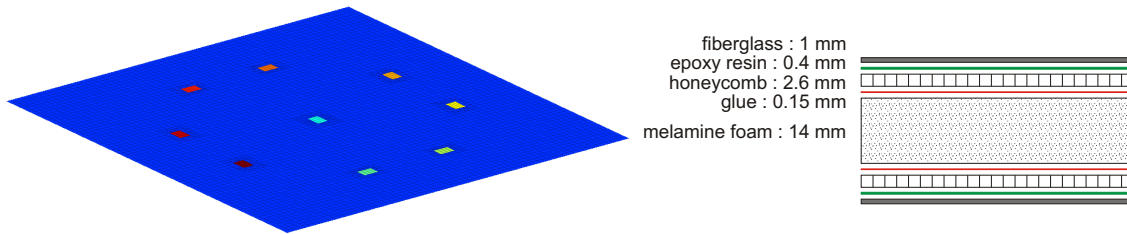
Figure 5.35: *Trim panel used in VASCo mock-up. Left: patches localization. Right: description of sandwich layers*

The objective of the simulation is to demonstrate the applicability of the proposed methodology to an industrial configuration. The mesh was generated using 9 elements trough the thickness: 2 outer shells for the skins, and volume elements for the other layers which are 4 glue, 2 Nomex honeycomb and 1 melamine. The piezoelectric patches are modeled using 4 x 4 elements which is sufficient to view local skin bending. A local automated 2D meshing procedure is used to obtain the adaptation of panel and patch mesh sizes before generating the thickness layup through extrusion. Despite this fairly rich procedure, the model has a reasonable size with 52 900 nodes, 221 000 DOFs and 60 000 elements. This poses no problem for panel computations and integration into a larger model could be easily done using superelements.

The accuracy of mode predictions was established in Friendcopter european project [59] (restricted publication).

Active control tests performed by ONERA showed very local acoustic emissions around the patches. The model was thus used to confirm that this panel configuration also showed local skin bending effects. Figure 5.36 clearly shows the blister shape for a static piezoelectric input. Figure 5.37 compares impedance computations with and without static correction. It clearly appears that the impact is even larger than for the CN20 beams. Modes are almost invisible in the impedance when the static correction is accounted for. One can thus conclude that the relative properties of patches and the sandwich layup lead to a very poor actuation mechanism in this case.
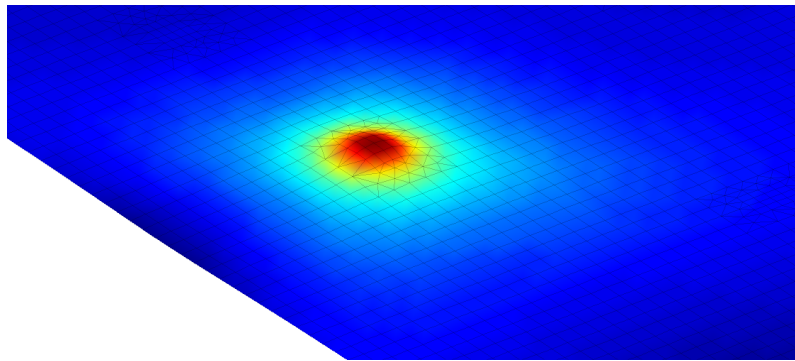
Figure 5.36: *Static response to an applied voltage on piezo 5*
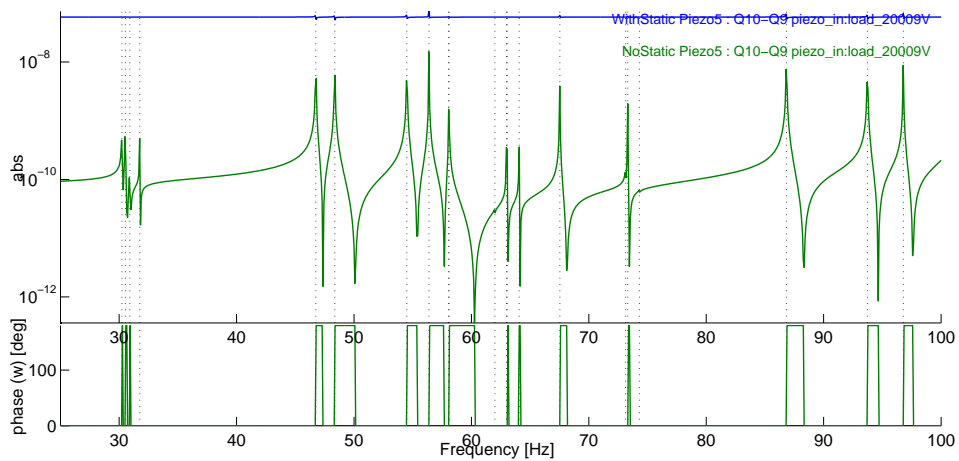
Figure 5.37: *Impendance for piezo 5 transfer. Blue : with static correction. Green : without static correction*

Modeling of a viscoelastic honeycomb panel equipped with piezoelectric patches in view of vibroacoustic active control design

Chapter 6

Conclusion and perspectives

Chapter 2 presented a literature review on tools used to model panels with honeycomb cores. Models detailing the honeycomb cell geometry are so large that equivalent representations are needed to allow coarser and thus more manageable meshes. The so called zig-zag (or layerwise model) and the shell-volume-shell model both properly represent the transverse shear in a cross section and thus can be used to describe the dynamic behavior of thick and/or viscoelastic layers such as honeycomb.The SVS model was preferred here because the use of multiple elements through the thickness is compatible with all FEM softwares, while zig-zag models require specific developments.

In the SVS model the honeycomb layer is represented by an equivalent volume with orthotropic material properties. As detailed in Section 2.3.2, the estimation of these orthotropic properties has been the subject of many publications without reaching a general agreement (see Table 3.4). The objective of chapter 3 was thus to introduce a numerical procedure to estimate effective parameters for the orthotropic material. Such a procedure can be seen as a numerical homogeneization.

The need for a numerical procedure allowing arbitrary detail in the cell meshing was based on the comments found in the literature on the influence of adhesive layer and skin properties. As a means to achieve this objective, it was proposed to use the frequency of periodic modes (waves propagating with a certain wavelength) as an objective function used to estimate equivalent properties of the honeycomb core.

In the sample case treated, the equivalence was shown to pose problems for low and high frequencies. At low frequencies, the error on panel predictions is small but the response is insensitive to the core properties which thus cannot be estimated properly. A small bias in frequencies was related to a mass effect but proper analysis of the phenomenon remains to be done. At high frequencies, or wavelengths lower than 10 cells, the model breaks down but this could be expected, since the energy fraction associated with skin bending increases rapidly.

The analysis of energy contributions in constituents as a function of wavelength also gave very useful insight. In addition to showing the classical importance of the core shear moduli $G_{xz}^\star, G_{yz}^\star$ and the skin modulus E_f, it showed that shear moduli only have an impact in a medium frequency range whose location depends on the skin properties. The influence of glue was also shown to be significant and a method to separately estimate core and glue properties was proposed.

While this is yet another procedure in a long list of methods giving similar results, one can claim that the method is useful for a wide range of applications because of its

key advantages of being able to account for arbitrary levels of detail, because periodic modes are computed on two cell meshes, and giving the possibility to validate robustness by comparing results at multiple wavelengths.

Issues that remain to be treated are the analysis of validity for static and dynamics applications, the modeling of transition regions where the skin or honeycomb have variable material or geometric characteristics, or the experimental demonstration of the ability to separate constituent properties in panel tests.

The objective of chapter 4 was to determine material properties of a specific Nomex paper based honeycomb. This honeycomb is used in trim panels for helicopter and aircraft applications. The process used, and validated in the chapter, is a model update of effective parameters by comparison of mode frequencies in free/free configuration. The initial suspicion that this material has a viscoelastic behavior was clearly validated by showing both frequency and temperature dependence. A fractional derivative model of the frequency dependence of the effective parameters was identified and validated by reusing values obtained on aluminum skin beams to predict responses on carbon skin beam tests.

For the considered honeycomb samples, the orthotropic shear moduli are both influential on the response (inducing frequency shifts of 3 to 5 %).Moreover, they are frequency and temperature dependent in the 0-1 kHz range which is the target for active control. The need to account for these dependencies in accurate predictions was thus established.

A first question left open is the use of estimated effective shear moduli to estimate constituent properties. This corresponds to the inverse of the homogeneization procedure introduced in chapter 3 and would allow predictions of effective properties for other core thickness or cell dimensions. A second issue would be the improvement of damping measurement in the test to allow the use of the imaginary part of the estimated shear moduli for damping predictions.

Having a validated model for honeycomb panels, chapter 5 addresses the modeling of piezoelectric patches to be used as sensors or actuators. After introducing the equations needed for the development of a piezoelectric shell element and its integration in a finite element resolution procedure, the chapter discussed validations performed on carbon skin/Nomex honeycomb beams equipped with MIDE QuickPack patches. When accounting for the viscoelastic behavior of the honeycomb, correlation of modal properties as well as piezoelectric transfers was shown to be very good.

Analysis of forced responses showed a major impact of static contribution of the actuator. In terms of mechanical behavior, the effect corresponds to actuation of local skin bending rather than global panel bending. In terms of control performance, this effect leads to small pole/zero separation in collocated transfers which is known to correspond to poor performance for collocated control strategies. Local skin bending being a not obvious result, detailed experimental validation was performed to confirm the model validity.

Proper understanding of how static contribution limits the controllability of honeycomb panels is a major contribution of the thesis. The result clearly motivates the need to use proper mechanical models, which has often been neglected in active control studies.

To conclude the chapter, strategies to incorporate patches using single or multiple element layouts, possibly with non-conforming meshes, were discussed. Avoiding remeshing was shown to be possible in actuator placement phases provided that the underlying mesh is sufficiently fine. Nominal modes could certainly be kept constant when testing various actuator positions, but static deflections need to be recomputed to obtain proper electrical transfers. This aspect is clearly absent in a lot of studies which use modal controllabilities as a basis for placement. Introducing a placement algorithm accounting for static effects is thus a clear need for the future.

Changing the honeycomb thickness was then shown to impact the static contribution limitation. In the long term, the way to improve performance is to design a proper actuation mechanism that has significant controllability for modes in the low frequency band, which is of interest in active noise control. Such an actuation mechanism will certainly require stiffening around the patch to favor panel bending while avoiding local skin bending. Introducing structural optimization procedures to obtain efficient actuation seems a useful direction for future work.

Finally, the possibility to apply the proposed models for more realistic panels was demonstrated using the VASCo helicopter cabin mock-up. The implementation of a 9 layer model with 9 piezoelectric patches posed no particular problem and the configuration also showed major limitations due to the static contribution effect. This study thus gave a proper mechanical explanation to issues in earlier active control experiments that motivated the thesis.

Bibliography

[1] R. A. S. Moreira, J. Dias Rodrigues, and A. J. M. Ferreira. A generalized layer-wise finite element for multi-layer damping treatments. *Computational Mechanics*, 37(5):426–444, 2006.

[2] J. Hohe. A direct homogenisation approach for determination of the stiffness matrix for microheterogeneous plates with application to sandwich panels. *Composites, Part B: Engineering*, 34:615–626, 2003.

[3] L. J. Gibson and M. F. Ashby. *Cellular Solids Structure and Properties, Second Edition*. Cambridge University Press, 1997.

[4] L. Al Bachi. *Modélisation numérique et expérimentale du comportement de matériaux sandwiches appliqués à láéronautique*. PhD thesis, Institut National Polytechnique de Toulouse, France, 2002.

[5] T. Bitzer. *Honeycomb Technology: Materials, Design, Manufacturing, Applications and Testing*. Chapman & Hall, 1997.

[6] B. Petitjean, O. Hernandez, and F. Cléro. Active trim panels for interior aircraft noise reduction. ACTIVE04, 2004.

[7] A.K. Noor, W.S. Burton, and C.W. Bert. Computational models for sandwich panels and shell. *ASME Journal of Applied Mechanical Reviews*, 49:155–199, 1996.

[8] E. Nilsson and A.C. Nilsson. Prediction and measurement of some dynamic properties of sandwich structures with honeycomb and foam cores. *Journal of Sound and Vibration*, 251(3):409–430, 2002.

[9] V. Piefort. *Finite Element Modelling of Piezoelectric Active Structures*. PhD thesis, Active Structures Laboratory Department of Mechanical Engineering and Robotics, Université Libre de Bruxelles, Belgium, 2001.

[10] A. Preumont. *Vibration control of active structures - An introduction - 2nd edition*. Solid Mechanics and its Applications - Kluwer Academic Publishers, 2002.

[11] S. Kelsey, R. A. Gellatly, and B. W. Clark. The shear modulus of foil honeycomb cores. *Aircraft engineering*, 30:294–302, 1958.

[12] C. W. Schwingshackl, P. R. Cunningham, and G. S. Aglietti. Honeycomb elastic material properties: A review of existing theories and a new dynamic approach. In *International Conference on Noise and Vibration Engineering*, ISMA, 2004.

[13] R. M. Jones. *Mechanics of composite materials*. Mc Graw-Hill, 1975.

[14] E. Reissner. Reflections on the theory of elastic plates. *Applied mechanics reviews*, 38:1453–1464, 1985.

[15] Reddy J.N. *Mechanics of laminated composite plates: theory and analysis*. CRC Press, Boca Raton, 1997.

[16] M. Touratier. An efficient standard plate theory. *International journal of engineering science*, 29:901–916, 1991.

[17] A. Idlbi, M. Karama, and M. Touratier. Comparison of various laminated plate theories. *Composite Structures*, 37:173–184, 1997.

[18] J.-M. Berthelot. *Materiaux composites - Comportement mecanique et analyse des structures*. Masson, 1992.

[19] T. Saito, R.D. Parbery, S. Okuno, and S. Kawano. Parameter identification for aluminum honeycomb sandwich panels based on orthotropic timoshenko beam theory. *Journal of Sound and Vibration*, 208 (2):271–287, 1997.

[20] D. Backstrom and A.C. Nilsson. Modelling the vibration of sandwich beams using frequency-dependent parameters. *Journal of Sound and Vibration*, 300:589–611, 2007.

[21] M. Areias Trindade. *Contrôle hybride actif-passif des vibrations de structures par des matériaux piézoélectriques et viscoélastiques: poutres sandwich/multicouches intelligentes*. PhD thesis, Conservatoire des Arts et Métiers, Paris, France, 2000.

[22] C. C. Chamis, R. A. Aiello, and L. N. Murthy. Fiber composite sandwich thermostructural behaviour: computational simulation. *Journal of Composites Technology and Research (ASME)*, 10(3):93–99, 1988.

[23] A.-S. Plouin and E. Balmés. Steel/viscoelastic/steel sandwich shells computational methods and experimental validations. In *International Modal Analysis Conference*, IMAC, 2000.

[24] F. W. Grosveld, R. D. Buehrle, and J. H. Robinson. Structural and acoustic numerical modeling of a curved composite honeycomb panel. AIAA, 2001-2277.

[25] C. Florens, E. Balmès, F. Cléro, and M. Corus. Accounting for glue and temperature effects in nomex based honeycomb models. In *International Conference on Noise and Vibration Engineering*, ISMA, 2006.

[26] A.K. Noor and W.S. Burton. Assessment of continuum models for sandwich panel honeycomb cores. *Computer methods in applied mechanics and engineering*, 145:341–360, 1997.

[27] E. Balmès. *Viscoelastic vibration toolbox, User Manual*. SDTools, 2004-2007.

[28] M. Grédiac. A finite element study of the transverse shear in honeycomb cores. *International Journal of Solids and Structures*, 30(13):1777–1788, 1993.

[29] F. Meraghni, F. Desrumaux, and M.L. Benzeggagh. Mechanical behaviour of cellular core for structural sandwich panels. *Composites, Part A: applied science and manufacturing*, 30:767–779, 1999.

[30] G. Shi and P. Tong. Equivalent tranverse shear stiffness of honeycomb cores. *International Journal of Solids and Structures*, 32:1383–1393, 1995.

[31] L. Gornet, G. Marckmann, and M. Lombard. Détermination des coefficients d´élasticité et de rupture d´âmes nids d´abeilles *nomex*® : homogénéisation périodique et simulation numérique. *Mécanique et Industries*, 6:595–604, 2006.

[32] J. Hohe and W. Becker. An energetic homogenisation procedure for elastic properties of general cellular sandwich cores. *Composites, Part B: Engineering*, 32:185–197, 2001.

[33] J. Hohe and W. Becker. A refined analysis of the effective elasticity tensor for general cellular sandwich cores. *International Journal of Solids and Structures*, 38:3689–3717, 2001.

[34] E. Balmès, J.M. Leclère, and J.P. Bianchi. *Structural Dynamics Toolbox 6.0 (for use with MATLAB)*. SDTools, Paris, France, www.sdtools.com, May 2007.

[35] A. Grédé, B. Tie, and D. Aubry. Elastic wave propagation in hexagonal honeycomb sandwich panels: Physical understanding and numerical modeling. Eighth International Conference on Mechanical and Physical Behaviour of Materials under Dynamic Loading, 2006.

[36] E. Balmès. Parametric families of reduced finite element models. theory and applications. *Mechanical Systems and Signal Processing*, 10(4):381–394, 1996.

[37] E. Balmès. Uncertainty propagation in experimental modal analysis. *IMAC, Dearborn*, 2004.

[38] Adrien Bobillot. *Méthodes de réduction pour le recalage. Application au cas d'Ariane 5*. PhD thesis, École Centrale Paris, 2002.

[39] A. Sternchüss. *Multi-level parametric reduced models of rotating bladed disk assemblies*. PhD thesis, Ecole Centrale de Paris, 2009.

[40] D. Clouteau, M. Arnst, T.M. Al-Hussaini, and Degrande G. Free field vibrations due to dynamic loading on a tunnel embedded in a stratified medium. *Journal of Sound and Vibration*, 238:173–199, 2005.

[41] Sternchüss, A. and Balmes, E. and Jean, P. and Lombard, JP. Reduction of Multistage disk models : application to an industrial rotor. In *012502*, 2008. Paper Number GT2008-012502.

[42] W. S. Burton and A.K. Noor. Structural analysis of the adhesive bond in a honeycomb core sandwich panel. *Finite Elements in analysis and design*, 26:213–227, 1997.

[43] C. C. Foo, G. B. Chai, and L. K. Seah. Mechanical properties of nomex material and nomex honeycomb structure. *Composite structures*, 80:588–594, 2007.

[44] A.D. Nashif, D.I.G. Jones, and J.P. Henderson. *Vibration Damping*. John Wiley and Sons, 1985.

[45] M. Nash. Use of the multivariate mode indicator function for normal mode identification. *International Modal Analysis Conference*, pages 740–744, 1988.

[46] D.J. Ewins. *Modal Testing: Theory and Practice*. John Wiley and Sons, Inc., New York, NY, 1984.

[47] W. Heylen, S. Lammens, and P. Sas. *Modal Analysis Theory and Testing*. KUL Press, Leuven, Belgium, 1997.

[48] E. Balmes. Frequency domain identification of structural dynamics using the pole/residue parametrization. *International Modal Analysis Conference*, pages 540–546, 1996.

[49] N. Lieven and D. Ewins. Spatial correlation of modeshapes, the coordinate modal assurance criterion (comac). International Modal Analysis Conference, 1988.

[50] G. Kergourlay. *Mesure et prédiction vibroacoustique de structures viscoélastiques - Application a une enceinte acoustique*. PhD thesis, Ecole Centrale Paris, France, 2004.

[51] Salençon J. *Viscoélasticité*. Presse des Ponts et Chaussées, 1983.

[52] E. Balmès and J.-M. Leclère. *Viscoelastic Vibration Toolbox*. User's Guide, January 2006.

[53] *Midé Technology Corporation*. http://www.mide.com.

[54] *IEEE Standard on Piezoelectricity*. ANSI/IEEE Std 176, 1987.

[55] A. Preumont. *Mechatronics - Dynamics of Electromechanical and Piezoelectric Systems*. Solid Mechanics and its Applications - Springer, 2006.

[56] E. Balmès and J.-M. Leclère. *Structural Dynamics Toolbox - FEMLink*. User's Guide Version 5.2, May 2005.

[57] E. F. Crawley and E. H. Anderson. Detailed models of piezoceramic actuation of beams. *Journal of Intelligent Material Systems and Structures*, 1(1):4–25, 1990.

[58] E. Julliard, F. Simon, S. Pauzin, and D. Biron. Acoustic localization into a generic helicopter cabin. Euronoise 2006, May-June 2006.

[59] V. Cokonaj, A. Criado Abad, G. Kawiecki, I. Briones Clar (AERNNOVA), F. Cléro, and F. Simon (ONERA). Active and hybrid control tests on composite panels and on an adapted helicopter cabin composite mock-up and provision of segmented active constrained layer-based panel vibrations damping system, ready to be flight tested. *FRIENDCOPTER Report - RESTRICTED release*, June 2007.

Résumé

Le contrôle actif a souvent été considéré pour la maîtrise du bruit basse fréquence rayonné par les panneaux d'habillage dans les cabines des avions et hélicoptères. Ces panneaux sont classiquement réalisés en matériaux sandwich nid d'abeille (nida), du fait de leur très bon rapport résistance/masse. La mise en oeuvre des techniques de contrôle actif sur des panneaux de type nida n'a pas toujours donné des résultats à la hauteur des attentes. Le travail présenté dans cette thèse introduit un modèle coque/volume/coque (SVS) de panneau nida équipé de pastilles piézoélectriques, valide ce modèle expérimentalement et propose une analyse des limitations de performance du contrôle actif.

Pour la modélisation des panneaux nida, la principale difficulté est d'estimer les propriétés effectives d'un matériau homogène équivalent au coeur. On introduit une procédure d'homogénéisation numérique à partir d'un modèle 3D très détaillé de la structure du nida. Cette procédure est basée sur la corrélation des modes périodiques du modèle 3D et du modèle SVS. L'utilisation de modes périodiques permet l'analyse détaillée de l'influence des constituants dans le comportement vibratoire du nida, en particulier de la couche de colle et des peaux du sandwich. Des essais vibratoires mettent en évidence les effets viscoélastiques présents pour les nida à base de papier Nomex. Ces effets sont pris en compte dans le modèle SVS en utilisant des paramètres élastiques dépendant de la fréquence. On intègre ensuite des actionneurs et capteurs piézoélectriques au modèle de panneau nida validé. Différentes stratégies pour l'intégration du modèle proposé dans un processus de conception sont discutées. On montre enfin que la réponse statique à une tension électrique correspond à une cloque, flexion très localisée des peaux plutôt que flexion globale du panneau. Il en résulte une mauvaise performance des actionneurs. Cet effet local est retrouvé sur un modèle de panneau d'habillage réaliste étudié à l'ONERA.

Mots clés : Contrôle actif, nid d'abeille, corrélation calcul-essais

Abstract

Active control has often been considered for low frequency control of noise radiated by trim panels inside aircraft or helicopter cabins. Trim panels are usually made of honeycomb core sandwich because of their high strength to mass ratio. Active control techniques applied to honeycomb panel have not always given results as good as expected and this thesis aims to understand these limitations based on validated mechanical models of the active panels.

For the modeling of honeycomb panels, the main difficulty is to estimate equivalent properties for the core. A numerical homogenization procedure is introduced to estimate effective parameters of a shell/volume/shell model based on the correlation with periodic modes of a detailed 3D model. The use of periodic modes allows a detailed analysis of the influence of constituent properties, especially glue and skin. Tests show that the considered Nomex based honeycomb has significantly viscoelastic behavior. In the model, the viscoelastic behavior of the core is taken into account by a frequency dependence of material parameters. Piezoelectric actuators and sensors are included in the validated honeycomb model. Strategies for integration in a numerical design process are discussed. Finally, the static response to an applied voltage is shown to correspond to a blister shape with local bending of the skin rather than global bending of the panel. This behavior results in poor actuator performance, which is also found in a realistic panel configuration studied at ONERA.

Keywords: active control, honeycomb, test-analysis correlation